POLITECNICO DI MILANO
Scuola di Ingegneria Industriale e dell'Informazione
Corso di Laurea Magistrale in Ingegneria Fisica

Advances in the detection at the new XMCD and RIXS beamline of the ESRF

Relatore: Prof. Giacomo Claudio GHIRINGHELLI
Correlatore: Prof. Lucio BRAICOVICH

Tesi di Laurea di:
Cassiano LANGINI
Matr. Nr. 801278

Anno Accademico 2013-2014

Abstract

The European Synchrotron Radiation Facility is a synchrotron radiation source offering forefront experimental instrumentation for the investigation of the magnetic properties and the electronic structure of materials. Within a general upgrade programme of the facility, the new ID32 soft X-ray beamline has been built, offering two experimental end-stations: one for RIXS and the other for XMCD measurements. ERIXS, the new spectrometer of the RIXS branch, is designed to achieve an unprecedented resolving power, requiring the optimization of all its components. In the present work we explore the possibility of enhancing the spatial resolution of the CCD detector of the spectrometer, which can be done by calculating the centre of mass of the charge clouds generated by each photon. This approach introduces some artefacts in the reconstructed images that we were able to remove by using the so-called η algorithm and one of its possible extensions. In the meantime we carried out the very first experiment of the XMCD branch of ID32, studying the temperature dependence of weak ferromagnetism in samples of doped high-T_c superconducting cuprates.

Summary

The European Synchrotron Radiation Facility (ESRF) is a 6 GeV third generation synchrotron radiation source located in Grenoble. One of the main goals of such research centres is to provide forefront experimental facilities to researchers from all over the world. In a context of continuous technological improvements upgrade programmes are a bare necessity, especially in those experimental areas that are rapidly developing and have proved to be able to produce outstanding scientific results. These motivations have urged the upgrade of ID8 to the new ID32 beamline, in order to create a cutting edge facility for the study of magnetic and electronic properties of materials with soft X-rays. It was decided to focus on two experimental techniques that have been attracting much attention in recent years: Resonant Inelastic X-ray Scattering (RIXS) and X-ray Magnetic Circular Dichroism (XMCD). So the new beamline is split into two branches leading to separate end-stations. The beam line construction is about to be completed: the XMCD branch has seen its first experiment in November 2014 whereas the RIXS branch is under commissioning and will probably greet the first users in July 2015.

As part of this thesis we followed the recent advances of the beamline and focused on two separate aspects, one regarding RIXS and the other concerning XMCD. Hence we present in this work two conceptually distinct results, but relating to the same experimental facility.

The new RIXS spectrometer of the beamline, called ERIXS, promises to reach a resolving power not seen before, touching 30 meV resolution at the copper L_3 edge around 930 eV photon energy. The optical layout of the system is very simple: the radiation emitted by the sample is dispersed by a variable line spacing diffraction grating and focused on a 2D position sensitive detector. In this way the whole spectrum can be acquired in parallel as there is a direct correspondence

between the photon energy and the vertical position on the detector. In order to achieve the desired resolving power of the entire system, the detector spatial resolution plays a role of utmost importance. Excellent detection performances can be obtained through the use of a commercial Charge Coupled Device (CCD) optimized for soft X-rays. Unfortunately the best spacial resolution they can achieve is limited to $\approx$ 20-25 μm, almost independently of the pixel size. This is due to the process of charge splitting inside the device. When a photon is absorbed within the active layer it generates a cascade of electron hole-pairs, which, while drifting to the quantum wells of the physical pixels, diffuses laterally. The photogenerated electron cloud thus splits among several pixels, deteriorating the spatial resolution. However the same phenomenon of charge splitting is crucially important for the single photon centroid reconstruction. Considering a small group of pixels sharing the charge generated by the absorption of one photon by the active volume of the detector, we can assume that the charge accumulated is proportional to its distance from the impact position. Hence a simple calculation of the centre of mass (COM) can locate each photon with subpixel resolution. The performance of this algorithm was tested experimentally with a CCD with 13.5 μm lateral pixel size, a traditional X-ray source and a razor blade partly covering the detector. The spatial resolution was then estimated by the sharpness of the light-to-dark transition. We were able to reproduce previous results on the same setup confirming a resolution enhancement from $\approx$ 20-25 μm to $\approx 7\,\mu$m using COM calculation. A main drawback of this technique is however a loss in efficiency, because, being a single photon counting method, it works properly only with no overlap of the photon spots, requiring frequent acquisitions and a low photon flux. The detection efficiency can be improved by reading the detector more often, so we tested the COM algorithm in the same experimental conditions but with the fastest available reading mode (pixel reading rate: 1 MHz with respect to 100 kHz of slow reading). This causes the presence of an anomalous background pattern that we were able to subtract almost completely through dark image acquisitions and image processing. Faster acquisition is characterized by higher noise, passing from ≈ 3.5 to ≈ 10 electrons *rms* per pixel, but we were anyway able to obtain a resolution of $\approx 8.5\,\mu$m with the best choice of software parameters. We also reported a value of $\approx 5\,\mu$m resolution, which however appears to be not reliable, being too small with respect to the slow reading values. Additional studies of the algorithm performances were carried out through the use of single-photon Monte Carlo simulations, which allowed us to explore the noise dependence of resolution for different pixel sizes and incoming photon energies.

Although giving encouraging results on resolution, images reconstructed through centroiding suffer from the presence of some artefacts. These are related to the fact that COM calculation systematically shifts the photon position towards the centre of the presumed central pixel of the spot. Hence the problem is more relevant for pixel edges that are depleted in reconstructed images, leading to unpleasant intensity oscillations in regions of homogeneous illumination. We tested two algorithms that compensate the systematic error made by COM calculation applying a statistical correction. The first one is the η algorithm, which works on 2×2 pixel matrices and the second, which we called β algorithm, is simply an extension of η to 3×3 spots. According to simulations, we proved that both η and β algorithms are able to correct the artefacts of COM calculation and perfectly succeed in reconstructing a flat field illumination. Furthermore the noise dependence of the total reconstruction error seems to suggest that both η and β outperforms the COM resolution at each readout noise level up to 12 electrons. The next step will then be to test them on real images taken with our setup and directly with ERIXS.

In recent years the development of RIXS has produced very important results on cuprate high-T_c superconductors. These materials exhibit unusual properties and ordering phenomena of both charge and spin that still represent one of the most challenging mysteries of condensed matter physics. A common feature of cuprate structure that is believed to play an important role in superconductivity is the presence of CuO_2 planes. Each Cu^{2+} ion within them is in the $3d^9$ configuration with an unpaired electron in the outer shell, developing a long-range antiferromagnetic order within the plane. A weaker inter-plane coupling determines an overall 3D antiferromagnetism, which is rapidly suppressed by the introduction of dopants. The unpaired spins, localized on Cu atoms, are not perfectly in plane but they are slightly canted due to the Dzyaloshinsky-Moriya interaction, thus developing a small out of plane component. The net magnetization is anyway zero because consecutive CuO_2 planes orient antiferromagnetically with respect to each other. However an external field is able to unveil the "hidden" weak ferromagnetism. XMCD technique can be very useful in studying these kind of systems and has recently demonstrated that this behaviour also persists upon doping in different families of cuprates. In this context we carried out an experiment to inspect the temperature dependence of the XMCD signal in underdoped and optimally doped samples of $La_{2-x}Sr_xCuO_4$ and $NdBa_2Cu_3O_{6+x}$. This was the very first experiment of the XMCD branch of ID32 and so it also represented the first trial of all the equipment in a "real" situation. We were able to report some minor energy drifts and a non-linearity in the measurement of the incoming beam intensity, although the overall quality of the absorption spectra was excellent. Despite the practical difficulties of measuring XMCD signals smaller than 1% on a totally new beamline, we succeeded in collecting a consistent set of data. The XMCD at the Cu L_3 edge of NBCO showed a paramagnetic temperature dependence that seemed in accordance with literature results. However we reported the persistence of an XMCD signal even at room temperature that has been never detected before. We also measured, for the first time to our knowledge, the XMCD at the O K edge of NBCO. The data seem to confirm the observations at the Cu edge, but the interpretation is less straightforward as the oxygen signal was smaller in intensity and more complex in shape.

Sommario

L'European Synchrotron Radiation Facility, abbreviato in ESRF, è una sorgente di luce sincrotronica di terza generazione, situato a Grenoble. Uno degli obiettivi principali delle grandi strutture di ricerca come ESRF è quello di fornire a ricercatori provenienti da tutto il mondo strumentazioni di misura molto costose e all'avanguardia. Tuttavia in un contesto di continue scoperte scientifiche e rapido sviluppo tecnologico un programma di aggiornamento delle strutture è spesso una necessità, specialmente per quanto riguarda quelle aree sperimentali che hanno avuto un grande sviluppo negli ultimi anni, producendo risultati scientifici estremamente innovativi. Queste sono certamente tra le motivazioni principali che hanno spinto a intraprendere il programma di ammodernamento della beamline ID08, trasformandola nell'odierna ID32. L'idea principale è quella di creare una struttura all'avanguardia per lo studio delle proprietà magnetiche ed elettroniche dei materiali mediante raggi X molli. Tra le possibili tecniche di misura si è deciso di dare la precedenza a quelle che avevano già rappresentato il punto di forza della vecchia ID8, attraendo l'attenzione di molti scienziati: lo scattering anelastico risonante di raggi X (RIXS dall'inglese *Resonant Inelastic X-ray Scattering*) e il dicroismo circolare magnetico (XMCD dall'inglese *X-Ray Magnetic Circular Dichroism*). Così la nuova beamline si suddivide in due rami differenti, uno dedicato al RIXS e uno all'XMCD. Il primo di questi è ancora nel pieno della fase di test e dovrebbe essere operativo per luglio 2015, mentre il secondo ha visto il suo primo esperimento a novembre 2014.

Durante il lavoro di tesi, svolto presso il Dipartimento di Fisica del Politecnico di Milano, ho seguito i recenti sviluppi della beamline concentrandomi in particolare su due temi molto diversi: da una parte il miglioramento dell'acquisizione di uno spettro RIXS e dall'altra la partecipazione al primo esperimento XMCD di ID32 e la successiva analisi e interpretazione dei dati.

Il nuovo spettrometro RIXS della beamline, che si chiama ERIXS, è stato esplicitamente progettato per raggiungere una risoluzione senza precedenti altrove e con un anticipo di un paio di anni rispetto ad altri progetti RIXS paragonabili in altre strutture. La promessa che si vuole mantenere è quella di arrivare a distinguere 30 meV all'edge L_3 del rame (situato a circa 930 eV) che è circa quattro volte meglio di quanto si riesca a fare oggi. Nonostante la grande complessità del progetto lo schema ottico dello strumento è molto semplice: la radiazione emessa dal campione viene dispersa da un reticolo di diffrazione a passo variabile e focalizzata su di un sensore di immagine. In questo modo l'intero spettro può essere acquisito in parallelo e si crea una corrispondenza diretta tra l'asse delle energie e la posizione sul detector. La risoluzione di quest'ultimo ha un ruolo fondamentale nel determinare le prestazioni complessive dello spettrometro. Una scelta condivisa è quella di utilizzare come detector un sensore CCD (da *Charge Coupled Device* ovvero dispositivo ad accoppiamento di carica). Esistono molte alternative commerciali ottimizzate per lavorare coi raggi X, che sono molto versatili e garantiscono un fondo di rumore molto basso. Sfortunatamente la miglior risoluzione che si riesce ad ottenere da questi dispositivi è intorno ai 20-25 μm indipendentemente dalla dimensione del pixel. Il motivo di ciò è il frazionamento tra più pixel della carica generata da un singolo fotone. L'assorbimento di un fotone nella zona attiva del dispositivo genera infatti una nuvola elettronica che, mentre viene raccolta dai pixel, diffonde lateralmente sparpagliandosi tra molti di essi e peggiorando la risoluzione. Ciononostante in questa situazione è il problema stesso a suggerire una possibile soluzione. Infatti se la carica della nuvola elettronica viene suddivisa tra diversi pixel, possiamo pensare che il punto d'arrivo del fotone coincida con il centro di massa delle intensità dei pixel coinvolti, facendo l'ipotesi che esse siano proporzionali alla distanza dal punto di impatto. In questo modo è possibile posizionare i singoli fotoni con una precisione inferiore al pixel. Le prestazioni di questo semplice algoritmo sono state verificate sperimentalmente con un piccolo setup sperimentale, consistente in una sorgente di raggi X tradizionali, una lama di rasoio e il CCD che sarà montato su ERIXS, con pixel da 13.5 μm. La lama di rasoio copriva parzialmente la superficie del sensore oscurandone una porzione. La risoluzione spaziale è stata determinata stimando la larghezza della transizione ombra-luce nelle immagini. In questo modo siamo riusciti a riprodurre risultati precedenti misurati sullo stesso setup che vedevano un miglioramento della risoluzione da circa 20-25 μm a valori intorno ai 7 μm utilizzando il calcolo del centro di massa. Tuttavia un grosso svantaggio di questo metodo è che funziona soltanto se nuvole di carica di fotoni diversi non si sovrappongono, quindi occorre acquisire immagini molto più frequentemente e mantenere bassa la densità dei fotoni, cosa che porta a un generale calo dell'efficienza della misura. Un miglioramento di questa situazione può essere ottenuto leggendo la matrice di pixel più frequentemente, abbiamo quindi provato ad utilizzare la modalità di lettura più veloce fornita dal CCD (la frequenze di lettura dei pixel in modalità veloce è 1 MHz contro i 100 kHz della lettura lenta). Un fatto inaspettato è che ciò comporta, nel nostro modello di CCD, la comparsa di un fondo disomogeneo, che tuttavia siamo riusciti a rimuovere tramite l'aquisizione e sottrazione di immagini buie. Ci aspettavamo invece un aumento del rumore di lettura, come riportato dal datasheet, da circa 3.5 a 10 elettroni per pixel. Nonostante ciò l'utilizzo del calcolo del centro di massa ha permesso un notevole miglioramento della risoluzione ottenendo un valore di 8.5 μm con la miglior scelta dei parametri software. Su di un set di immagini siamo anche riusciti a stimare un valore di 5 μm di risoluzione che è tuttavia inspiegabilmente basso se confrontato con i valori della lettura lenta e le successive simulazioni Monte Carlo. Queste ultime si sono rivelate essere un utile strumento per lo studio della dipendenza della risoluzione dal rumore di lettura, per diverse dimensioni del pixel e energie dei fotoni incidenti.

Nonostante i risultati incoraggianti sul miglioramento della risoluzione, le immagini ricostruite tramite l'algoritmo del centro di massa soffrono la presenza di alcuni artefatti. Questi sono dovuti al fatto che il calcolo del centro di massa tende a spostare il punto di impatto del fotone verso il centro dell'ipotetico pixel centrale della nuvola di carica, svuotando in questo modo la regione a bordo pixel. Avviene quindi che, nelle regioni uniformemente illuminate, le immagini ricostruite mostrino fastidiose oscillazioni di intensità con periodicità di un pixel. Abbiamo quindi sperimentato l'utilizzo di due algoritmi che permettono di compensare l'errore sistematico generato dal calcolo del centro di massa, tramite un'opportuna correzione statistica della posizione dei fotoni. Il primo algoritmo provato si chiama η e lavora con macchie 2×2, mentre il secondo, che abbiamo battezzato β, è semplicemente una estensione di η mediante l'uso di matrici 3×3. Grazie ad ulteriori simulazioni abbiamo dimostrato che gli algoritmi η e β sono entrambi in grado di correggere completamente gli artefatti dati dal centro di massa, ricostruento quindi perfettamente una regione con illuminazione omogenea. Inoltre l'analisi dell'errore medio totale in funzione del rumore di lettura ha permesso di stabilire che alternativamente η oppure β riescono a superare i risultati dell'algoritmo del centro di massa a qualsiasi valore di rumore fino a 12 elettroni. Una volta verificate le potenzialitá degli algoritmi η e β la fase successiva sarà la loro messa a punto su immagini reali misurate col nostro setup e direttamente sulla beamline.

Lo sviluppo del RIXS ha permesso recentemente la scoperta e lo studio di fenomeni molto interessanti nei cuprati superconduttori ad alta temperatura critica. Questi materiali possiedono proprietà molto peculiari e mostrano fluttuazioni delle cariche e degli spin che costituiscono uno dei più grandi enigmi della fisica della materia condensata. Una caratteristica che accomuna i cuprati e si pensa quindi sia fondamentale per l'insorgere della superconduttività è la presenza di piani CuO_2. Ognuno dei loro ioni Cu^{2+} si trova in una configurazione $3d^9$ caratterizzata da un elettrone spaiato nella shell esterna. Ciò fa si che al loro interno si sviluppi un ordine ferromagnetico a lungo raggio. Un più lieve accoppiamento magnetico tra piani CuO_2 consecutivi fa anche sì che l'antiferromagnetismo si estenda in tre dimensioni. L'ordine a lungo raggio è tuttavia velocemente soppresso all'aumentare del drogaggio. In realtà gli spin degli atomi di rame non giacciono perfettamente nel piano CuO_2 ma sono invece lievemente inclinati a causa dell'interazione di Dzyaloshinsky-Moriya generando quindi un piccolo momento magnetico perpendicolare ai piani. La magnetizzazione netta dovuta a queste componenti è tuttavia nulla perché i momenti di piani successivi si accoppiano antiferromagneticamente tra loro. Eppure basta applicare un campo magnetico sufficientemente forte per orientare parallelamente i momenti e svelare il ferromagnetismo debole che era prima nascosto. La tecnica dell'XMCD è molto utile per studiare questi sistemi e ha recentemente dimostrato che questo debole ordine ferromangetico sopravvive anche al drogaggio in diverse famiglie di cuprati. In questo contesto abbiamo portato a termine un esperimento per studiare la dipendenza dalla temperatura del segnale XMCD in campioni di $La_{2-x}Sr_xCuO_4$ e $NdBa_2Cu_3O_{6+x}$ *underdoped* e *optimally doped*. Questo è stato inoltre il primo esperimento XMCD ad ID32 e pertanto costituiva un test di tutto l'apparato sperimentale in una situazione reale. Sebbene la qualità generale degli spettri di assorbimento fosse eccellente, abbiamo riscontrato una piccola deriva della scala delle energie e una non linearità nella misura dell'intensità della radiazione in ingresso. Nonostante le difficoltà nella misura di effetti XMCD minori dell'1% della XAS su di una beamline completamente nuova siamo riusciti a raccogliere una consistente quantità di dati. All'edge L_3 del rame nell'NBCO abbiamo osservato un comportamento tipicamente paramagnetico dell'XMCD in dipendenza dalla temperatura, che è in accordo con alcuni risultati di letteratura. Tuttavia abbiamo anche riportato la presenza di un segnale XMCD a temperatura ambiente, che non era mai stato osservato prima. Inoltre abbiamo anche misurato per la prima volta, per quanto ci è dato sapere, il segnale XMCD dell'edge K dell'ossigeno nell'NBCO. I dati dell'ossigeno sembrano confermare quelli all'edge del rame, tuttavia la loro interpretazione è meno diretta avendo gli spettri una forma molto più complicata e un'intenstità molto minore.

Contents

List of Figures

List of Tables

Chapter 1

CCD technology for RIXS

Resonant Inelastic X-ray Scattering is a powerful experimental technique to probe magnetic and electronic excitations in materials. In recent years, thanks to the development of new synchrotron sources and dedicated equipment, it has demonstrated to be able to produce groundbreaking results by itself and integrated with other investigation techniques. As RIXS is a spectroscopic method, the ultimate quality of the measures it produces is determined by the final spectral resolution. A commonly adopted acquisition method consists in using a spectrometer to disperse light on a CCD, thus establishing a direct correspondence between the positions on the sensor and the spectral components. It follows from this assertion that the CCD resolution influences directly the instrument resolving power, and it is thus an important parameter to optimize. Different methods have been tested in order to enhance the detector resolution and their discussion is one of the main topics of the present thesis. However, in order to comprehend the main results we expose, a basic understanding of RIXS technique and the working principles of a CCD is necessary. In this chapter, after a general presentation of RIXS, we give a brief description of the ID32 beamline and the ERIXS spectrometer, focusing on the aspects that produce the final spectral resolution. Afterwards we summarise the basic structure and operating principles of a CCD and the technological solutions needed to employ this kind of sensors in the soft X-ray range. Finally we briefly describe the specific detector we used to test the acquisition algorithms explained in next chapter.

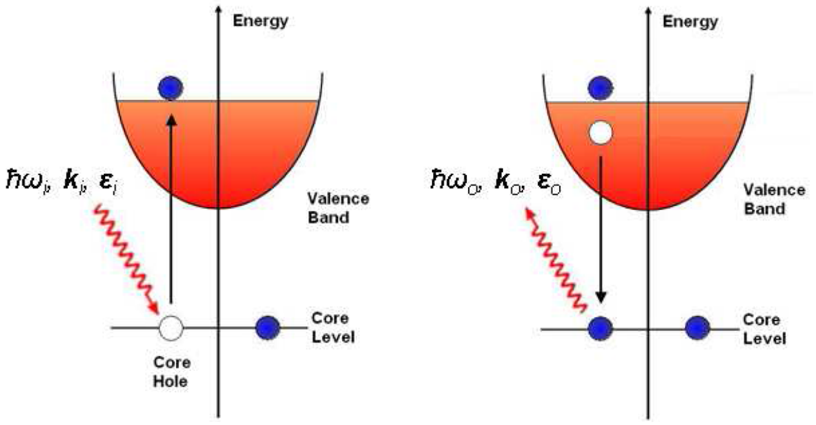

Figure 1.1: The two steps of RIXS scattering process. The incoming photon excites a core electron to an empty state of the valence band (left panel). The excited state is unstable and rapidly decays emitting a photon (right panel). Image taken from [40].

1.1 RIXS spectroscopy

We describe how RIXS spectroscopy works starting from its name: *Resonant Inelastic X-ray Scattering.* First of all RIXS involves a scattering process, meaning that an incident beam is modified by the interaction with a sample that is excited by the radiation. Specifically RIXS is a photon *in*-photon *out* spectroscopy, which means that we measure the light emitted by the sample upon its irradiation. In particular the scattering measured by RIXS is a second order process and can be thought of as involving the two steps depicted in Fig.(1.1). First the incoming X-ray photon, characterized by its energy $\hbar\omega_i$, momentum $\mathbf{k}_i$ and polarization ϵ_i, is absorbed by the system, promoting a core electron to an empty valence state above the Fermi level (left panel). The created excited state is unstable (its lifetime is about 1 fs) and rapidly decays by recombining the core hole with a valence electron. During the process a photon is emitted with energy $\hbar\omega_o$, momentum $\mathbf{k}_o$ and polarization ϵ_o (right panel). As the process involves two steps RIXS is able to observe excitations that are forbidden by dipole selection rules, but this is also a disadvantage as the cross-sections are small and require a very high photon flux. At the end of the process the system may be left in the ground or in an excited state: the first case is called elastic scattering and $\hbar\omega_i = \hbar\omega_o$, whereas in the second case part of the energy of the incoming photon is transferred to the system excitation and $\hbar\omega_o < \hbar\omega_i$. This scattering is called inelastic as it involves an *energy loss.* The RIXS spectrum, which gives information about the possible excitations, is represented by the measured intensity as

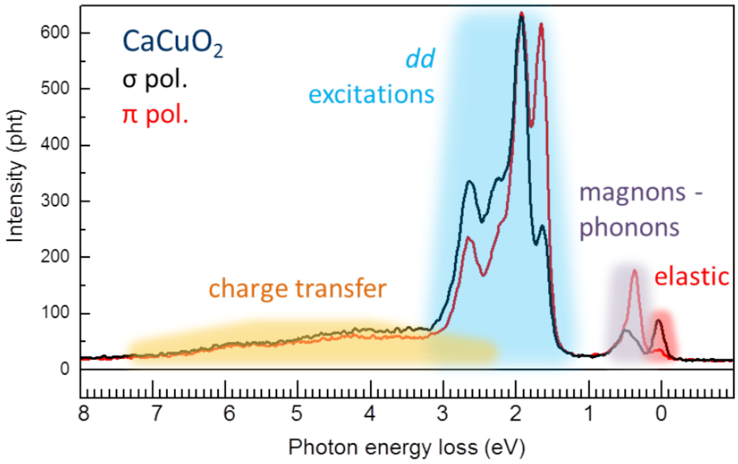

Figure 1.2: Example of a typical RIXS spectrum, measured on a $CaCuO_2$ sample. The most relevant excitations investigated by RIXS are highlighted. The two curves correspond to two different and orthogonal polarizations of the incoming radiation. Image taken from [1].

a function of the energy loss $E_{loss} = \hbar\omega_i - \hbar\omega_o$. Furthermore the geometry of the experiment fixes the direction of the momentum of the incoming and outgoing photons and determines the momentum transfer in the excitation process. RIXS is very powerful because it gives information on both the energy loss and the momentum transfer connected to the excitations, thus spectra are often visualized as 2D colour maps as function of these two relevant parameters. The energy and the wave-vector of the excitations can be retrieved thanks to the conservation laws of energy and momentum:

$$\begin{aligned} \hbar\omega_i &= \hbar\omega_o + E_{ex} \\ \hbar\mathbf{k}_i &= \hbar\mathbf{k}_o + \hbar\mathbf{q}_{ex} \end{aligned} \tag{1.1}$$

The properties of the incoming photons are precisely known whereas the ones for the outgoing photons are measured. The last important parameter in order to fully characterize the process is the polarization of the outgoing photons ϵ_o which is often not measured. Being a photon *in*-photon *out* technique RIXS does not modify the total neutrality of the samples and ensures the absence of charging problems in insulating systems, which are a main drawback of other spectroscopic techniques.

We now need to define what resonant means. If we observe the absorption spectrum of a system, it is characterised by edges that are visible through a sudden increment of the absorbed radiation and occur when the energy of the incoming photon corresponds to the energy jump between a core level and the valence band. As the energy levels are a chemical signature of the atoms, with RIXS we can tune the incoming photon energy to select a specific chemical element and study the excitations from its point of view. Furthermore the absorption edges are modified by the chemical environment, so if the same element is present in more configurations within the structure, RIXS is able to distinguish among them to a certain extent. The use of RIXS with soft X-rays has demonstrated to be very useful, because in this energy range, roughly considering photons from 400 eV to 1600 eV (this is the tunable energy range of ID32), we find the O K edge, the $L_{2,3}$ edges of $3d$ transition metals, for example copper, and the $M_{4,5}$ edges of rare earths. Fig.(1.2) shows a typical RIXS spectrum measured at the Cu L_3 edge of $CaCuO_2$ which involves electron excitation from the $2p_{3/2}$ core level to the $3d$ valence shell. As we can see, most of the spectrum is included in a few eV energy loss from the elastic peak. The plot also highlights some of the excitations that can be probed at this edge, which consist of charge transfer, magnetic, lattice and ligand field excitations. A further possibility of RIXS is to study the polarization dependence of the spectrum. The two curves in figure are measured with two orthogonal linear polarizations (σ is perpendicular and π is parallel to the scattering plane, see for example [41] for a typical experimental geometry) and the spectral peaks are enhanced or suppressed depending on the polarization of the incoming photon.

RIXS instrumentation

Now that we have briefly outlined the physical principle, it is important to introduce how a RIXS measurement is carried out practically, that is how the experimental equipment works. We should focus our attention to the main parameters determining spectral resolving power and the reasons why it is so important to enhance the CCD resolution, which constitutes the main motivation of this thesis work.

In the last 20 years RIXS spectroscopy has seen important advances in photon flux and resolving power due to the introduction of third generation synchrotron sources and specifically designed equipment. The radiation intensity on the sample is very important for RIXS, which, relying on a second order process, requires a remarkably high photon flux and it is often described as *photon hungry.* On the other hand a higher resolving power allows to distinguish small spectral features

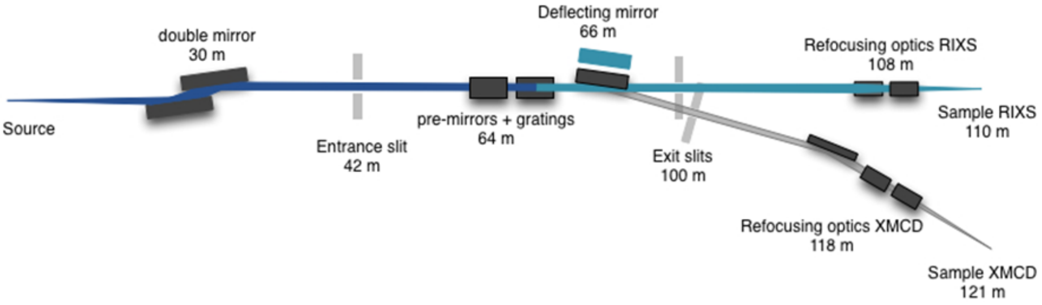

Figure 1.3: Optical schematic of the ID32 beamline at the ESRF. Taken from [3].

and is thus essential in the study of system excitations. One of the most important current RIXS projects is the ERIXS spectrometer at the ID32 beamline of the ESRF. The instrument has been designed by Prof. G. Ghiringhelli, the leader of our group at Politecnico di Milano, and coworkers, and it was conceived to provide a huge enhancement of the spectral resolution available nowadays. Previous spectrometers designed by the same group, that can be considered ERIXS predecessors and share the same optical layout with it, are AXES, which is now dismissed and was placed in the old ID08 beamline of ESRF, and SAXES [21] at the ADDRESS beamline of the Swiss Light Source (SLS), currently working and holding so far the record of the best resolving power, giving a resolution of around 130 meV at the Cu L_3 edge [41].

The ID32 beamline was built to replace ID8 according to the ESRF upgrade programme and keep its role of spectroscopic investigation of magnetic properties and electronic structure of materials using soft X-rays. Actually it is the only beamline at ESRF working in the soft X-rays range, with a tunable energy between 0.4 and 1.6 keV, which makes it particularly suitable for studying the L and M edges of transition metals and rare earths. Two main different spectroscopic techniques are used in the beamline, which separates into two branches leading to the XMCD and the RIXS end-stations. A simple schematic of ID32 is shown in Fig.(1.3), which evidences all its optical elements. The electron source is constituted by three APPLE II undulators tunable in energy that can provide 100% polarized light with right/left circular and horizontal/vertical linear polarization. A double mirror focuses the beam inside the entrance slit of the optics hutch, which contains the two gratings (one for XMCD, the other for RIXS) that work as monochromators and a moving deflecting mirror allowing to direct the

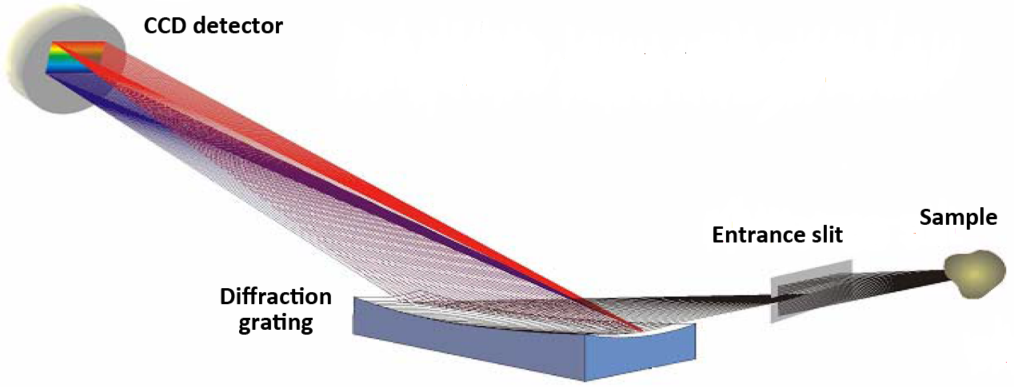

Figure 1.4: Optical layout of a RIXS spectrometer. The light coming from the sample enters the instrument through the entrance slit and is dispersed and focused by a VLS concave grating towards the CCD detector.

beam either to the XMCD or to the RIXS end-station. The two monochromators are both variable line spacing (VLS) gratings and the one for XMCD also has a sagittally refocusing mirror. For the moment we limit our description to the RIXS branch whereas the XMCD one is described in the last chapter, when presenting some experimental results. The beam comes out from the optics hutch through the exit slit and is focused on the sample. The total distance between source and sample is 110 m.

As RIXS implies a spectral measurement, the most important part of the experimental setup is the spectrometer which separates the various components of the radiation emitted by the sample and acquire them. ERIXS, as well as its predecessors, was designed following the logic of simplicity and reliability and all the three instruments have the same basic optical layout shown in Fig.(1.4). The source of the spectrometer is constituted by the sample itself that decays emitting photons, which are collected by the instrument through the horizontal entrance slit. The aim of the entrance slit is to reduce the source size and hence decrease its image on the grating. However, as ERIXS has been designed to give a spot size of $4 \times 60\,\mu\text{m}^2$ (vertical × horizontal direction) on the sample, the use of the entrance slit is unnecessary during measurements. The heart of the spectrometer is represented by a concave diffraction grating which works at grazing incidence and it is the only optical element of the system. It has the dual task of dispersing the radiation and focusing it on the 2D position sensitive detector. In general applications radiation dispersion is obtained through Bragg crystals but this is unluckily impossible for soft X-rays because of the lack of

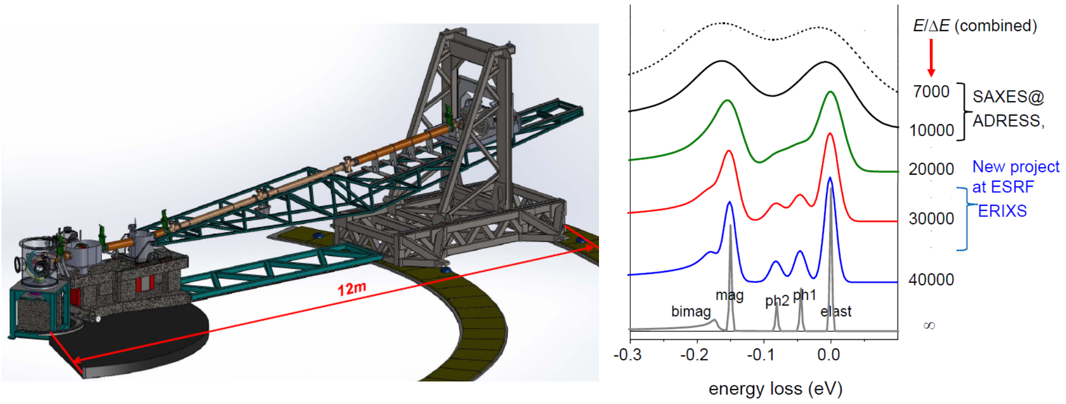

(a)

(b)

Figure 1.5: (a) 3D rendering of the ERIXS spectrometer. (b) The plot shows how a true excitation spectrum is observed by a RIXS spectrometer with increasing resolving power from top to bottom. The collocation of SAXES and ERIXS in the diagram is shown next to the scale.

crystals with the desired lattice constant. Hence the common solution is to use a VLS diffraction grating which works more or less as the monochromator, where the variable line spacing makes it possible to reduce all higher order optical aberrations. The grooves of the grating are horizontal and perpendicular to the direction of the photons, which, arriving at grazing incidence, are vertically dispersed by them and focused on the detector; in order to focus radiation the grating is slightly concave and the detector should be put on its focal plane to minimize the linewidth. As the deflecting angle depends on the photon energy, the vertical position on the detector is in direct correspondence with the energy loss. Thus the use of a position sensitive detector allows to acquire all the interesting region of the spectrum in parallel and the image on the detector is made up of horizontal isoenergetic lines parallel among each other, whose vertical position is directly related to the photon energies. According to the spectrometer design a 2D position sensitive detector is needed and the solution chosen for ERIXS is a commercial thinned back-illuminated CCD for soft X-rays, that is described in details in the next sections. The CCD resolution is extremely important because it represents the exit slit of the system, which contributes to the combined resolving power. Actually experimental tests (see next sections and [19]) have demonstrated that CCD resolution is about 25 μm irrespective of the pixel size, although it can be improved by using the CCD at grazing incidence. In ERIXS the angle formed by the detector surface with the tangent of the focal curve [21] is $\gamma = 30°$ meaning that we have to multiply the calculated CCD resolution by $\sin(\gamma) = 1/2$.

The combined spectral resolution of the system is determined by the two contributions ΔE_{BL} and ΔE_{SPEC} respectively given by the beamline and the spectrometer, which have to be summed quadratically:

$$\Delta E_{TOT} = \sqrt{\Delta E_{BL}^2 + \Delta E_{SPEC}^2} \tag{1.2}$$

The beamline contribution ΔE_{BL} is determined by the RIXS monochromator, which has been designed to reach a goal resolving power of 42000, that means a resolution of $\approx 22\,\mathrm{meV}$ at the Cu L_3 edge. The spectrometer term ΔE_{SPEC} is composed by three main contributions (which once again are summed quadratically): the finite source size, depending on the focus of the beam on the sample, the slope error of the grating and the detector resolution. The limiting factor of the combined resolving power of ERIXS, as it was for SAXES, is the detector resolution, because it is fixed at around $25\,\mu$m and cannot be enhanced by reducing the pixel size. For this reason it is of paramount importance to explore alternative ways to improve the resolution. A possible strategy is to use the *single photon counting* (SPC) algorithm described in next chapter, which is able to reconstruct the photon positions with subpixel accuracy. In the first measurements, in non-optimal conditions and without using SPC, ERIXS is expected to provide a final resolution of about 60 meV at the Cu L_3 edge. However in the target scenario the resolving power of the instrument is 30000, which means $\approx 30\,\mathrm{meV}$ spectral resolution, that is three to four times better than SAXES. This requires a detector resolution around $7\,\mu$m, which would be achievable using SPC as we demonstrate in Chapter 3. In order to reach the goal resolving power a high photon flux is essential, because the gain of a factor two in spectral resolution, from 60 meV to 30 meV, means an intensity loss of an order of magnitude (probably a factor between 20 and 30). It also has to be stressed the difference between spectral resolution and definition. The resolution is represented by the instrumental widening of the ideal spectral features and is usually estimated as the FWHM of the elastic peak of a sample of graphite. Spectral definition has to do with the sampling period of the final spectrum. In the target scenario of 30 meV resolution the scale conversion on the detector is 17 meV/pixel. The number of points per pixel depends on the algorithm used. The traditional algorithm (see next chapter for details) uses the technique of channel doubling that means two points per pixel. In the SPC algorithm the number of sub-channels can be chosen arbitrarily, but it should be set as a trade-off between definition and intensity, because if we increase the number of subpixels, the same number of photons is divided among more channels. In the experimental tests carried out in Milano, we were using 7 subpixels.

Although conceptually simple, the practical design of ERIXS layout, shown in Fig.(1.5a), was not so straightforward. The total length of the instrument is approximately 12 m and one of the main challenges was represented by the necessity of moving the long arm in order to change the scattering angle on an interval of 100°. The best solution found was to lift the structure micrometrically and make it slide on two marble rails thanks to a thin cushion of air.

The necessity of improving the resolving power of RIXS instrumentation is outlined by the plot in Fig.(1.5b), which shows how a true energy loss spectrum (grey line) is smeared out by the acquisition system depending on its resolution. ERIXS would represent a big improvement with respect to SAXES, allowing to resolve smaller spectral features and potentially observe new excitation processes ignored so far.

1.2 CCD structure and operating principles

The Charge Coupled Device is an image sensor, *i.e.* a system with spatial resolution that converts the radiant energy it receives into an electronic signal; it was first designed in 1969 by William Boyle and George E. Smith while working at the AT&T Bell Labs. The spatial resolution is obtained by a matrix of equal elements (pixels) that collect an electric charge proportional to the incoming flux of photons. Each pixel is realized through a Metal-Oxide-Semiconductor (MOS) heterojunction.

MOS capacitor in deep depletion regime

The general MOS structure is shown in Fig.(1.6a) and is composed of three layers: a *p*-doped silicon substrate, a silicon oxide (SiO_2) insulating layer and a metal contact called *gate*. By applying a voltage V_G to the latter the electronic properties change accordingly and various working regimes can be identified. We recall that in order to ensure charge accumulation the MOS capacitor has to be operated out of equilibrium in *deep-depletion* regime. Starting from the accumu-

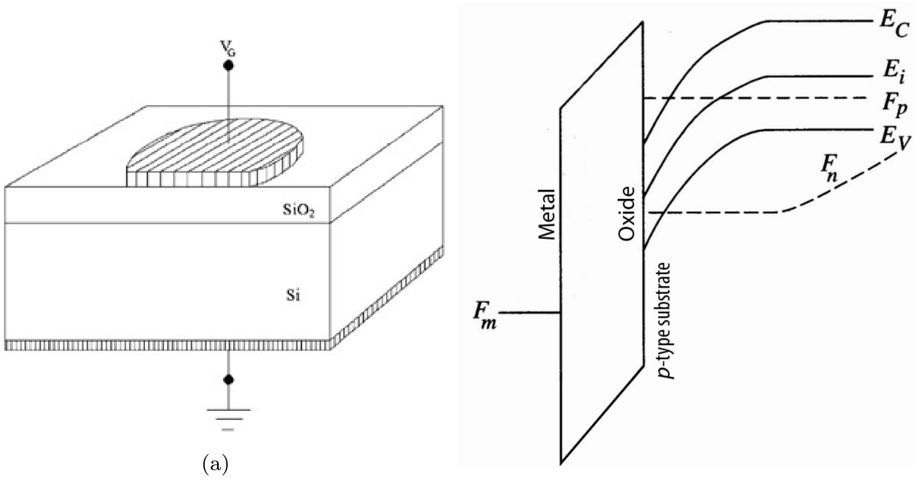

(a)

(b)

Figure 1.6: MOS capacitor structure (a) and out of equilibrium band diagram (*deep depletion* regime) exhibiting band bending (b).

lation regime, V_G is rapidly commuted to a voltage higher than the characteristic threshold V_T and the bands bend as sketched in Fig.(1.6b), where E_C and E_V are the conduction and valence band respectively while F_p and F_n represent the Fermi quasi-levels of holes and electrons. This situation occurs exactly after gate commutation and the Si-SiO$_2$ interface is immediately depleted of electrons, which are minority carriers in p-doped silicon, leaving an almost zero concentration near the oxide. In order to restore the equilibrium of Fermi quasi-levels an accumulation of electrons at the interface is necessary and two different processes can occur: drift-diffusion of electrons from the bulk and electron-hole pairs generation. We are interested in the latter phenomenon because it can be brought about by light irradiation. A photon with energy $h\nu$ larger than the gap (the gap of Si is 1.11 eV at 300 K) can be absorbed promoting an electron from the valence to the conduction band. The electron-hole pair is separated by the electric field within the depleted region and cannot recombine, thus electron accumulation at the interface is possible. Highly pure silicon crystals and low temperature ensure that thermal generation and diffusion from the bulk are negligible, so that the charge accumulated under each pixel is proportional to the incoming photon flux.

Charge transfer mechanism

In order to accomplish the acquisition of the image, the charge stored in each pixel has to be measured and converted to an electronic signal. This can be done

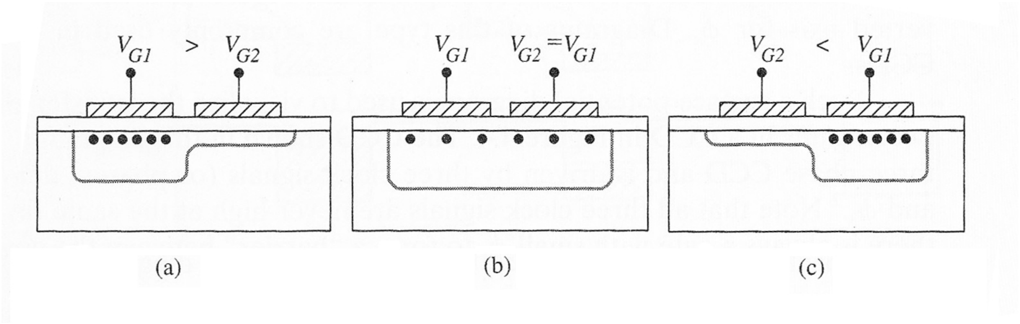

Figure 1.7: Charge coupling mechanism for transferring electrons between adjacent MOS capacitors. Taken from [26].

by shifting the charge from pixel to pixel towards one end of the device, where it is measured sequentially. The underlying mechanism that allows charge transfer between neighbouring pixels is called *charge coupling*, from which the entire device takes its name. A simple representation is shown in Fig.(1.7), in which we consider two adjacent MOS capacitors. A gate voltage $V_{G1} > V_T$ is applied to the left one allowing charge accumulation at the silicon-oxide interface, whereas the second is kept at $V_{G2} < V_T$ preventing it. Charges are confined in a potential well under the left pixel (Panel (a)) because of the energy barrier resulting from the different gate voltage applied, thus they cannot flow to the pixel on the right. If V_{G1} is raised to V_{G2}, the confining electric field is no longer present and the charge can distribute equally in the two MOS (Panel (b)). Finally V_{G2} is lowered below V_T and the initial situation is reversed; now the charge is fully confined within the right pixel (Panel (c)). Charge coupling is the basic process in the reading mechanism for the whole matrix. After exposure to radiation, the charge of the bottom pixel row is moved to a serial shift register and all the other charges are consequently shifted one row down. Finally the electrons in the serial register are transferred sequentially to a charge-to-voltage converter and amplifier and can be digitized hereafter. The process ends when all the CCD matrix has been recorded. Moreover in many detectors the explained charge transfer process is not performed directly by the accumulating elements. Instead charge is transferred to dedicated registers once the exposure is finished. With this technique it is also possible to start a new exposure, while the previous one is being acquired.

It already follows from this introduction how critical the readout process can be for measurements, as for example RIXS spectra, in which the duty cycle

is essential. The duty cycle can be defined as the ratio of exposure time over the total time necessary to acquire an image, thus it strongly depends on the exposure time itself and on the readout speed of the device. Having a high duty cycle is important for many reasons. First of all it is strictly connected with the efficiency and allows faster data collection. Furthermore a low duty cycle might also lead to image modification; if the readout time were much longer than the exposure, most of the charges would be generated while reading the image. In this stage, as the electrons are shifted with respect to the pixel matrix, new photons hitting the detector before acquisition finishes would be assigned to the wrong pixel. This problem however is effectively solved by using a shutter that stops the beam while reading the pixel matrix.
In order to avoid a loss in duty cycle exposure time should not be too short, but at the same time it has to assure a low photon density on the image, required by the processing algorithms. Boosting the readout speed seems the best solution to improve the duty cycle, although as we shall see in Chapter 3, this implies some other problems to cope with.

1.3 CCD detectors for soft X-rays

Thinned back-illuminated CCDs

If I_0 is the radiation intensity incident on the sensor it is possible to define the incident photon flux $\phi_0 = I_0/h\nu$, which undergoes an exponential decay inside the material due to absorption according to Beer-Lambert law:

$$\phi(x) = \phi_0 \mathrm{e}^{-\alpha x} \tag{1.3}$$

The active region inside the semiconductor, in which photogenerated electrons contribute to charge accumulation extends for a length $W + L_n$ from the interface with the oxide layer, where W is the length of the depleted region and L_n the diffusion length of the electrons. In soft X-ray range the absorption coefficient is $\alpha \gg 1/(W + L_n)$, meaning that most of the radiation is absorbed within the thickness of the active region and contributes to the signal. The problem is that in typical CCDs, optimized for infrared or visible light detection, the radiation impinges on the gate side of the device so that it has to cross the metal and oxide layers before reaching the active region. Soft X-rays, due to their

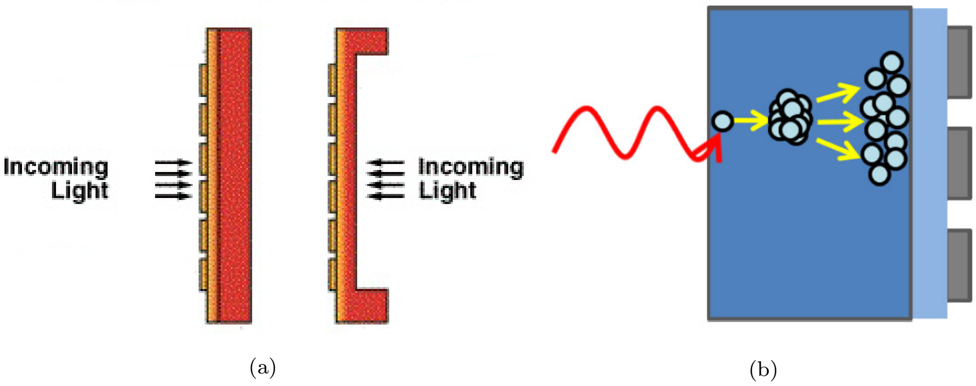

(a) (b)

Figure 1.8: (a) Comparison between a front and a thinned back-illuminated sensor. (b) Charge cloud splitting: a photon hitting the detector generates a charge cloud which splits among many pixels.

large absorption coefficient, cannot reach the substrate because they are almost completely absorbed within the thickness of the first layers before getting through to the active region. This difficulty has been overcome by development of thinned back-illuminated detectors. As the name says, this kind of device is illuminated from the back *i.e.* from the substrate side. As this layer is way thicker than the active region, the device has to be thinned by etching down to a thickness of 10-25 μm to be well matched to the X-ray absorption length: not too thin to avoid being semi-transparent, not too thick to maximize the photon absorption in the active region next to the Si-SiO$_2$ interface. A comparison between the front and thinned back-illuminated geometries is depicted in Fig.(1.8a).

Charge cloud splitting

If we expose the CCD to a uniform X-ray photon source and keep the photon flux low enough, instead of getting a flat intensity map, we can distinguish individual charge clouds corresponding to single photon events (as we shall see this is the working condition we need in order to apply single photon counting algorithms). Clouds corresponding to a single photon are split among several pixels worsening the effective spatial resolution of the detector, which is almost independent of the pixel size, if this is smaller than the charge cloud [19, 38]. The process leading to charge cloud splitting, depicted in Fig.(1.8b) can be broken into three main steps, according to [45]:

1. The energy $h\nu$ of the incoming X-ray photons is larger than the energy gap of silicon, thus the photo-ionized electrons thermalise by scattering

and produce an avalanche of secondary ionizations. The newly generated charges form a charge cloud, approximately spherical, which is smaller than the pixel area, having a diameter $D[\mu\text{m}] = 0.0171(E[\text{keV}])^{1.75}$ according to [31]; that means $D = 0.015\mu\text{m}$ for photons at 930 eV.

2. The cloud propagates to the pixel interface, while laterally diffusing. The entity of this process is dependent on the local electric field strength in the region where the cloud is generated. The stronger field at the interface causes compact clouds, whereas photons absorbed far away from the oxide result in bigger clouds.

3. The charge cloud is split into charge packets by the pixel matrix. The number of pixels involved depends on both the cloud and pixel size and on the impact position. If the photon hits on the border between two neighbouring pixel, the probability of a split event is higher.

In order to give an estimate of the charge lateral size, experiments were performed in the past by our group [21, 19]. The CCD, with 13.5 μm lateral pixel size, was exposed to uniform illumination at low photon flux, generated by a traditional X-ray source with 930 eV photon energy. Thousands of clouds induced by single photon impacts were analysed statistically to get the mean intensity distribution. For each event the centre of mass of the spot was calculated and the relative intensity weight of each pixel (ratio between the charge in a pixel and the charge of the whole spot) was linked to the distance from the centre, generating the histogram in Fig.(1.9), where the two data sequences represent the distribution in the horizontal (black squares) and vertical (red circles) direction. The estimated FWHM of the spot is about 24 μm in each direction demonstrating that charge diffuses isotropically.

CCD detector tested

The CCD camera we tested is a special delivery by *Princeton Instruments* [30] based on PIXIS-XO:2048B. It is a back-illuminated sensor optimized for X-ray detection, having a quantum efficiency [1] higher than 65% in the whole energy range of interest for RIXS applications, which roughly ranges between 500 eV

---

[1] Quantum efficiency is defined as $QE = \frac{\text{Number of revealed photons}}{\text{Number of incoming photons}}$.

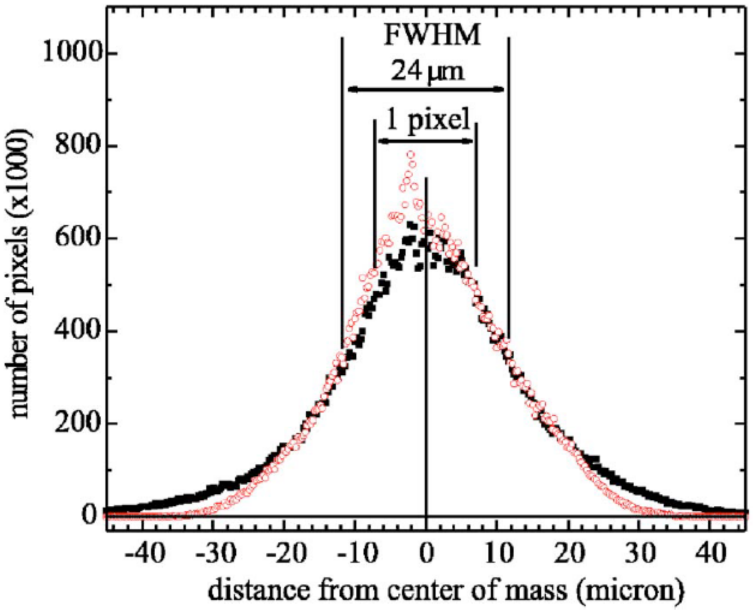

Figure 1.9: Histogram of the charge distribution as a function of the distance from the centre of mass, for single photon events. The two datasets correspond to the horizontal (black squares) and vertical (red dots) directions. Taken from [21].

and 1500 eV. Moreover at the Cu L_3 edge (≈ 930 eV), quantum efficiency reaches its maximum around $QE = 85\%$. This large value of QE is essential to allow measurements with low photon flux and photon-hungry techniques as RIXS. The CCD is arranged in a matrix of 2048×2048 squared pixels with 13.5 μm lateral size, which means a total detecting area of 27.6×27.6 mm^2. The detector is cooled with liquid nitrogen to the working temperature of -110 °C, which is kept constant electronically. Low temperature conditions are fundamental to reduce electron accumulation due to thermal generation and diffusion that contributes to dark current and can saturate the pixels during long exposures. After accumulation, the charge of each pixel is read and transformed to a voltage signal as explained in Section 1.2. Afterwards a constant offset is added to the signal to ensure the output is not negative and finally it is digitized by a 16 bit A/D converter. The acquisition chain can work at two different conversion speeds. The low noise mode works at 100 kHz, whereas the high speed mode, with 1 MHz frequency, gains a factor 10 in the duty cycle but suffers a higher noise and non-uniform background problems.

The two main noise sources in the acquisition process are the dark current and the A/D readout noise. Considering both contributions the total noise affecting the final data can be written as

$$n = \sqrt{d^2_{rms} + r^2_{rms}} \tag{1.4}$$

where n is the total noise, d is the dark current, r is the readout noise and each contribution is specified by its root mean square value (rms) expressed in electrons per pixel. The dark current is due to accumulated charges which are not generated by photo-ionization. According to previous tests [21], this contribution is negligible, amounting to 1 electron/h per pixel, if we work at low temperature. Instead the readout noise, added by the conversion electronics, depends on the chosen reading mode, being 3.39 electron rms at 100 kHz and 10.2 electron rms at 1 MHz (the noise values were supplied by Princeton Instruments in a certificate of performance at the time of manifacture).

Chapter 2

Acquisition algorithms

After radiation exposure the raw images acquired by the detector have to be processed in order to extract the spectral information we are interested in. As detailed in Chapter 1, the experimental geometry we are going to employ in RIXS experiments consists of a diffraction grating which spatially disperses the energy components of the light coming from the sample, determining a direct correspondence between the energy of the photons and the vertical position on the CCD. Therefore raw images consist of parallel horizontal isoenergetic lines, from which the spectral information can be extracted using the algorithms discussed in the present chapter. The *traditional algorithm* is the simplest approach to the problem as it consists in direct intensity integration along the isoenergetic lines. Raw images are only pre-processed by subtracting a mean background and filtering out the single pixels with intensity which is inconsistent with the relevant experimental process; pixels with too high or too low intensity can be due to cosmic rays and noise. This method already gives good results but it has a main drawback: when working with the total integrated intensity the resolution is limited by the charge cloud size, as explained in Chapter 1.

This physical limitation can be overcome by totally changing approach using *Single Photon Counting* (SPC) algorithm. If the impinging rate on the sensor is low, clouds generated by single photons can be identified and analysed separately. The centre of mass (COM) of each photon spot is calculated and localized on the pixel matrix, after upsampling it on a finer grid. This allows a great resolution enhancement, breaking the pixel size limit, provided that we can keep the photon flux low.

However the COM calculation introduces a systematic artefact because it tends to move the centres of the spots towards the centre of the pixels. The η *algorithm*[61] compensates this error in a statistical way, working on spots of 2×2 pixels. An extension of the η algorithm, which we simply call β *algorithm*, can work on larger spots, resulting in a more precise correction in low noise conditions.

The first section of this chapter is a short explanation of the traditional algorithm, focusing on the aspects useful for the understanding of the more advanced techniques. The following sections are devoted to the extensive description of single photon, η and β algorithms, on which the experimental work discussed in Chapter 3 is based.

2.1 Traditional algorithm

The traditional algorithm is a quick and simple procedure to obtain spectra from raw images. It is important for general applications because, although limited in resolution by the size of the charge cloud, it works well in every experimental condition, not requiring a low photon flux. It is also really quick to execute because it works with the integrated intensity not involving a spot search and position reconstruction. The main conceptual steps of the algorithm are the following, which will be then analysed separately:

```
Traditional algorithm
  Image filtering
  Conversion from ADU to photons
  Spectrum integration
```

Image filtering

The first step to carry out on raw images is filtering. As already stated in Chapter 1 the A/D converter adds an offset to the signal, in order to avoid zero line problems during conversion, but this also constitutes a background overlapping the true intensity and thus has to be removed. The offset is evaluated as the mean value of pixel intensities on a dark region of the image (a region not exposed to X-rays) and subtracted from to the total image.

After background removal the image is thresholded in order to discard some spurious contributions that has nothing to do with the true spectrum. First of all each pixel with a signal below the *low threshold* (LT) is set to zero. This is necessary because, after offset subtraction, pixels not involved in charge accumulation still have some small or even negative value due to noise contributions. All these pixels, which clearly have not been involved in a photon hit are set to zero. Anyway LT is usually very small and its absence would not alter results that much.

It happens to find pixels with an intensity which is too high to be compatible with soft X-rays. These events are typically associated with cosmic rays that reach energies in the MeV range (see [65] for a general review). In order to filter out these contributions a *high threshold* (HT) is established above which all pixels are set to zero. Choosing the value of HT may be troublesome with a high photon flux, because charges of photons hitting on the same area stack up generating the so-called multiple events, that can reach a high intensity in some pixels. A too low HT could thus affect the data by removing true signal. On the other hand if HT is too high it is not effective in removing cosmic rays. Another limitation is that their rejection is never perfect because they generate very big spots involving many pixels, where, although the central ones exceed HT, the tails are usually below it leaving some spurious signal on the image. The only solution in this case is to keep the exposure time short as the number of cosmic ray events changes proportionally to it. Anyway the main limiting factor of the algorithm is usually the readout noise and cosmic ray rejection is almost never a problem. As we shall see in next section single photon algorithm does not suffer this problem because it works on single spots and if one of them is identified as being produced by a cosmic ray it is completely ignored. Fig.(2.1) shows a typical RIXS spectral line before (left) and after filtering (right). The offset subtraction is clearly visible, which brings the counts in dark regions back to a value around zero.

Conversion from ADU to photons

Pixel intensity in raw images is expressed in ADU *i.e.* Analog to Digital Units. The converter gain (electrons/ADU) was evaluated experimentally and corresponds to around 2.5. To get physical meaning we prefer to express the intensity

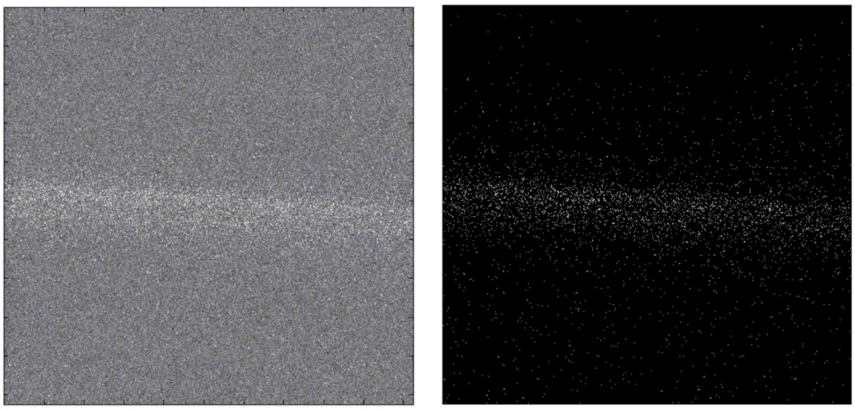

Figure 2.1: Typical experimental spectral line: raw data (left) and after image filtering (right). Reproduced from [1].

in number of photons; given that the average energy needed to generate an electron-hole pair in silicon is 3.6 eV the conversion is simply given by:

$$I[\text{photons}] = \frac{3.6 \cdot 2.5}{Photon\, energy[\text{eV}]} \cdot I[\text{ADU}] \tag{2.1}$$

where we assume that all the energy of the absorbed photon is converted into electrons, forming the charge cloud.

Spectrum integration

After signal filtering and conversion the pixel matrix is ready to be integrated to obtain the spectrum. As the diffraction grating disperses the radiation from the sample, the spectrum reconstruction can be done by summing the pixel charges perpendicularly to this direction, that is along isoenergetic lines. These are not perfectly aligned with the pixel rows as we don't have a precise micrometric control of the detector angle with respect to the grating. Moreover this has the advantage of averaging out efficiency variations between different pixel rows when the signal is integrated. The inclination of isoenergetic lines with respect to pixel rows is specified by a *slope*; in addition, due to optical aberrations, lines are not perfectly straight but slightly curved and so they are described by a discrete equation of this kind:

$$\Delta_j = slope \cdot j + smile \cdot j^2 \tag{2.2}$$

where j is the pixel column index and Δ_j is the vertical shift of the isoenergetic line relatively to the pixel row (Fig.(2.2a)). We can then perform a transformation in which each column is moved vertically by the quantity $-\Delta_j$ in order to

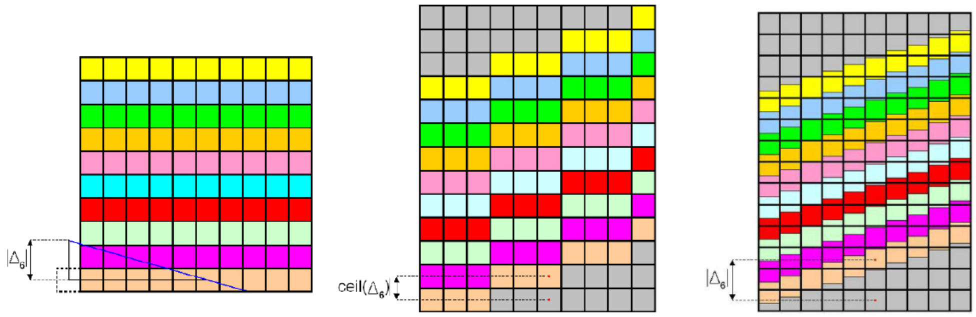

(a) (b) (c)

Figure 2.2: Procedure to bring the isoenergetic lines horizontal with respect to the pixel matrix. Colourful rows represent the charges inside the pixels, the blue inclined line is the isoenergetic line (a). The column shift applied to the matrix can be an integer number of pixels (b) or the exact fractional value (c). In the latter case the intensity of the new cell is calculated through interpolation. Taken from [46].

realign the isoenergetic line with the pixel rows, so that the spectrum can be obtained by simply summing along the rows of the newly defined matrix. One main issue connected with this approach is that Δ_j has to be rounded as the vertical shifts should be integers to define a new pixel matrix (see Fig.(2.2b)). This translates to a maximum error of ± 0.5 pixel in the shifts, determining a loss in spectral resolution.

There is an alternative procedure that avoids rough integer shifts, which is done by interpolation between neighbouring pixels. If we apply a fractional shift to the columns of the old matrix, each cell of the new one contains a portion of two neighbouring pixels, as displayed by Fig.(2.2c). The intensity of the new pixel is defined as the interpolation of the older ones where the weights represent the fraction of the old pixel areas lying in the new cell. After interpolation the spectrum is again obtained by summing along the rows. In order to improve spectral definition *channel doubling* can be also carried out. If we double the number of cells in each column of the new matrix, after vertical shift each old pixel can overlap up to three cells and the new intensity is again evaluated as a weighted sum according to the overlapping percentage. It is important to stress that although doubling the number of experimental points, this procedure does not involve a resolution enhancement because each point is generated by interpolation. The result is only a smoothing of the data that gives a higher definition of the spectrum, because the number of samples is doubled.

2.2 Single photon counting algorithm

An improvement with respect to the traditional algorithm, that can break the resolution limit given by charge cloud size and even by pixel size, is represented by the *Single Photon Counting* technique (SPC). The basic idea behind it is that if the charge cloud is shared among several pixels we can in principle try to identify the centre of the intensity distribution which should correspond, within uncertainties, to the photon impact position. In this way, splitting does no longer constitutes a limiting factor, but allows a resolution enhancement instead.

The relevant difference with the traditional algorithm is on the conceptual level; the previous one considers a continuous radiation and works on the total integrated intensity of many photon events. This allows a high photon flux and long exposures and the best signal-to-noise ratio is obtained working on a single image with stacking of many events. On the other hand the SPC algorithm involves an image reconstruction, where each photon spot has to be analysed separately in order to identify the centre of the charge distribution. To get correct results from this procedure the photon spots do not have to overlap, meaning that we are compelled to keep the photon flux low and the exposure time short. So the final reconstructed image from which the spectrum is calculated is the sum of several short exposures that are put together to have a statistically meaningful signal.

It is important for the following presentation to distinguish between three types of photon events:

- **Split event**: the charge cloud generated by one photon is split between neighbouring pixels. The charge in each pixel is proportional to the distance from the impact position.
- **Single event**: the charge generated by the photon is almost completely accumulated inside a single pixel.
- **Multiple event**: clouds generated by different photons overlaps partially or totally.

It is clear that centroid reconstruction is effective only in the case of split events, as it needs to take advantage of the information stored in more than one pixel. Single events are useless because pixels surrounding the central one carry no information, but their occurrence becomes relevant when pixel size is comparable or bigger than the charge cloud. Multiple events are likewise troublesome, because they alter the evaluation of the spot centre, by assigning to a photon additional charges generated by another one. We implemented the SPC algorithm following these main steps:

```
SPC algorithm
    Image filtering
    Conversion from ADU to electrons
    Spot search
    Centroid reconstruction
    Spectrum integration
```

Before being processed raw images are filtered in a similar way as in the traditional algorithm. Background subtraction, as explained below, becomes more critical for the correct reconstruction of the centroids. Thresholding instead is not carried out at this moment because cosmic rays are rejected during spot recognition. At this point pixel intensity is converted from ADU to electrons just to give a physical meaning to the units; the number of photons will be established by the number of spots recognized. The core of the algorithm, which differentiates it from the traditional one is represented by the spot search all over the image and the subsequent centroid reconstruction for each spot. Afterwards the spectrum is generated in a way only slightly different from before. These steps are described in details in the next subsections.

Spot search

Spot search is a crucial part of SPC algorithm because it has to recognize all the spots generated by photons of the desired energy and distinguish them from charges of other origin, for example cosmic rays or noise. At first, according to the energy range of the photons we are interested in, we have to choose the *high* and *low central pixel threshold* (HCPT and LCPT). Although the charge is spread among many pixels we expect the central one (supposedly the one hit by the photon) to carry the highest intensity. A first screening on the complete image identifies all the pixels candidate to be central pixels of a spot, where the spot is defined as an N×N pixel matrix centred on each of them. In principle the spot matrix does not need to be square, but we are supposing that the charge distribution is isotropic in the horizontal and vertical direction, which is in agreement with experimental data (see Fig.(1.9) and [21]) and with theoretical works that predicts to first approximation a 2D gaussian distribution, although with some corrections [45]. The choice of the spot dimension is a trade-off to minimize the reconstruction error and is dealt with thoroughly in next chapter. The use of two thresholds to identify the central pixels does not guarantee that only the most intense pixel of a spot is considered. If the photon hits on the boundary between two pixels they usually store a similar charge and are identified as two central pixel, so that the same spot is counted twice. Hence a check is carried out that confronts each candidate with the other pixels in the N×N matrix and discard it if it is not the most intense. This procedure is also effective in wiping out cosmic ray spots; central cosmic ray pixels are usually too intense to be considered, but lateral pixels of the spot might be in the right intensity range between the thresholds. However, as they are only lateral pixels, usually they are not the most intense when considering an N×N matrix centred on them, and therefore the spot is discarded.

The method explained for spot recognition works well but it is still susceptible to faults. For example when the impact position is close to the central pixel edge, the higher intensity might be collected by the adjacent pixel causing a wrong recognition of the spot. This can happen because of noise or statistical fluctuations due to the discrete nature of the charge. To avoid this kind of error the spot can be defined alternatively as the N×N matrix containing the highest number of accumulated charges, rather than a matrix centred on the highest intensity pixel. So, after identification of a candidate central pixel, the total intensity of the N×N matrix centred on it is compared to the total intensity of an N×N matrix centred on each of its first neighbours and the true spot is the one with the highest total intensity. The better performance of the first (highest intensity of the central pixel) or the second (highest total intensity) criterion for spot selection is strongly dependent on noise level and pixel size. After recognition, spots are usually separated by intensity using two thresholds: the *low* and *high spot intensity threshold* (LSIT and HSIT). These are a further instrument to select photon events with the expected energy. Spots with a lower intensity can be due to strong noisy contributions, whereas spots which are too high in intensity are the result of multiple events and would lead to a wrong centroid reconstruction.

Centroid calculation

Once the N×N spot has been defined, we have to calculate the centroid of the intensity distribution. Neglecting its true shape, but considering that pixel intensities are in some way proportional to their proximity to the photon impact position, the latter can be in first approximation defined as the *centre of mass* (COM) of the N×N pixel matrix. In terms of image moments [23] the COM is given by:

$$\{x_{COM}, y_{COM}\} = \left\{\frac{M_{10}}{M_{00}}, \frac{M_{01}}{M_{00}}\right\} \tag{2.3}$$

where the general moment M_{ij} is defined as:

$$M_{ij} = \sum_x \sum_y x^i y^j I(x,y) \tag{2.4}$$

in which x, y are the integer pixel coordinates and I is the pixel intensity. In our calculation, considering N×N spots, $-(N-1) < x, y < N-1$ so that for each spot the COM position is specified with respect to its central pixel, which is assigned the location $(0,0)$ within the spot matrix. COM calculation is one of the most used methods to locate the centre of the distribution, because it is simple and computationally very fast, although other methods can be employed, involving for example bidimensional fitting with a 2D gaussian distribution [64]. The COM coordinate, that is relative to the centre of the N×N, is then added to the absolute central pixel position in order to relocate the photon hit on the complete image.

Spectrum integration

The last step of acquisition is spectrum elaboration and, in contrast to the traditional algorithm, SPC does not have to deal with a continuous charge intensity, but directly with the single photon COM positions, specified by a couple of rational numbers (x_{COM}, y_{COM}). However, as before, we still have to carry out an integration along the isoenergetic lines in order to obtain the spectrum; we apply a coordinate transformation to make these lines horizontal, so that integration is

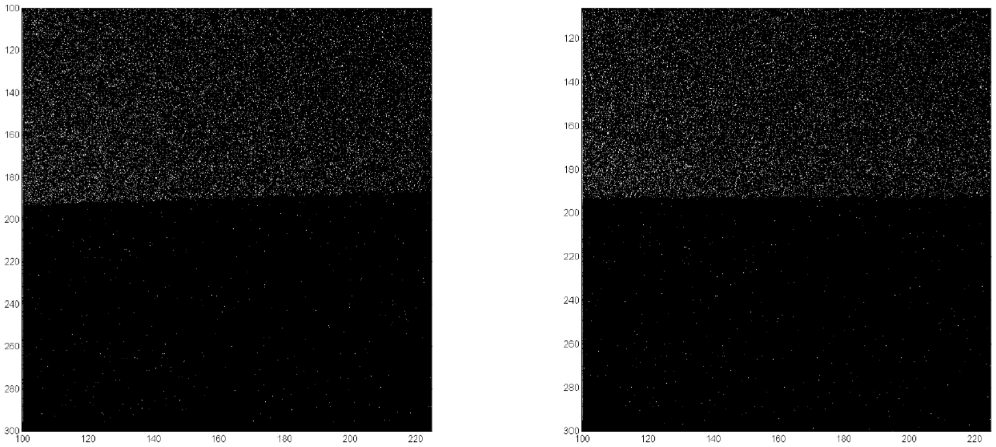

Figure 2.3: Example of COM positions before (left) and after (right) the slope subtraction (vertical shift). Taken from [1].

straightforward. This is done by subtracting from the y_{COM} the corresponding shift of the isoenergetic line Δ_y calculated at x_{COM}. The transformation is the following:

$$\begin{cases} x'_{COM} = x_{COM} \\ y'_{COM} = y_{COM} - \Delta_y \end{cases} \tag{2.5}$$

where $\Delta_y = slope \cdot x_{COM} + smile \cdot x^2_{COM}$. The effect of the transformation on a set of reconstructed images is shown in Fig.(2.3). This is not a spectrum, but it is an image used for the resolution tests described in next chapter. The sensor is partly covered by a razor blade, so the upper part is exposed to radiation and the lower part is dark. The edge of the blade is not parallel to the pixel rows and hence resembles the inclined isoenergetic line that has to be realigned to simplify integration. Actually the spectrum is finally given by the sum of the photons falling along the same isoenergetic line and is produced through the histogram of all the y'_{COM} coordinates of the photons, where the bins are specified by the chosen number of subpixels. For each pixel the calculated spectrum has a number of datapoints equal to the number of subpixel, whereas the spectrum generated by the traditional algorithm has only two points per pixel (because of channel doubling). Hence single photon counting is also improving spectral definition, although the number of sub-channels has to be chosen accurately, not to reduce too much the spectral intensity.

Intensity oscillations and systematic error

As proven experimentally and numerically in the next chapter SPC technique allows a huge enhancement of spectral resolution, which abundantly justify the strict experimental requirement of low photon flux. However centroid reconstruction introduces systematic oscillations in the intensity profile. These are not clearly visible in the final spectrum because isoenergetic lines are not parallel to pixel rows and the application of the shift to correct the slope smooths them. However they can be seen if integration is performed directly along CCD rows and columns (without shifting the COM positions). The origin of this phenomenon can be ascribed to a systematic error intrinsic in COM calculation. If we plot a histogram of all the calculated COM positions with respect to the central pixel of their spot (in the following we call it an *all-in-one* plot), we obtain the graph in Fig.(2.4a) The histogram is not flat as expected for uniform illumination, but it is peaked at the centre of the pixel dropping very quickly at the edges. This means that COM calculation tends to systematically shift the hit positions towards the centre of the pixel. This is due to the fact that we use a finite pixel matrix (generally 3×3 or 5×5) to calculate the COM coordinates. If the spot intensity distribution extends outside this matrix, the outer tails of it are neglected. These contributions, although very small, are essential to evaluate the COM correctly, because their weight contributes to move the COM outwardly. On the contrary, if we neglect them, the COM is systematically shifted towards the centre of the pixel where the photon hit, giving rise to a reconstruction error. If this happens for each random spot on the image, this mechanism explains the oscillation of the integrated intensity in Fig.(2.4b). If we try to repeat the all-in-one plot with a pixel period and sum all the replicas together we are able to reproduce almost perfectly the oscillation pattern Fig.(2.4c), meaning that it is intrinsically caused by the systematic error on COM localization. Our explanation of the origin of the reconstruction error implies that its entity is strongly connected with the choice of the spot dimension N as we show in next chapter with the help of numerical simulations. However, as the error appears to be systematic, it is possible to find a way of getting rid of it, by applying an empirical correction to the COM coordinates, as the η algorithm does.

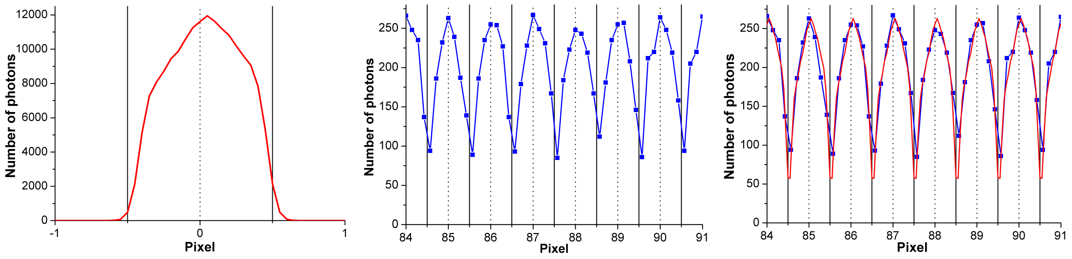

(a) (b) (c)

Figure 2.4: (a) Histogram of the COM distribution with respect to the central pixel of the spot, so-called all-in-one plot. (b) Reconstructed intensity of a flat-field illumination, integrated with a zero slope. Oscillations with one pixel period, introduced by COM calculation, are clearly visible. (c) Intensity oscillations (blue line) are well reproduced by summing replicas of the all-in-one plot at one pixel distance (red line). Data comes from a set of real measures made on our setup at Politecnico (see Chapter 3 for description) using the CCD in slow reading mode (100 kHz) and 3×3 pixel matrices for calculating the spot COM with the SPC algorithm.

2.3 η and β algorithm

The η algorithm is a non-linear charge interpolation method devised to optimize the detector resolution without systematic errors suffered by COM calculation. To understand how this algorithm actually works we start our analysis by considering a 1D strip detector, on which the η algorithm was first developed and tested [20, 61]; later we will extend this method to 2D sensors [53].

A strip detector is a 1D position sensitive detector where the basic sensing unit is a microstrip rather than a pixel. We are not entering in details of this kind of detectors, but an example of it on which η algorithm was successfully employed is called GOTTHARD [48]. If we consider strips with a small pitch p, charge splitting occurs exactly as in CCDs. Assuming that most of the charge is shared by a *cluster* of only two adjacent strips we can define the variable η as:

$$\eta = \frac{Q_R}{Q_L + Q_R} \tag{2.6}$$

where Q_L (Q_R) is the charge accumulated in the left (right) strip of the cluster. If we compare (2.6) with (2.4) it is clear that η is exactly the position of the centre of mass with respect to the centre x_L of the first strip. Hence the photon hit position would be given by the linear correction:

$$x_P = x_L + \eta p \tag{2.7}$$

Unluckily this calculation systematically shifts x_P with respect to the true hit position X_P. This is due to the fact that η is not linear with X_p because of capacitive coupling between adjacent strips and the specific charge distribution profile; moreover, another reason for non-linearity, which is relevant in our applications, is the fact that the charge cloud is usually bigger than the cluster and the intensity tails are lost outside it, being neglected in the calculation. If the charge cloud were square instead of gaussian-shaped, and smaller than the strip pitch, the linear correction in (2.7) would be exact, in ideal experimental conditions. In the case of a gaussian charge distribution the error has two main reasons: the non-linear relation between the COM and the actual gaussian center, and the loss of charge outside the two strips, which is not used in the COM calculation. The latter error depends strongly on the relative strip and gaussian widths. To compensate the reconstruction error we should use a correction which is non-linear in η:

$$x_P = x_L + f(\eta)p \tag{2.8}$$

where $f(\eta)$ is a strictly increasing function of η and $f(0) = 0$, $f(1) = 1$. If we consider a flat-field illumination of the detector we can calculate the value of η for many photon events and generate a distribution $dN/d\eta$ similar to the blue line in Fig.(2.5)[1]. The actual shape of the distribution depends on the intrinsic characteristics of the detector, in particular on the diffusive process inside the pixels and on the capacitive coupling among them. The correction factor $f(\eta)$ is given by the cumulative distribution of $dN/d\eta$ divided by the total number of events considered to generate the it:

$$f(\eta) = \frac{\int_0^\eta \frac{dN}{d\eta'} d\eta'}{\int_0^1 \frac{dN}{d\eta'} d\eta'} \tag{2.9}$$

In other words the idea behind the η algorithm consists in mapping the value of the centre of mass η for each possible hit position x_P and then inverting this relation to get $x_P(\eta)$. However this is not a true bijection as the mechanism of charge splitting is probabilistic, so we have to generate the histogram of η in a condition of mean illumination and pass through $f(\eta)$ to get the right correction shift. This implies that the η algorithm cannot make a strictly exact correction, as it is based on a statistical evaluation of it, not on the direct knowledge of the error of each event. Nevertheless we will show below that it works very well in practical terms.

---

[1] This curve is generated by computer simulations and consider a 2D pixel sensor, not a 1D strip detector (see below).

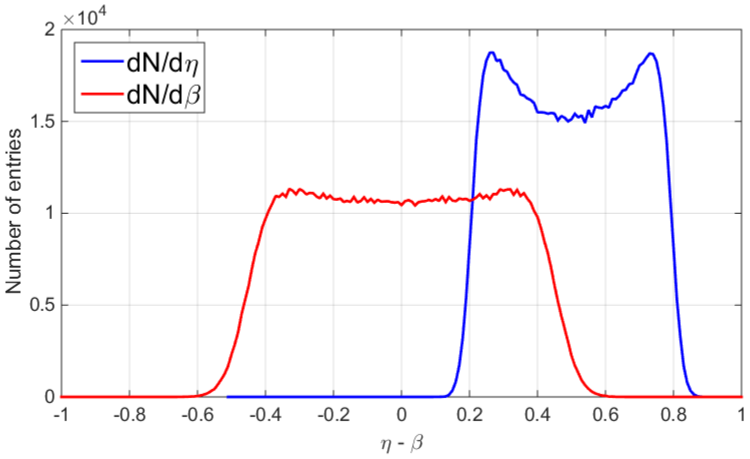

Figure 2.5: Example of η (blue line) and β (red line) distributions. They were generated by simulating 5×10^5 photons on a CCD with $20\,\mu$m pixels and 3.5 electrons of *rms* readout noise. See Chapter 3 for more details on the simulations.

This method can be easily extended to 2D sensors by considering clusters of 2×2 pixel and separating the calculation along the x and y direction. We can then define two η parameters:

$$\begin{aligned} \eta_x &= \frac{\sum_j \left(\sum_i Q_{ij}\right) x_j}{\sum_{ij} Q_{ij}} \\ \eta_y &= \frac{\sum_i \left(\sum_j Q_{ij}\right) y_i}{\sum_{ij} Q_{ij}} \end{aligned} \tag{2.10}$$

where the origin $(x_j = 0, y_i = 0)$ for η calculation is the centre of the top left pixel of the cluster and the pixel coordinates x_j,y_i can assume only the integer values 0 and 1 as we are working on 2×2 pixel clusters. Starting from this position the photon impact subpixel coordinates (x_P, y_P) are evaluated by adding the corrections $f(\eta_x)$ and $f(\eta_y)$ given by Eqn.(2.9). An example of a typical distribution $dN/d\eta$ is plotted in Fig.(2.5) (blue line). The curve shape is analysed in more details in Chapter 3. Our algorithm for spot search does not work directly with 2×2 clusters, but at least with a 3×3 matrix. Once a spot has been identified the corresponding cluster is chosen as the most intense of the four 2×2 submatrices of a 3×3 matrix. The simplest version of the η algorithm works with clusters of 2 pixels in each direction because in the detectors on which it was first implemented charge splitting mainly involved only two neighbouring pixels. However, with a $13.5\,\mu$m detector and 930 eV photons, using a 2×2 cluster means neglecting a large part of the charges. So we tried to implement an extension of the η algorithm working with 3×3 matrices, which we called β algorithm just for our convenience. In this case β_x, β_y correspond exactly to the COM coordinates x_{COM}, y_{COM}, and the subpixel correction is referred to the central pixel of the spot. As Eqn.(2.9) returns a correction between 0 and 1, we redefined it as:

$$f(\beta) = \frac{\int_{-\frac{1}{2}}^{\beta} \frac{dN}{d\beta'} d\beta'}{\int_{-\frac{1}{2}}^{+\frac{1}{2}} \frac{dN}{d\beta'} d\beta'} - \frac{1}{2} \tag{2.11}$$

to allow a correction in the interval $[-\frac{1}{2}, +\frac{1}{2}]$, so that we are able to locate each event everywhere inside the central pixel of the spot. An example of distribution $dN/d\beta$ is represented in Fig.(2.5) (red line). Both η and β are able to evaluate the photon hit positions applying a statistical correction which is not linear in η (or β). The SPC algorithm instead uses a linear correction represented by the COM position, which is simply summed to the central pixel coordinate to obtain the photon impact position, in a similar way as displayed by Eqn.(2.7). η and β can compensate non-linearities, which the linear COM correction converts into artefacts in the reconstructed image. However the performances of the three algorithms strongly depend on the experimental conditions and in particular on the relative size of the pixel and of the charge cloud, as it will become clear in the following chapter.

Chapter 3

Experimental results

The current chapter is devoted to the experimental assessment of the algorithms described in the previous one. The main attention is put on the resolution enhancement that is possible to obtain by moving from the traditional algorithm to single photon techniques involving the reconstruction of the hit positions. The data shown are results from both numerical simulations and experimental measurements carried out in the labs of Physics Department at Politecnico di Milano. Not every aspect of the algorithms described in Chapter 2 was analysed in detail, but rather we focused on results which are innovative with respect to the work done by previous students [1, 46]. In particular we studied the resolution comparison of traditional and SPC algorithm operating the CCD in the high speed reading mode. A key step in the procedure was the correct offset subtraction that required an in-depth analysis of the background shape. The last section presents the preliminary results on the application of the η and β algorithm for correcting the systematic error generated by COM calculation.

3.1 Experimental setup

Fig. (3.1) shows the experimental setup installed at Politecnico di Milano in order to carry out the CCD resolution tests with the different algorithms. The photon source is a conventional X-ray lamp with a copper anode generating a non-monochromatic spectrum with a dominant peak around 930 eV which corresponds to the Cu $L_{\alpha,\beta}$ emission lines. The beam has a spot size around 2 mm and a high divergence and it is collimated horizontally by two slits with 40 μm

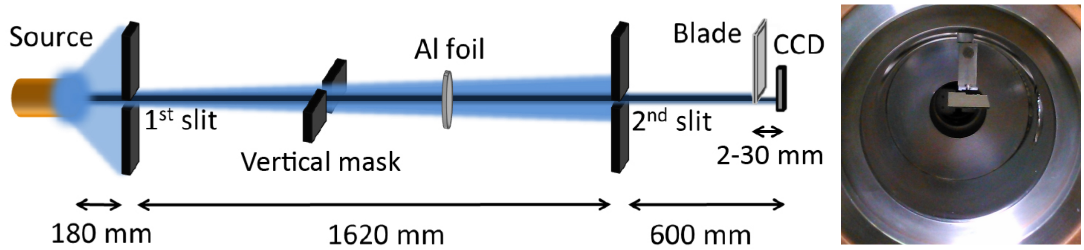

(a)

(b)

Figure 3.1: Experimental setup, top view taken from [2] (a) and detail of the razor blade (b).

aperture, whereas vertical divergence and beam size are only slightly reduced by using an intermediate mask. A thin Al foil stops the low energy visible photons emitted by the X-ray tube filament that, being detected by the CCD, would dominate the signal over the X-ray photons. These are partly stopped by a vertical razor blade placed in front of the detector and resolution is estimated by the sharpness of the transition between the illuminated and the shadowed region of the sensor. The blade is mounted on a micrometric xyz manipulator that allows to adjust its position with respect to the beam and its distance from the detector surface. The latter parameter has been optimized to avoid loss in resolution due to diffraction effects; it was shown by simulations that the optimal value was below 2 mm, with a corresponding diffraction broadening smaller than $2\,\mu$m. The setup was designed this way because at first we were interested in evaluating the resolution along one direction only, whereas the intensity was integrated on the perpendicular one, resembling the same procedure for generating a RIXS spectrum. For this reason we took care of collimating the beam mainly in the direction along which we wanted to measure the resolution. All the setup is kept in high vacuum around 10^{-8} mbar.

In our system we do not have a diffraction grating that separates the energies of incident photons, so we could not characterize precisely the spectrum emitted by the X-ray lamp. However we can get a good insight of it by plotting the spot intensity histogram, which is also useful for checking the amount of multiple events and whether spot reconstruction is correct. Fig.(3.2) shows the spot intensity histogram generated at three different levels of emission current of the lamp (which gives a proportional photon flux). The main peak is centred about 290 electrons, which is not far from the expected spot energy of the Cu emission lines (260 electrons); the discrepancy could be due to a small error in the exper-

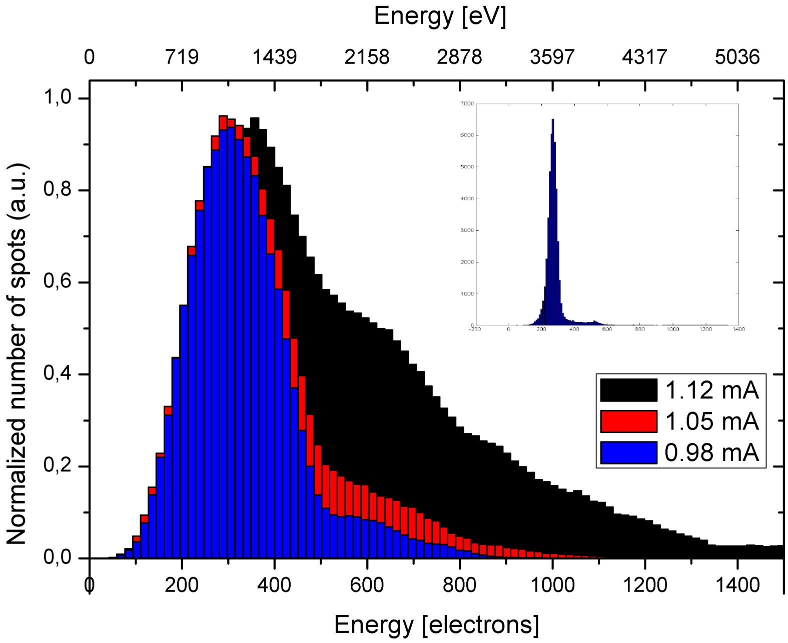

Figure 3.2: Spot intensity histograms for three increasing levels of emission current of the lamp. It is interesting to notice how the bump of double events increases up to completely modifying the shape of the spectrum. In the inset, an equivalent spectral measurement done at ESRF, taken from [1].

imental determination of the electron/ADU gain. A second small peak emerges at twice the energy of the main one, representing the double events present in the image and if we increase the photon flux, the right shoulder of the main peak increases more and more. This is due to double and triple events and to spots which are not correctly reconstructed because in the same spot area a superposition of the lateral charges of different photons occurs, leading to events with a fractional number of photons. For comparison the inset shows the analogous histogram obtained with synchrotron light at ESRF [1]; The main peak is thinner and better defined, centred at 260 electrons, but it is still possible to notice the double event peak on the right. This kind of plot was very useful to set the thresholds for the spot recognition in the algorithm, in order to select only the main peak and leaving out most of the double events.

3.2 Background analysis

The SPC algorithm has already been tested in depth by our group in the slow reading mode of the detector (100 kHz), obtaining a strong resolution enhancement from 30 μm to $\approx$ 7 μm [1, 2].Hence we would like to demonstrate that a

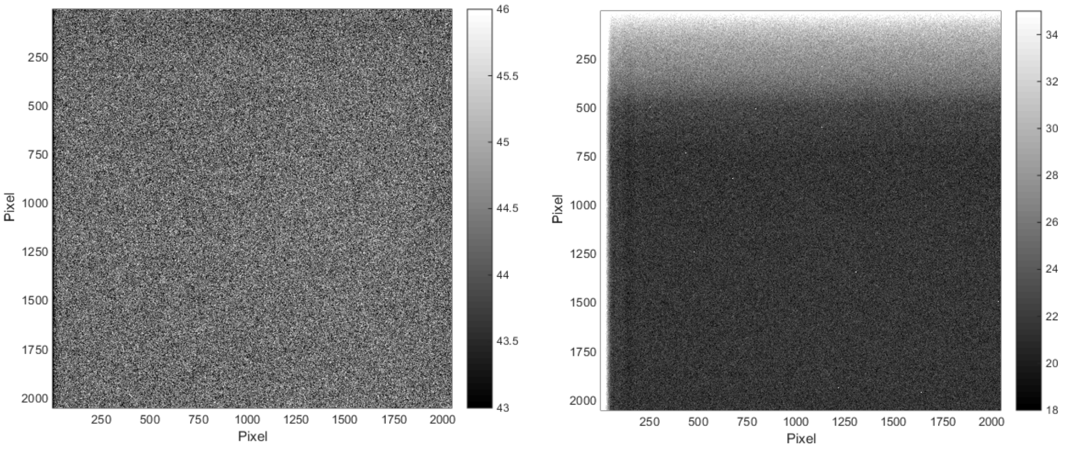

(a) (b)

Figure 3.3: Comparison of the background for fast (a) and slow reading (b). The images are the result of 10 exposure of 30 s. Intensity is expressed in ADU and divided by 10 to get the mean value for a single exposure.

comparable increase in resolution is also possible in fast reading mode (1 MHz). The latter is very important for applications because it lowers by ten times the reading time of the CCD with a corresponding improvement of the duty cycle. If we consider the whole CCD area (2048×2048 pixels) the reading time is ≈ 41 s for slow reading and ≈ 4 s for fast reading. We expected a sizeable deterioration of resolution due to higher readout noise, but the main issue in processing fast reading images with respect to slow reading ones was connected with the background subtraction. Fig.(3.3) shows a comparison of the background map in slow and fast reading mode. Each image is the accumulation of ten exposures of 30 s each; intensity is expressed in ADU and rescaled by a factor 10 to get the mean intensity for a single exposure. The mean value of the offset differs notably in the two modes, but this does not represent a problem as long as the background is flat. This is the case for the slow reading mode (Panel (a)) where the background is almost constant around 44 ADU on all the chip, but on the other hand the fast reading mode (Panel (b)) reveals some peculiar features, the most evident of them being a long-range decreasing slope in the y-direction. The other characteristic features are visible on the left side of the detector and consist in a region of almost saturated pixels followed by an intensity oscillation along the x-direction. We can better identify the regions of the detector involved in these phenomena by integrating portions of the image along pixel rows and columns as depicted in Fig.(3.4). Integration along x (Panel (a)) highlights the decreasing pattern of the background; the total drop is far from being linear and three

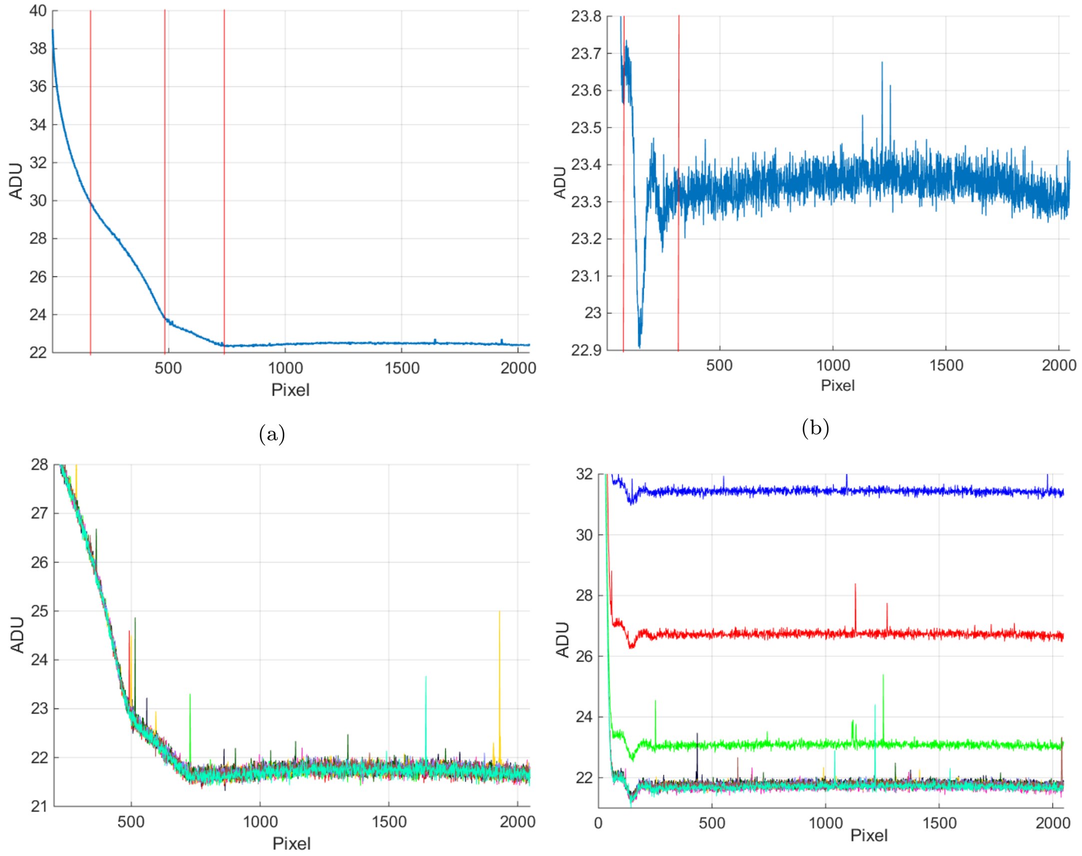

(a) (b)

(c) (d)

Figure 3.4: Background characterisation by integrating different chip regions: full chip integrated along x (a); full chip integrated along y (b); vertical stripes integrated along x (c); horizontal stripes integrated along y (d).

distinct regions with different slopes can be visually identified, as pointed out by the red vertical lines. Finally the pattern flattens out after about 740 pixel rows. The intensity of this long fall ranges from 39 to 22 ADU which means an interval of 42 electrons. Along x (Panel (b)) the situation is different; the saturated region takes 65 pixel columns, after which there is a damped intensity oscillation which dies out around pixel 300. Finally there is a flat region with a maximum intensity variation of a fraction of electron. An integration over the whole CCD surface, although useful, might be too crude, so we divided it into 10 vertical and horizontal stripes of the same width (204 pixels). Panel (d) shows the integration along y of the horizontal stripes; the different profiles are vertically shifted because of the decreasing slope along y and superimpose in the flat region. The important evidence is that, although shifted, they preserve the same shape suggesting background uniformity along the pixel rows. In Panel (c) the vertical stripes have been integrated along x and are very well overlapping, confirming uniformity along the rows. The first stripe along the left edge of the detector is not shown as it also includes the saturated region.

After identifying the main features of the background we wanted to understand if they are connected to the physical borders of the detector or to the *region of interest* (ROI) that is measured. To do this we took several exposures with different ROIs and carried out an analysis similar to the one for the whole chip. What emerged is that the decreasing surface is strictly linked to the ROI and not to the physical positions of the pixels. This means that if we define a ROI in the flat region of the background of Fig.(3.3) we do not get a flat image, but an inclined profile, whose slope is also dependent on the ROI size; we then suggest that this feature may be connected with the charge transfer mechanism. As explained in Chapter 1 the image is acquired by consecutively shifting each rows of charge towards one end of the detector. When readout frequency is too high we suppose that charge transfer is not correct and some electrons are left behind leading to charge accumulation. This would explain why this slope occurs only in one direction and involves all the length of the chip. The intensity oscillation is instead tied to the left side of the ROI, no matter where this is chosen on the physical detecting area. Moreover its period and amplitude is constant not depending on the ROI extension. We do not have any explanation for this phenomenon but it should be still correlated to an imbalance of charge transfer in the fast reading mode, as it is not present in the slow one. The only feature related to the physical edge of the sensor is the saturated region on the left side, which is not present if we exclude the first columns from our ROI; however, if we also consider the detector edge in the ROI, the number of columns involved, in which saturation occurs, depends on the width of the ROI.

In slow reading mode the background that has to be subtracted is calculated for every single exposure by taking the average intensity in a dark area (a region not exposed to X-rays) of the image. This ensures that the removal is correct also if shifts in the background level have occurred between exposures. The method works correctly only if the background is reasonably flat, which means that if we wanted to apply it also in the fast reading mode we would have to be able to position the interesting signal in the flat region. If we consider Fig.(3.5) we understand that the larger the ROI is, the wider the flat region extends,

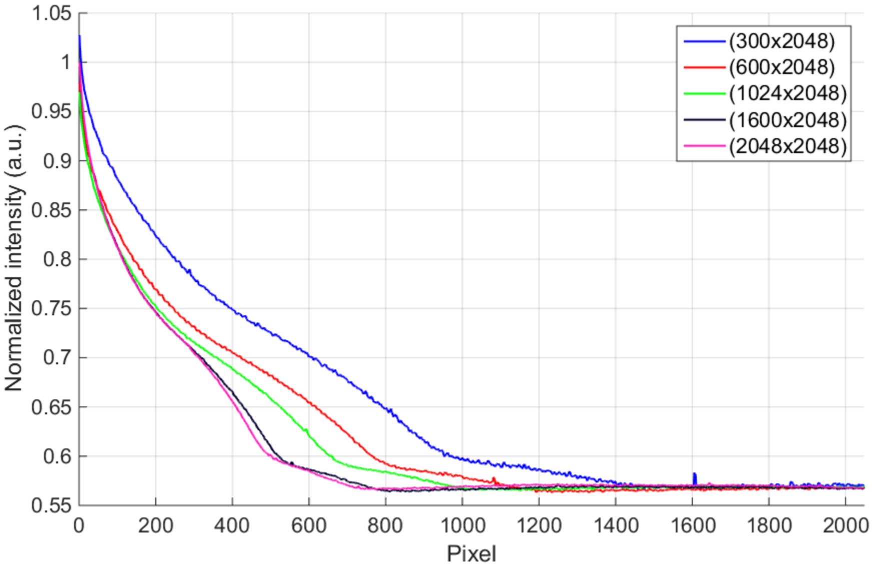

Figure 3.5: x-integrated profiles for different ROI sizes. The first 100 columns of the sensor were not considered in order to neglect the saturated region. Curves were slightly smoothed and rescaled to match the flat areas.

because the different lines represent x-integrated backgrounds for ROIs with different number of pixel columns. This means that, to be sure the algorithm is working correctly, it is preferable to work with the whole sensor, but most of the pixels that have to be read are useless. This approach is undesirable because it deteriorates the duty cycle and occupies a lot of memory making processing tasks on group of several images troublesome. As the background of fast reading acquisition is not homogeneous all over the sensor, the best way to subtract it is to take a dark image for background evaluation before each illuminated one. This approach is however not practical on our setup because every time the lamp is shut with a slit and opened again, photon flux takes a long time to stabilize. Hence we decided to measure the background only every set of 90 exposures, assuming that it was not evolving too much during the time lapse of the measurement (if we consider 40 s exposures each set takes around one hour to be acquired). The general procedure we implemented to subtract the background is outlined by the block diagram of Fig.(3.6). We are making the initial assumption that the total background is constituted by a non-uniform component, which is though stable in time, and a fluctuating offset, which is almost constant on the entire chip. We start by acquiring a set of dark images (top, left in figure) to average in order to improve statistical accuracy. We were generally using 20 images for our measurements. We cannot take their average

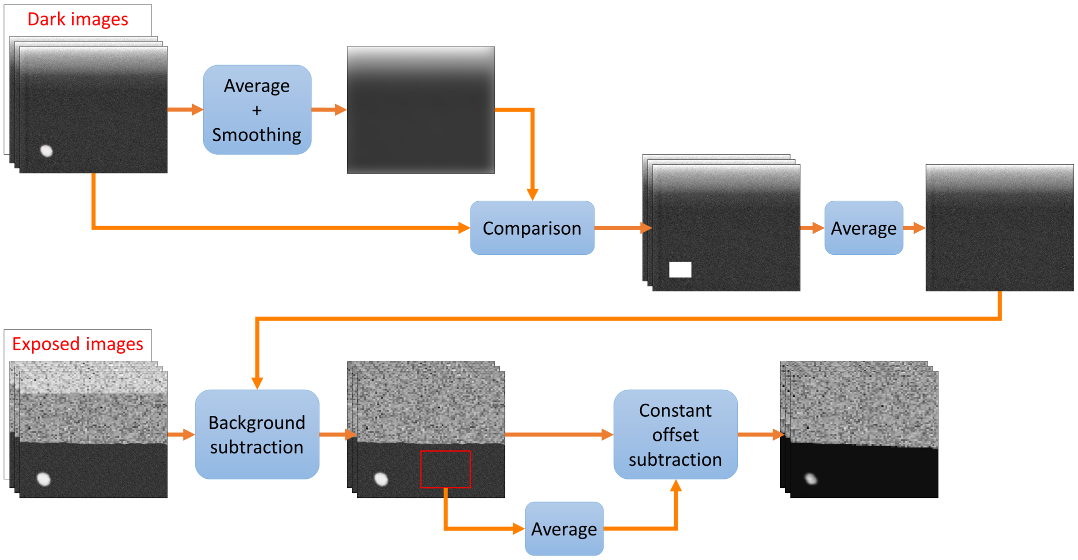

Figure 3.6: Block diagram sketching the background removal procedure for images taken in fast reading mode.

directly because of the possible presence of cosmic rays (the white spot in the bottom left corner of the pictures, intentionally exaggerated in size) that, having a high number of counts, would alter locally the background shape. To get rid of them we generate a trial background given by a strongly smoothed average of the dark images (strong smoothing is enough to flatten the cosmic ray peaks). We then compare each dark image with the trial background and pixels differing from it by too many counts, hinting at the presence of a cosmic ray, are set to NAN (*Not a number*) values. NAN values are not considered in generating the final average which represents our estimate of the background. This constitutes the irregular pattern that is supposed stable over time and it is subtracted from each exposed image (bottom left). However between consecutive images small fluctuations or jumps in the A/D converter can occur. These are treated as a constant offset stacking on the irregular background and are estimated for every single image by taking the pixel average on a dark region. The calculated value is subtracted from the corresponding image, concluding the background removal process.

For a packet of 20 background images (the typical dimension we used in the measurements) the pixel intensity standard deviation, averaged over the image is 3.37 ADU that is 8.4 electrons, which is compatible with the expected readout noise; this is also in agreement with the intensity standard deviation averaged on a dark region of a packet of 90 illuminated images.This value is not modified after background subtraction meaning that offset removal is correct and is not introducing additional noise contributions.

3.3 Resolution estimates

In this section we describe the main results obtained in enhancing the resolution with the SPC algorithm (COM calculation) with respect to the traditional one. We started by repeating the measurements with slow reading mode to reproduce and confirm the previous results by Andrea Amorese [1, 2]. During measurement we operated the X-ray lamp at 3 kV, keeping the current in the filament around 2.9 A with a typical emission current between 0.1 and 0.4 mA, depending on the stability of the lamp. This value was constantly adjusted in order to keep the photon flux enough low, avoiding too many overlapping spots. The photon density on the image was monitored approximately by eye inspection. The software thresholds for spot recognition were chosen in order to keep photons of the desired energy range and avoid double events. We used LCPT = 60 electrons and HCPT = 210 electrons. The latter value was kept on purpose lower than the expected total spot intensity (260 electrons) to reject single events. The thresholds on the total spot intensity are LSIT = 120 electrons and HSIT = 420 electrons and were chosen according to the spot intensity histogram (Fig.(3.2)) as a trade-off between the total number of spots and the number of double events. The number of subpixels was fixed at 7 meaning that each channel of the final spectrum is 1.93 μm. The COM calculation was carried out on a 5×5 matrix because it had proved to be the best solution for 13.5 μm pixels in the slow reading mode (3.4 electrons *rms* noise) as it did not neglect the tails of the charge distribution. We did not consider the whole detector but acquired a ROI of 585×600 pixels in order to select a region where illumination was almost uniform; moreover this also helped saving computational resources. Fig.(3.7) shows the result of the acquisition of 12 groups of 90 images exposed for 40 s each, for a total of 1080 images. The total spectrum was generated by summing the profiles of every group of images after manual alignment. The traditional profile was rescaled and horizontally shifted to ease the comparison with the SPC profile. We defined the system resolution as the width of the transition from the dark to the illuminated region on the image. The cut was fitted with an *erfc* (complementary error func-

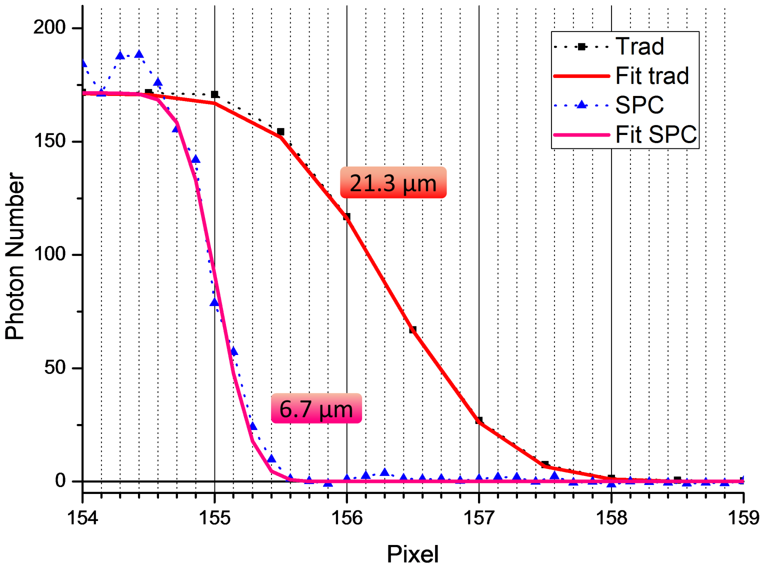

Figure 3.7: Experimental results of resolution tests using slow reading mode, with 5×5 spots.

tion), and the resolution was taken as the FWHM of the gaussian generating it. For the traditional algorithm we obtained a resolution of 21.3 μm (1.6 pixels). This value is the same order of magnitude of the cloud size, as we expected. With SPC we managed to enhance resolution up to 6.7 μm (0.5 pixels), proving that subpixel resolution is achievable. Our results are in good agreement with those in [2].

Afterwards we repeated the same procedure on images acquired in fast reading mode. We kept the same experimental conditions and used also the same software parameters except for incrementing the LCPT to 70 electrons. In this case we studied the different performance of the spot matrix size, by analysing the same dataset with a 3×3 or a 5×5 matrix. Indeed the 5×5 spot matrix does not neglect the tails of the charge cloud with respect to the 3×3, but the additional ring of pixels it considers for COM calculation has a low signal to noise ratio. We considered 11 sets of 90 images with 40 s exposure, for a total of 990 images. Every group was interchanged with a set of 20 background acquisitions. Results are shown in Fig.(3.8). The traditional line has been normalized to the SPC profile. A slight rescaling was also necessary between the two SPC curves because spot selection marginally depends on the matrix size chosen. The traditional profile is of course the same because it does not involve photon counting. We demonstrated that also in fast reading mode SPC is capable of strongly enhancing the spectral resolution. Without centroiding, resolution is 30.3 μm (2.2 pixels),

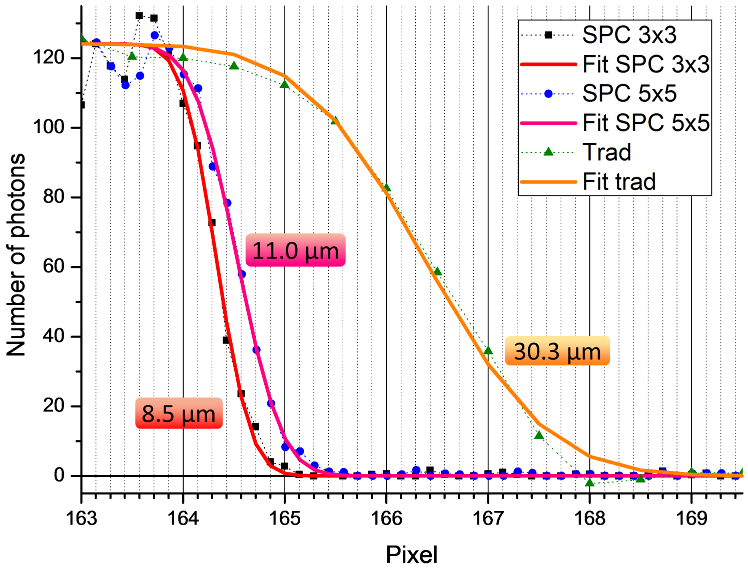

Figure 3.8: Resolution test in fast reading mode. Comparison of the results for 3×3 and 5×5 spot matrices.

but, with SPC, it reduces to 11 μm (0.8 pixel) for 5×5 spots, or 8.5 μm (0.6 pixel) with 3×3 spots. Subpixel resolution is then still achievable. As expected, performances in fast reading mode are worse than in slow reading, because of higher readout noise (10.2 electrons *rms*) and background alteration. While a 5×5 spot matrix is the best choice for slow reading, a 3×3 matrix guarantees a better resolution with fast reading. With low noise a 5×5 matrix is preferable because it completely contains the photon charge cloud, whereas a 3×3 matrix does not, when using a CCD with 13.5 μm pixels. However in fast reading mode the tails of the intensity distribution are completely exceeded by the noise and hence a 3×3 matrix gives better results.

3.4 Mean spot shape and all-in-one plots

The mean spot shape is important to understand if SPC is working well and can give interesting information on charge cloud diffusion to be compared with literature. To get the spot shape we cannot simply average all the spot matrices identified in an image, because of pixel discretisation; doing like this we get the stepped surface in Fig.(3.9a). Instead we have to take into account the COM position inside the central pixel of the spot. This is accomplished by defining a subpixel grid and shifting each spot in order to bring its COM in the centre of

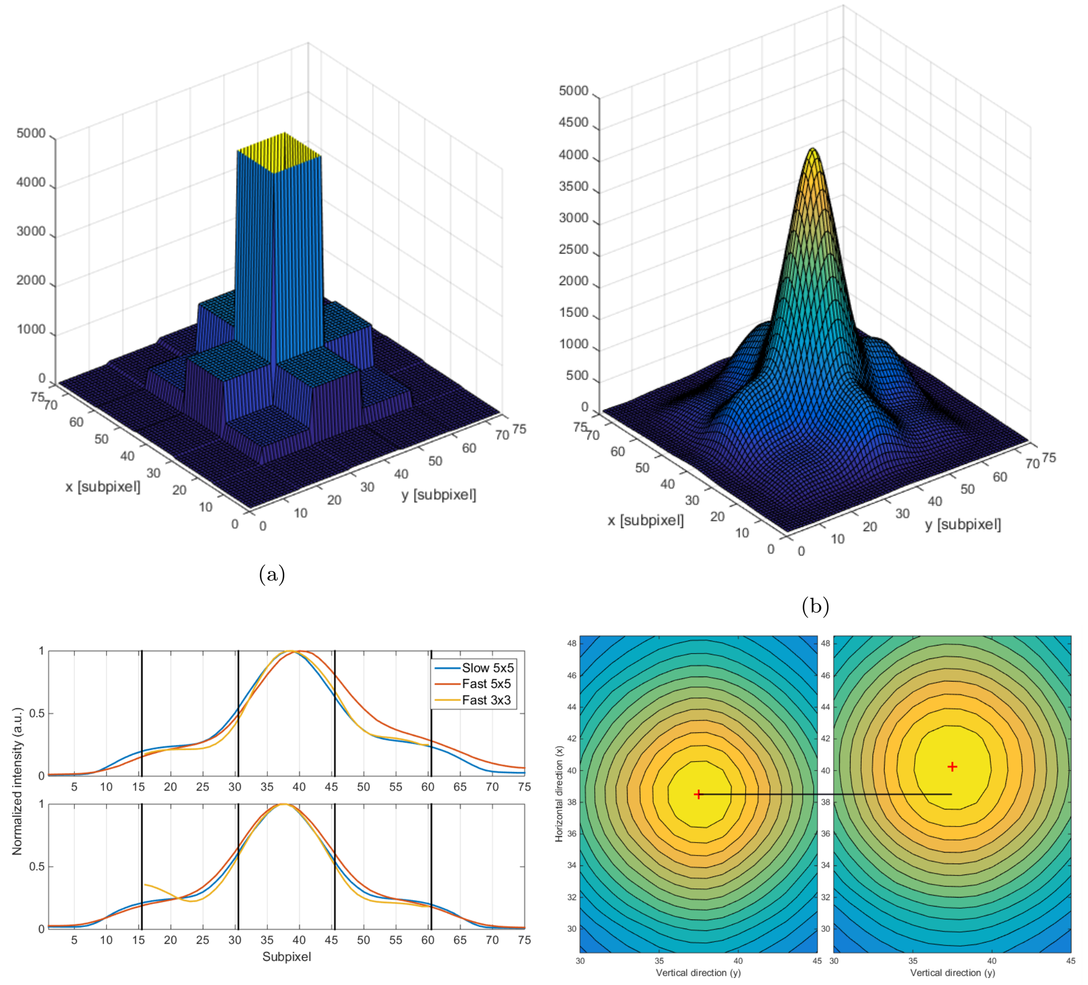

(a)

(b)

(c)

(d)

Figure 3.9: Mean spot shape analysis: (a) stepped mean spot shape generated without COM subpixel shifts. (b) Smoothed mean spot shape after COM supbixel shifts. (c) Horizontal (top) and vertical (bottom) cuts of the mean spot shape. (d) Contour plots of the mean spot shape for slow (left) and fast reading (right) using 5×5 spots, exhibiting the spot deformation in the y direction (axes are rotated by 90°).

the spot matrix. This allowed us to generate the mean spot shape in Fig.(3.9b) which resembles a 2D gaussian. Nevertheless we were not able to remove the effect of discretisation totally, which is still visible in the four lateral shoulders surrounding the main peak. Anyway we tried to fit the curve with a 2D gaussian getting a FWHM of 20-25 μm, which is compatible with [21].

It is interesting to compare the mean spot shape for different acquisition modes and matrix sizes. Apparently the situation is pretty similar resulting in almost the same FWHM. However some differences are highlighted by cutting the mean spot in the matrix centre, along x (horizontal direction) and y (vertical

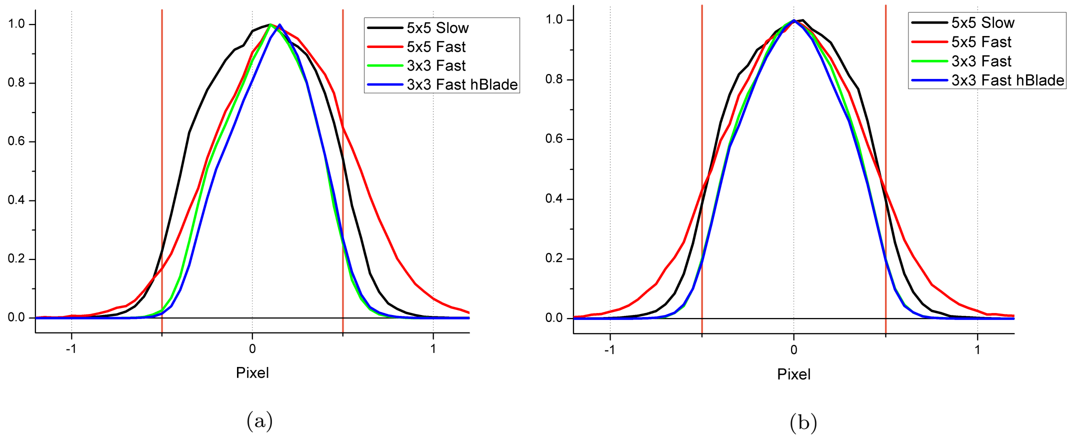

(a)

(b)

Figure 3.10: All-in-one plots along x (a) and y (b) for different reading modes and spot matrix sizes. The blue curve refers to measurements after a 90° rotation of the blade (now oriented horizontally).

direction). As depicted in Fig.(3.9c, bottom), the mean spot shape is symmetric along y despite a small width variation due to the combination of noise and matrix size. A 5×5 spot with fast reading collects a lot of noise on the outer pixels, where the signal is small, resulting in a broadening of the mean reconstructed spot. On the other hand a 3×3 matrix neglects the lateral tails of the charge cloud and COMs are shifted more strongly to the pixel centre. Along x, as shown in Fig.(3.9c, top), the mean spot shape is no longer symmetric, but it is deformed to the right. This behaviour, although slightly present in slow reading mode, increases with fast reading, even leading to a subpixel peak shift with a 5×5 matrix. This deviation is difficult to visualize directly on the 3D surface of the mean spot, but it is evident from a contour plot (Fig.(3.9d)). Spot deformation happens perpendicularly to the direction along which background increases, hence we believe that this phenomenon is also due to imperfect charge transfer during fast reading, but it is not compensated by background removal.

The very same behaviour is also highlighted by the all-in-one plots, which represent the histogram of COM x and y positions relative to the central pixel of the spot. Fig.(3.10) shows the all-in-one plots for different combinations of reading modes and spot matrix sizes. With uniform illumination we expected the plots to be flat as photons hit each region of the pixel with the same probability. However COM calculation, as anticipated in Chapter 1, introduces a systematic error by accumulating COMs towards the pixel centre and depleting the edges, giving the black line in Panel (b) in case of a 5×5 matrix with slow reading. If we keep the same spot size for fast reading the curve sharpens and long tails develop outside the central pixel. In ideal conditions, with no noise, COM calculation should always return values between +0.5 and -0.5 pixel, hence located in the central pixel of the spot, but adding noise also allows values to extend outside pixel edges. As the noise level is raised, uncertainty on COM location increases as well, generating longer tails of events outside the central pixel. There is a critical noise level at which it is possible to get a COM position even outside the spot from which it arises, strongly affecting resolution. This problem can be dealt with by neglecting the events giving COM outside the spot, as they are too much disturbed by noise. Fast reading with 3×3 spots (green line) gives a more peaked distribution, because neglecting the outer pixels of the spot results in a bigger shift towards the centre. If we consider what happens along x (Panel (a)), the situation is similar to what we observed on the mean spot shape. In slow reading (black line) the COM distribution is slightly not symmetric, and this tendency exacerbates in fast reading. To understand if, as we supposed, this spot deformation was really linked to a physical direction on the sensor and not to the way we processed the data, and to check whether it was worsening the resolution, we wanted to repeat the same measurements along the opposite direction of the CCD. As the beam collimation was optimized for the horizontal direction in our setup, we should have rotated the CCD camera by 90° to maintain the same beam properties for the new measurements. This was however impossible because of the liquid nitrogen tank assembled with the sensor, that had to remain vertical. Hence the only feasible solution was to rotate the razor blade by 90° instead, which was then horizontal, recalling that the resolution is evaluated along the direction perpendicular to its edge. The measures in the new configuration demonstrated that spot deformation was linked to the physical sensor and not to the direction along which resolution was estimated. Thus the problem is not a software fault, but a true charge drift, probably during readout. The all-in-one plots with the horizontal blade, using a 3×3 matrix, are reproduced in the graphs of Fig.(3.10) (blue lines) and coincide approximately with the corresponding curves measured with the vertical blade (green curve).

We were not too worried about the COM distribution deformation because it occurs along the x-direction of the sensor which corresponds to the direction of integration when the detector will be installed on ERIXS. However we believed that this shape modification could at least deteriorate the resolution we were

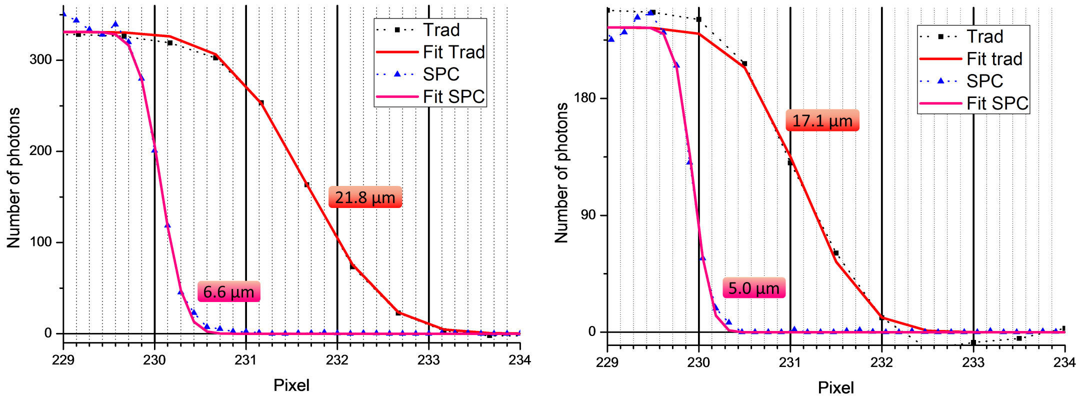

(a)

(b)

Figure 3.11: Experimental results of resolution test after rotating the blade by 90 °. Slow reading, 5×5 matrix (a) and fast reading, 3×3 matrix (b).

measuring with the vertical blade, hence its rotation by 90 ° might be also useful to test if we could get a resolution enhancement when the spot asymmetry is integrated out, as it will happen in the real setup. The results we obtained are summarized in Fig.(3.11). During measurement and data processing we used the same parameters as in the case of the vertical blade. The slow reading profile with 5×5 spot size (Panel (a)) was obtained from 15 groups of 90 images exposed for 40 s each, for a total of 1350 images. We found a resolution of 21.8 μm with the traditional algorithm and 6.6 μm with the SPC. Values comparable to the previous case with vertical blade are compatible with the fact that COM histogram is not significantly shifted in case of slow reading. More interesting, but not so straightforward to understand, is the result for fast reading, where we explored only the 3×3 case that is the best solution for higher noise. In this case we found an extremely small resolution value of 17.1 μm with traditional algorithm and 5.0 μm with SPC, with a big resolution enhancement with respect to the vertical blade tests. An improvement was expected, but the value we found is smaller than its counterpart obtained with slow reading, despite the lower noise, and even better than the value given by ideal single-photon simulations (see next section). Moreover in the case of the horizontal blade the beam should be more diverging, which should affect the resolution negatively. A measurement repetition would be required to confirm these values, that could arise from a particularly stable set of images, but anyhow we believe that the true experimental geometry at ERIXS represent the best solution with respect to the performance

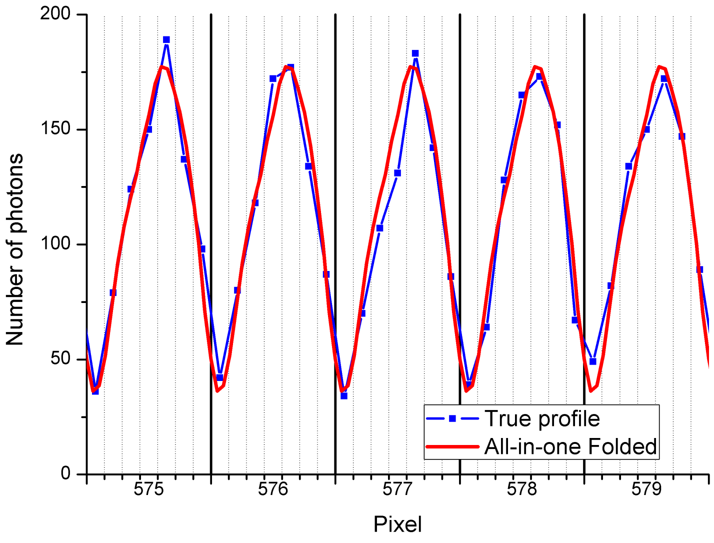

Figure 3.12: Intensity oscillations (blue line) in fast reading mode reproduced by replicating and folding the COM all-in-one plot (red line).

achievable with our detector.

Although not problematic for resolution, the systematic error of COM reconstruction results in a modulation of the final intensity profile in each pixel, that can finally reflect into troublesome oscillations of the spectrum. In the spectra we used to estimate resolution, oscillations were not present because they were smoothed out by integrating along an inclined line. In order to reveal oscillations we used the same set of images taken for resolution tests with fast reading, integrated them along horizontal lines (slope$\,=\,$0) and summed all the profiles without any shift. The intensity profile, blue line in Fig.(3.12), shows oscillations with a period of one pixel and the signal at the edges is around one quarter of the signal in the centre. As already anticipated in Chapter 2 (see Fig.(2.4)) intensity oscillations are clearly connected with COM systematic error, as we were able to reproduce them by summing copies of the all-in-one plot at one pixel distance (red line). The asymmetry in the all-in-one plot also appears in the intensity profile where the oscillation maxima are shifted by $\approx 1/7$ pixel (one subpixel) from the centre. If we consider a 5×5 matrix, both in slow and fast reading, the all-in-one plots show longer tails outside the central pixel (see Fig.(3.10)), which, when folded, partly compensate the depleted edges, resulting in an almost flat intensity. The presence of intensity oscillations with uniform illumination was one of the main reasons to start experimenting COM correction methods as the η and β algorithm.

3.5 Resolution estimates from simulations

Before devoting ourselves to the study of algorithms for COM correction, we wanted to explore through computer simulations the performance of SPC algorithm in a wider range of working conditions, as different readout noise, pixel size and photon energy. The simulations were carried out on a 100×850 pixel image with monochromatic photons generating a gaussian-shaped charge cloud of 25 μm FWHM. The intensity (number of electrons) of each photon was given by the nominal intensity $N_{el} = E_{photon}/3.6$ plus a gaussian Fano noise contribution, using Fano factor for silicon $F = 0.115$. Each simulation consisted in 3×10^6 photon hits, and readout noise was modelled as gaussian with zero mean and standard deviation specified by its *rms* value expressed in electrons per pixel. As we had enough intensity on the image, we used a grid with 20 subpixels for spectrum integration. It is important to stress the fact that the simulations we carried out were approximate as they did not take into account some real experimental aspects. In particular we did not consider the presence of a background and we supposed truly monodispersed photons. Moreover, to speed up computation, we shot photons one-by-one on the image calculating their COM separately, so we were completely excluding double events. Fig.(3.13) shows as an example the profiles generated for a sensor with 13.5 μm pixel, using a 3×3 spot matrix, for different noise levels. As the readout noise increases the transition broad-

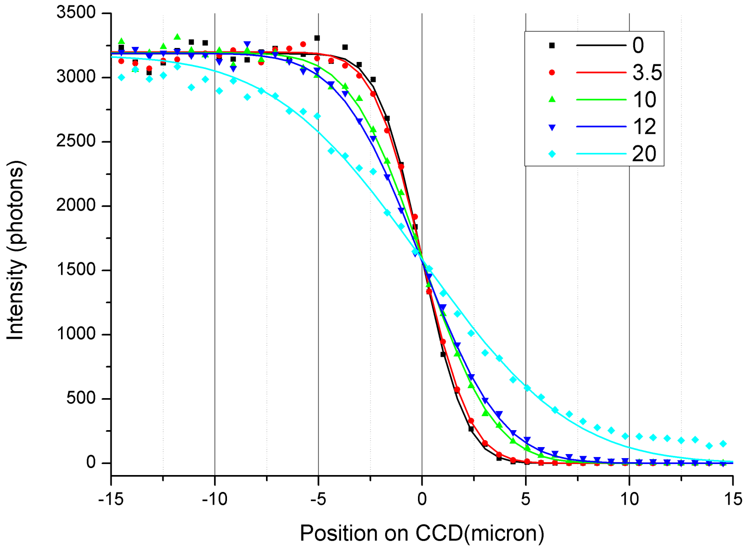

Figure 3.13: Simulation results show how the width of the transition (resolution) broadens by increasing the readout noise.

ens lowering resolution. The datapoints for 20 electrons *rms* noise (cyan curve) show long tails moving away from the *erfc* fitting line. These are due to the already mentioned problem that calculated COMs can be shifted far from their spot centre by noise, but its occurrence can be prevented by neglecting the spots which are too deformed. We were mainly interested in inspecting SPC performance with 13.5 μm and 20 μm pixels, as they are the pixel sizes of detectors we have at Politecnico di Milano, so for these cases we tested many values of readout noise. Moreover we also changed photon energy to 450 eV and to 3000 eV to see whether SPC was applicable to other energy ranges, and which was the approximate resolution that could be achieved. Finally we analysed a few cases with 30 μm and 48 μm pixel size, as they were alternative detector solutions that were being developed in other laboratories. The main results we obtained from simulations are summarized in Tab.(3.1) and Fig.(3.14). The resolution values are again calculated as the FWHM of the transition from the dark to the exposed region of the image and are expressed in μm.

Photon energy	**Pixel size**	**Spot size**	**Noise level**									
			0	2	3.5	4	6	7	8	10	12	20
930 eV	13.5	3x3	4.0	4.0	4.3	4.5	4.9		5.6	6.4	7.2	13.3
	20	3x3	2.4	2.6	2.8	3.1	3.7		4.7	5.5	6.6	11.2
	13.5	5x5	1.8	2.7	3.7	4	5.8		7.8	9.8		
	20	5x5	1.9	3.3	5.0	5.7	8.2		11.1	13.8		
450 eV	13.5	3x3	4.9		6.0			8.7		14.0		
	20	3x3	3.1		4.6			8.0		11.3		
	13.5	5x5	2.6		7.1			14.7		25.2		
	20	5x5	2.5		10.2			20.4		29.6		
3000 eV	13.5	3x3	3.5		3.5			3.5		3.8		
	20	3x3	1.8		1.9			2.0		2.1		
	13.5	5x5	1.0		1.5			2.2		3.0		
	20	5x5	1.3		1.9			3.1		4.3		
930 eV	30	3x3	2.7		3.5					7.6		
	48	3x3	11.1		12.4					15.6		

Table 3.1: Synthesis of all the resolution values obtained from computer simulations.

Concerning the 13.5 μm and 20 μm detectors in Fig.(3.14a), the plot demonstrates that with a 5×5 spot size a detector with 13.5 μm pixels always gives better results, whereas a 20 μm pixel has to be preferred if we choose a 3×3 spot. The 3×3 lines are also less inclined with respect to the 5×5 ones, meaning that they are less sensitive to the readout noise. This is explained by the fact that a smaller matrix takes into account only the pixels with higher SNR, and gives an almost slowly-increasing resolution unless the noise becomes comparable with the photon-generated intensity. For 20 μm pixels a 3×3 matrix is always the best solution, no matter the readout noise; a spot with 25 μm FWHM is totally contained in a 3×3 matrix and using another ring of outer pixels does not add signal but only noise. On the contrary, for 13.5 μm pixels, the choice of the best spot size depends on the noise level with a break-even point around 5 electrons *rms*. This confirms our choice of using a 3×3 matrix for fast reading (10.2 electrons of readout noise) and a 5 × 5 matrix for slow reading (3.4 electrons). We found a similar trend in case of 450 eV photons (Panel (b)), although the profiles dramatically broaden. Except for ideal noise conditions around zero electrons, 5×5 spots are almost useless and give a resolution larger than the charge cloud FWHM for 10 electrons readout noise. 3×3 matrices work better, but with high noise, resolution is already of the order of 10 μm.

On the contrary SPC technique can be applied efficiently with hard X-rays as the estimates for 3000 eV photons demonstrate (Fig.(3.14c)). In all the tested conditions, resolution never exceeds 4.5 μm up to 10 electrons *rms* noise. A 3×3 matrix guarantees a resolution that is almost independent of noise, which stays around 3.5 μm for a 13.5 μm pixel and 2 μm for a 20 μm pixel. For low noise the best solution is represented by a 13.5 μm pixel with 5×5 spots, as in this energy range readout noise is negligible to the signal; so we should use the matrix size that encompasses all the charge cloud. Finally we compared the capabilities of 30 μm and 48 μm pixel detectors, with photons at 930 eV (Panel (d)). Although a 30 μm pixel is still small enough to give a resolution comparable with the 20 μm, especially for low noise, a 48 μm pixel is definitely too big for centroiding applications, as most of the photons generate single events on which the COM calculation does not work properly.

Simulations were also useful to evidence how COM calculation modifies a flat illumination field in different working conditions, leading to the already mentioned intensity oscillations (Fig.(3.15)). Considering a CCD with 13.5 μm pixel

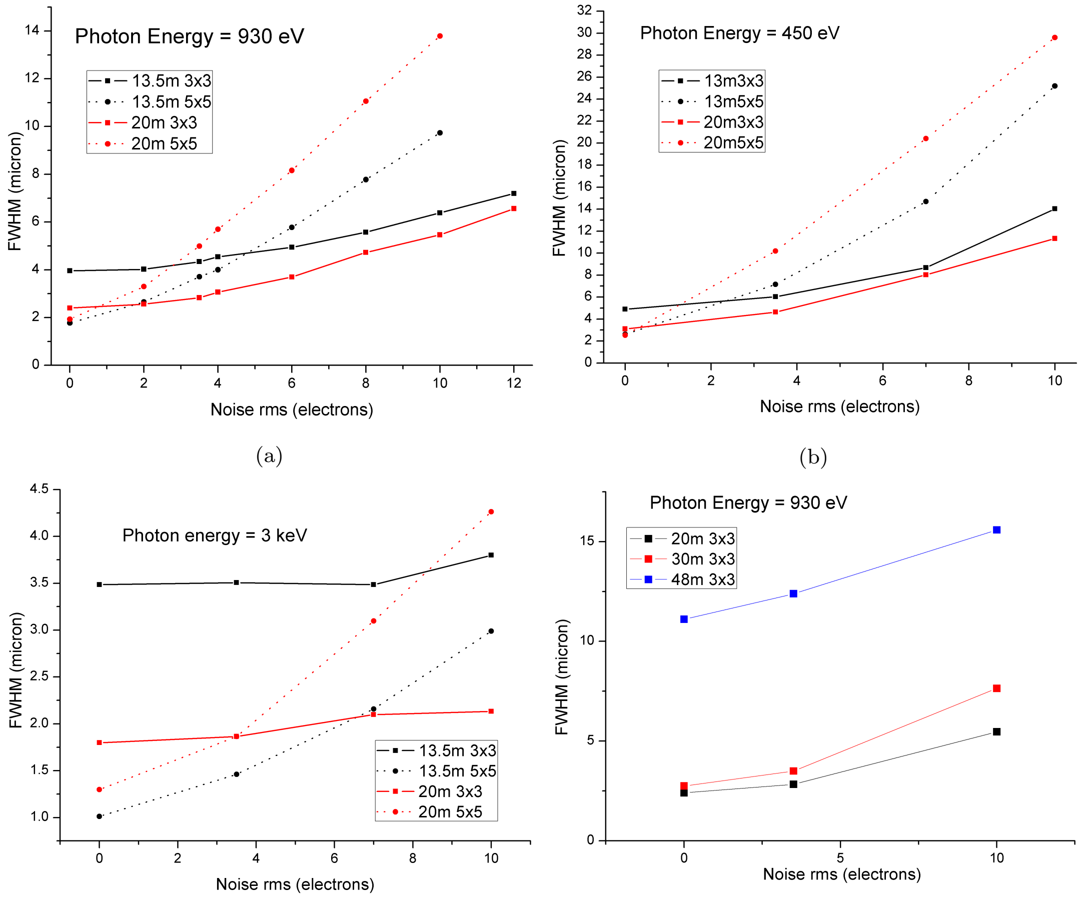

(a) (b) (c) (d)

Figure 3.14: Noise dependence of spectral resolution. Values are results from simulations.

size in homogeneous illumination, photon hits are randomly distributed all over the image (Panel (a)), but reconstruction with a 3×3 matrix concentrates COMs in the pixel centre generating an empty grid along pixel edges (Panel (b)). This problem is mainly due to the fact that we are leaving out the external part of the intensity distribution, indeed a 5×5 matrix succeeds in reconstructing the original flat distribution (Panel (c)). Noise has also the effect of randomly scattering the COM coordinates, resembling uniform illumination; however with a 3×3 spot 10 electrons *rms* readout noise is still not able to destroy completely the depleted grid (Panel (d)). From this last analysis one could wrongly conclude that the best solution for COM calculation is to use a 5×5 matrix; this is certainly true if noise is absent, but in presence of noise a 3×3 matrix, although introducing visible artefacts, is capable of spreading small features less, giving in general a finer spectral resolution. Moreover, excluding random variations, the

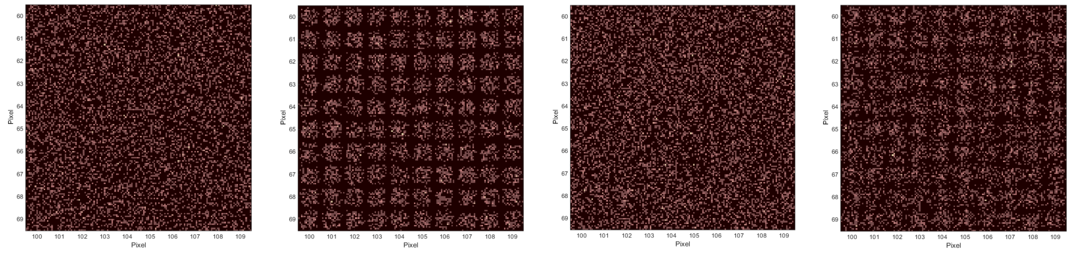

(a) (b) (c) (d)

Figure 3.15: Simulation of how the original photon position map (a) is reconstructed by the SPC algorithm on a CCD with 13.5 μm pixel size in different working conditions: 3×3 spot matrix, zero noise (a). 5×5 spot matrix, zero noise (c). 3×3 spot matrix, 10 electrons *rms* noise (d).

error on COM calculation is systematic and can be corrected to a certain extent using η or β algorithm.

3.6 η and β algorithm: ideal simulations

In this section we present the preliminary tests we carried out in order to evaluate the performance of η and β algorithm. We did not try to apply them to real measurements yet, but we limited our analysis to ideal computer simulations where we could keep track of all the notable working parameters. Before estimating the resolution achievable by η algorithm in an analogous way as we did for SPC, simulations were of fundamental importance to quantify how well it could compensate COM systematic error, or in other words how well we were able to reconstruct a flat illumination field. In testing the algorithms we carried out simulations at two consecutive levels of refinement. The first results, which we present in this section, were generated by shooting photons directly on a 3×3 matrix, distributing the spot centres uniformly in the central pixel. This was useful to evaluate the position-dependent reconstruction error before and after the application of the η algorithm. Of course this kind of simulation entails the fact that we already know the position of the true central pixel of the spot and no spot search is involved. This represents the abstract case in which we are able to locate exactly each spot, that, depending on noise level, could be far from reality. Hence the further step in simulation, whose results are described in the next section, is to take into account a spot search; in this more realistic case we simulated a complete image with a slope in order to evaluate the spectral resolution achievable, as we did for SPC. These simulations were

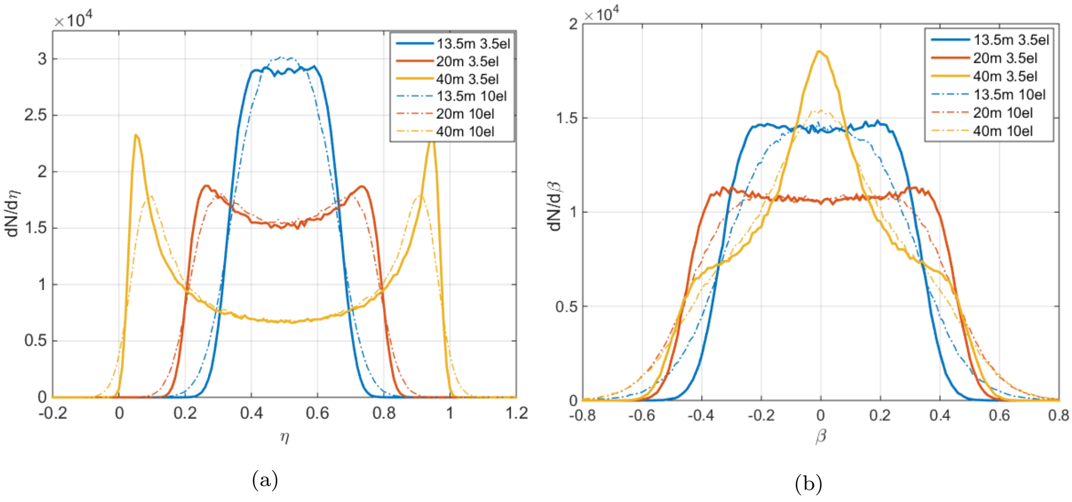

Figure 3.16: η (a) and β (b) distributions for different pixel sizes (13.5 μm, 20 μm, 40 μm) and readout noise equal to 3.5 electrons (solid lines) and 10 electrons (dash-dot lines). Each curve was simulated using 5×10^5 photons.

also useful to test the spot search algorithm in order to verify how many centres are mistaken. Although more realistic these are still single-photon like, in the sense that photons are shot and looked for one-by-one. This makes the use of intensity thresholds unnecessary and totally exclude double events. Moreover, as for SPC, we used only monochromatic photons. Unless explicitly declared, all the simulations consider 930 eV photons generating a 2D gaussian electron cloud with mean FWHM equal to 25 μm (refer to Section 3.5 for details).

η and β distributions

We start our discussion with a description of the η distribution, in order to understand how the corrected position of the impact point is evaluated. As explained in Chapter 2 the photon hit position within the cluster is fully characterised by the distribution $dN/d\eta$ evaluated in uniform illumination, whose shape takes into account statistically the non-linear charge splitting process and capacitive coupling between the pixels. Examples of simulated η and β distributions are respectively shown in Panel (a) and (b) of Fig.(3.16) for different lateral sizes of the pixel and noise levels corresponding to slow reading mode ($\simeq$ 3.5 electrons *rms*, solid lines) and fast reading ($\simeq$ 10 electrons *rms*, dash-dot lines). The shape of the η distribution gives information about charge sharing between adjacent pixels. With a 13.5 μm pixel charge sharing amounts to at least $\simeq$ 30% of the cluster total charge and is always present, as we cannot find any events with η around 0 or 1, but they are all concentrated in the centre. This also means that part of the charge cloud is collected by pixels outside the cluster. Furthermore the splitting process is roughly linear as the η distribution is flat. A similar situation persists with 20 μm pixel size, where charge splitting is still very effective, but more values of η are reachable and the distribution is larger. However two spikes at the edges of the distribution start developing and they sharpen using a 40 μm pixel. In this case the charge cloud FWHM is almost one half of the pixel dimension; hence if the photon hits the sensor near the border of a pixel charge sharing is effective and roughly linear, whereas if the impact position is close to the centre of the pixel, no charge splitting happens and η assumes values close to 0 or 1, contributing to the side peaks. These are not exactly centred at $\eta = 0$ or $\eta = 1$ because of coupling with the neighbouring pixels and the peak width is connected with the diffusion process and S/N ratio [61]. Readout noise has the effect of broadening the features of the distribution and allows a larger range of η values, even outside the interval $[0, 1]$ as if the true impact position were not between the centres of the left and right pixel of the cluster.

An analogous behaviour is exhibited by the β distribution. Now the value β is calculated with respect to the central pixel of a 3×3 cluster and thus it is symmetric around zero, extending roughly in the interval $[-0.5, +0.5]$. As before readout noise has the effect of smoothing and broadening the distribution. If the photon hits the centre of a 13.5 μm pixel charge sharing is approximately linear, but the number of entries goes to zero around ± 0.5, meaning that the charge cloud is not completely collected by the cluster, leading to a COM position which is systematically shifted and explaining why we found pixel borders depleted in SPC simulations with 13.5 μm pixel and 3×3 spot matrices (refer to Fig.(3.15)). The situation improves with a 20 μm pixel which exhibits a broader flat plateau extending in all the interval $[-0.5, +0.5]$, because the bigger pixel size is capable of gathering almost all the charge cloud, including the long tails. In this case also the linear correction (Eqn. 2.7, which corresponds to the COM correction) can shift the hit position x_P all over the central pixel of the spot with no fully depleted edges. If we increase pixel size to 40 μm a huge peak at $\eta = 0$ develops. In this case the pixel dimension is too big with respect to the charge cloud width, so photons hitting near the edges undergo charge sharing, whereas photons arriving

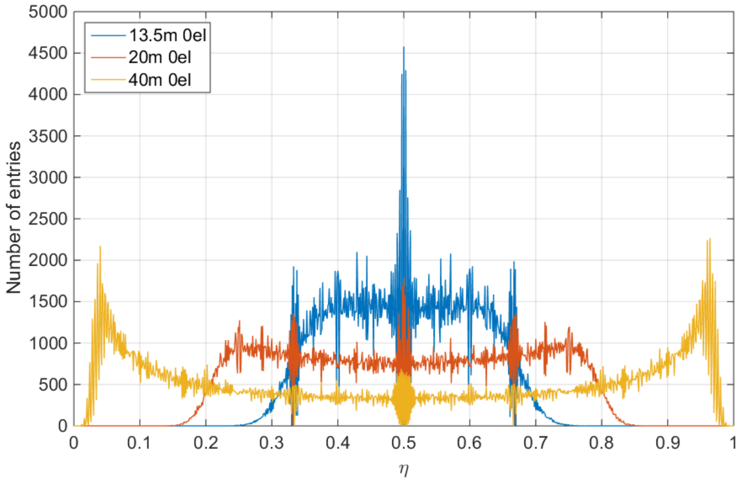

Figure 3.17: η distribution for different pixel sizes, with zero readout noise and using 1000 bins to generate the histogram. It is possible to notice the fast oscillations due to the discrete number of charges.

close to the centre mainly generates single events summing up to the central peak of the histogram. All the distribution shown were evaluated along the x direction, but as the charge cloud is modelled as centrosymmetric we obtained the same results in y, statistical uncertainty excluded. As expected $dN/d\eta$ and $dN/d\beta$ are also symmetrical under axial reflection through $\eta_0 = 0.5$ and $\beta_0 = 0$ respectively; slight asymmetries could be due to numerical rounding.

For low noise level η and β distributions exhibit a jagged and oscillating behaviour apparently incompatible with the intrinsic phenomenon. This is due to the discrete nature of the charge, which is constituted by a finite number of electrons. As each photon generates about 260 electrons, the variable η is not continuous but it is a fractional number given by all the possible combinations of ratios obtained by dividing the total number of electrons into two groups. Hence the obtained distribution is originally discrete and it is further discretised by dividing it into bins to generate the histogram. The distributions in Fig.(3.16) were generated using 100 bins, just for visualization convenience in order to plot a smoother function, but as we want a finer quantization of the possible corrections we generally employ 1000 bins to perform the following simulations, thus having η distributions with fast oscillating features as the ones shown in Fig.(3.17). The entity of the correction $f(\eta)$, necessary to find the photon position x_P, is given by Eqn. (2.9) for η and (2.11) for β algorithm and is shown in Fig.(3.18), also compared to the case of linear COM correction (Eqn.(2.7)). We have to point out that the real η and β distributions extend outside the intervals $[0, 1]$ and

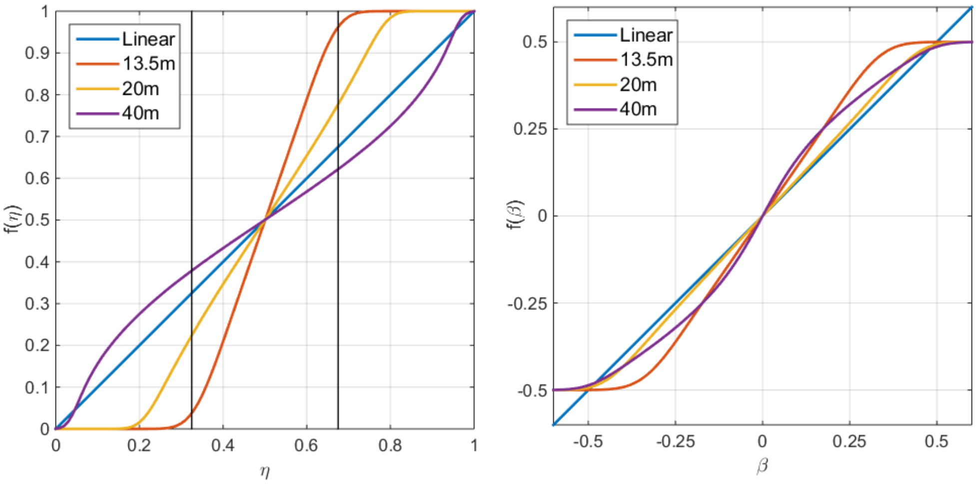

(a) (b)

Figure 3.18: Correction functions $f(\eta)$ (a) and $f(\beta)$ (b). The blue line corresponds to the linear COM correction given by Eqn.(2.7).

$[-0.5, 0.5]$ so, in calculating $f(\eta)$ the lower extreme of integration is changed to $-\infty$ and the correction is normalized over the entire real axis. The linear correction of the position (which corresponds to the COM calculation) is the blue straight line with unitary angular coefficient. If we apply the η algorithm (Panel (a)) with 13.5 μm and 20 μm pixel size we obtain a correction which is still almost linear in η although having a different slope. If we consider for example the case of 13.5 μm, there are no entries in the η distribution outside the interval $[0.3, 0.7]$; so in the central region of the plot (between the vertical black lines) the linear algorithm is not able to generate a correction that spans all the inter-pixel distance. On the contrary the η correction is still linear (because of linear charge sharing), but can redistribute the hit positions all over the pixel, without leaving the centre depleted.[1] With 20 μm pixel $f(\eta)$ has a smaller slope and gets closer to the linear case, justifying the better correction given by COM on a 20 μm CCD even using 3×3 spots. With 40 μm pixels the correction exhibits two bumps that separate it from linearity and are due to the lateral peaks that arise in $dN/d\eta$. Similar arguments can be applied to explain the shape of $f(\beta)$ (Panel (b)); in this

---

[1] In the η algorithm the correction is referred to the centre of the left pixel of the cluster and returns values between 0 and 1; so $f(\eta) = 0$ means that the photon hit in the centre of the left pixel, $f(\eta) = 1$ means it hit in the centre of the right one. If we are not able to assign these corrections, the centres of the pixels are depleted and not the edges as it happens with the SPC algorithm.

case 13.5 and 20 μm pixels have a linear behaviour and the latter is very close to the SPC correction (the blue line represents the SPC linear algorithm with 3×3 spots). The curves are detached the most from one another in the region near the edges of the pixel ($f(\beta) = \pm 0.5$), where the systematic error made by linear COM calculation is maximum [2]. The violet curve, corresponding to a 40 μm pixel, is not linear, due to the central peak in $dN/d\beta$. It is also important to note that values of η outside the range $[-0.5, +0.5]$ are given a correction inside this interval. This means that when the COM calculation gives a position β outside the central pixel of the spot, the correction $f(\beta)$ brings it back inside it. So with β algorithm once the spot is identified the photon is assigned to its central pixel, with no possibility of moving it to an adjacent one. In this case a correct and effective spot search becomes essential.

Intensity and error maps

After describing and understanding the shape of the distributions, we carried out some simulations to quantify the reconstruction error brought about by SPC (linear COM correction), η and β algorithms. We generated many 3×3 spots distributing the hit positions uniformly within the central pixel and for each of them we calculated the reconstructed position, according to the different algorithms. We divided the central pixel into a grid of 20×20 subpixels and we simulated a total of 5×10^5 photons, meaning an average of 1250 hits per subpixel. The reconstruction error, *i.e.* the distance between the true and the calculated centre of the spot, was evaluated for each subpixel and separated into a systematic and a random contribution. The systematic error was defined as the average of the reconstruction errors, whereas their standard deviation was identified with the random contribution due to the stochastic nature of charge diffusion[2]. Fig.(3.19) shows the results of the comparison between SPC, η and β algorithm, for a CCD with 13.5 μm pixel and 3.5 electrons *rms* readout noise. The three reconstruction methods were used on the same set of simulated photons in order to compare the results. η and β distributions were generated from analogous simulation of 5×10^5 photons, using the same parameters. The first row of figures shows the

---

[2] As we are working on a 2D sensor, the error contributions are plane vectors with a x and y component. In the error maps we show the norm of the mean error, so first we average the components and then we calculate the norm.

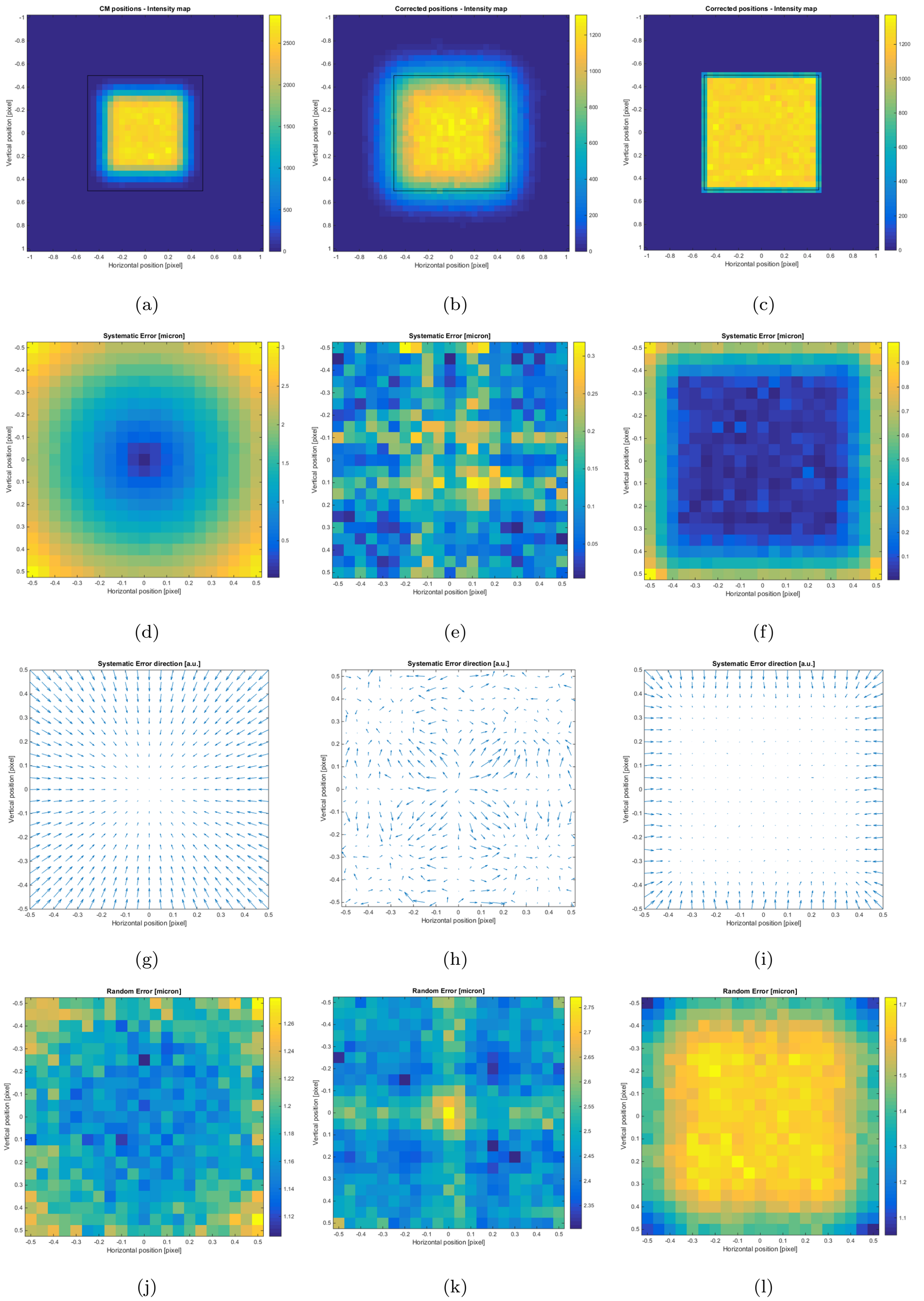

(a) (b) (c)

(d) (e) (f)

(g) (h) (i)

(j) (k) (l)

Figure 3.19: Comparative analysis of the errors generated by COM calculation with a 3×3 matrix (first column of images), η (second column) and β algorithm (third column). The quantities shown are the intensity map (first row), modulus of the systematic error (second row), direction of the systematic error (third row) and random error (fourth row). The data were simulated for a 13.5 μm pixel with 3.5 electrons readout noise.

intensity maps, that is the 2D photon position distributions, for the different methods used; the black line highlights the pixel edges. Unlike the analysis presented in previous sections, the pixel border does not coincide with the subpixel edge, but it cuts the subpixel in the half. This solution was preferred in order to avoid problems when assigning to subpixels photons hitting exactly on the pixel edge. As a consequence subpixels along the borders carry half of the intensity with respect to the ones inside the pixel, as it is clear from the true intensity map of the generated photons, which is plotted in Fig.(3.20a). The linear SPC algorithm with a 3×3 matrix (Panel (a)) confirms once again the results already obtained in the previous sections. COM calculation accumulates the photons towards the centre of the pixel depleting the edges completely and giving rise to the distinctive intensity oscillation already discussed. η algorithm is able to give a flatter distribution, but paying the price of moving many events in the wrong position outside the central pixel, resulting in a broader dispersion (Panel (b)). β algorithm instead reconstructs an almost perfectly flat intensity, also keeping all the photons inside the central pixel of the spot because $f(\beta)$ returns values in the interval $[-0.5, 0.5]$ (Panel(c)). The broader distribution of events created by the η algorithm is the result of the uncertainty on the choice of the right cluster: with a $13.5\,\mu$m pixel a 2×2 cluster collects only a small part of the photon charge, resulting in a bigger uncertainty with respect to the β algorithm which uses 3×3 matrices. We could expect a comparable performance of the two solutions only at a very high noise level. These results are better visualized by the COM all-in-one plots of Fig.(3.20b) which were obtained by integration of the intensity maps along the horizontal direction and suggest that β algorithm, except statistical fluctuations, follows the true flat intensity very well. Folding the all-in-one plots (Fig.(3.20c)) we get an idea of what happens in a uniformly illuminated region of the sensor. Both η and β techniques fully remove the oscillations given by the SPC algorithm; the former compensates the depleted edges of a pixel with the tails of the neighbouring one and the latter reconstructs a flat distribution in each pixel. The other rows of Fig.(3.19) show respectively the maps of the modulus of systematic error, its mean direction and the modulus of random error for the three different algorithms. The systematic error of COM calculation is zero in the centre of the pixel (here, according to Fig.(3.18) the linear correction is exact and coincides with the non-linear algo-

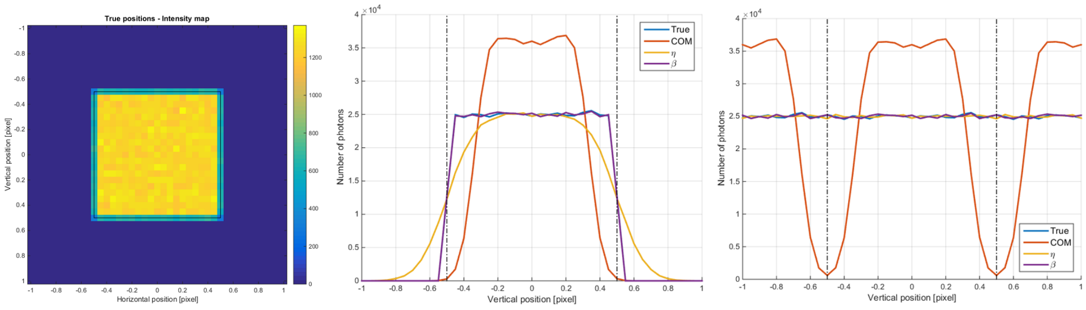

(a) (b) (c)

Figure 3.20: (a) True flat-field used to generate the results in Fig.(3.19). (b) All-in-one plots obtained by integrating the intensity maps along the horizontal direction. (c) Folded all-in-one plots show that both η and β algorithm are able to perfectly reconstruct a uniform illumination.

rithm) and increases towards the edges, touching a value of 3 μm in the corners, but with an average value of 1.7 μm within the pixel area. The evolution of the error is depicted in Panel (g) where the arrows point towards the direction of drop, which in this case is the centre of the pixel. The random error is instead almost constant around 1.2 μm. η and β algorithms well succeed in reducing and flattening the systematic error (Panel (e) and (f)), that is the goal for which they were developed, giving an average value of 0.1 μm and 0.3 μm respectively. Some residual systematic error remains along the two medians of the pixel for the η algorithm, giving a distinctive cross pattern, and along the pixel edges for the β algorithm, for which the central area of the pixel is perfectly flat. As the systematic correction is done through a statistical distribution, some uncertainty is added to the random error with respect to the SPC case. η algorithm gives an average random error of 2.5 μm, whereas β guarantees 1.5 μm, which is only slightly worse than SPC. We ascribe the large uncertainty of η algorithm to its use of 2×2 clusters which miss a non-negligible part of the signal, so we expect an improvement of its performance using 20 μm pixels, as it will be thoroughly demonstrated below. Furthermore β algorithm seems to mix what we called the systematic and random components of the error, by transferring systematic error to stochastic uncertainty. This is evident from the maps in Panel (f) and (l) which are complementary: subpixels with small systematic error have large random error and vice-versa. However in general, if we sum the systematic and random contributions, its maximum is found in the positions where the choice of the correct spot central pixel or cluster is more critical, which are linked to the events that requires correction values at the limit of the applicable interval.

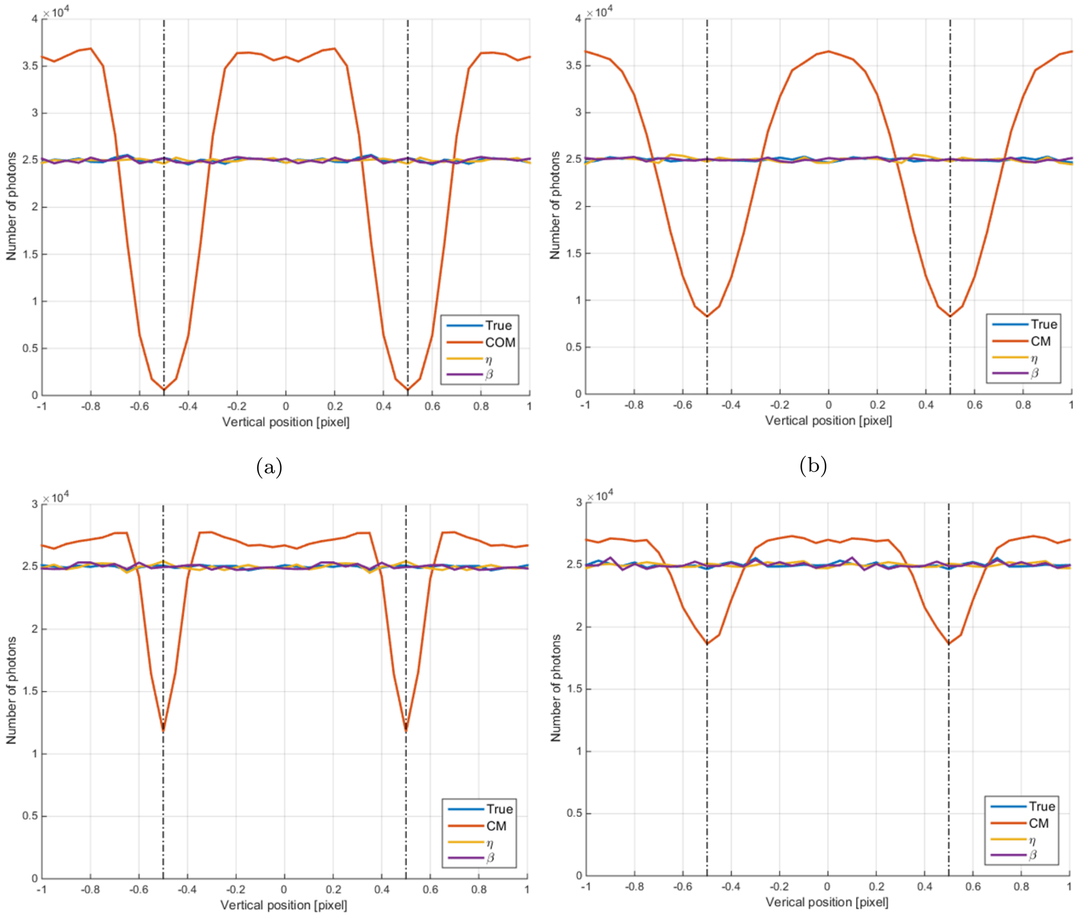

(a) (b)

(c) (d)

Figure 3.21: Folded all-in-one plots for different pixel sizes and noise levels: 13.5 μm, 3.5 electrons (a) and 10 electrons noise (b). 20 μm, 3.5 electrons (c) and 10 electrons noise (d).

This means that SPC and β algorithm are less precise at locating events along the edges of the pixel, whereas η gives worse results for photons hitting close to the pixel centre, as it makes use of 2×2 clusters.

We can now consider what happens by varying the noise level and the pixel size. We repeated this analysis on the examples most relevant for our needs, which were 13.5 μm and 20 μm lateral pixel size, at slow ($\simeq$ 3.5 electrons *rms* noise) and fast reading ($\simeq$ 10 electrons *rms* noise). The two relevant features of η and β algorithm, which were also the main motivations for their introduction are the reduction of the reconstruction error and the ability to reproduce a flat illumination without oscillations. The latter was inspected by using the folded all-in-one plots depicted in Fig.(3.21). In all the cases both η and β algorithm robustly reproduce a uniform intensity, whereas COM calculation always fails

		COM			η			β		
Pixel	Noise	Sys	Rnd	Tot	Sys	Rnd	Tot	Sys	Rnd	Tot
13.5	0	1.7	0.9	1.9	0.1	2.1	1.9	0.2	1.2	1.1
	3.5	1.7	1.2	2.0	0.1	2.5	2.2	0.3	1.5	1.4
	10	1.6	2.4	2.7	0.1	4.2	3.6	0.8	2.7	2.5
	12	1.6	2.9	3.0	0.1	4.8	4.2	1.0	3.1	2.9
20	0	0.6	1.0	1.1	0.1	1.5	1.4	0.1	1.1	1.0
	3.5	0.6	1.5	1.4	0.1	1.7	1.5	0.2	1.5	1.3
	10	0.5	3.2	2.8	0.2	2.9	2.5	0.6	2.9	2.6
	12	0.5	3.8	3.4	0.3	3.3	2.9	0.7	3.3	3.0

Table 3.2: Summary of systematic, random and total error obtained for the configurations we were mostly interested in. Values are a 2D average over the pixel and are expressed in μm.

(here the comparison was limited to the use of a 3×3 spot matrix, which anyhow represents the best choice for high noise level). The situation is particularly dramatic with a 13.5 μm pixel where 3×3 matrices leave out a lot of signal. Raising readout noise instead reduces the amplitude of the oscillations by randomly shifting the events. Apart from the reconstruction of a flat radiation field, the most relevant quality index to assess the performance of the different algorithms is the reconstruction error they introduce. In Tab.(3.2) we summarize the 2D average over the pixel of systematic, random and total error for the four configurations already considered and also in the ideal case of 0 and in the worse case of 12 electrons *rms* noise per pixel. The latter scenario is taken into account to evaluate possible CCDs with a readout faster than 1 MHz, which also means a higher readout noise. The total error is not trivially the sum of systematic and random error, because the former represents the mean systematic shift from the hit position and the latter is the dispersion of the values around it. Thus they are not homogeneous quantities from a logical point of view and cannot be summed directly. The total error is instead calculated as the mean of the moduli of the reconstruction errors, so that it keeps into account both random and systematic deviations and represents the best collective indicator to assess the algorithm performance. All the values are expressed in μm to make them directly comparable.

The table is only illustrative of the main configurations we were interested in,

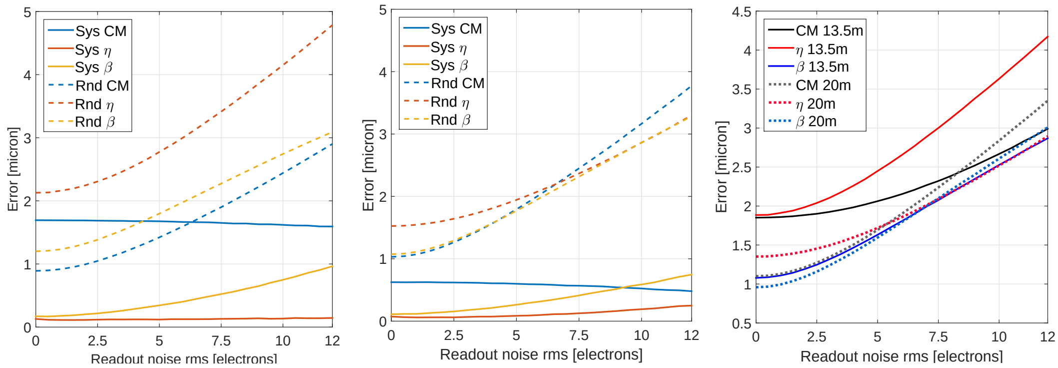

(a) (b) (c)

Figure 3.22: Simulation of the systematic (solid lines) and random error (dashed lines) as a function of the readout noise for 13.5 μm (a) and 20 μm pixels (b). Simulation of the total error as a function of the readout noise (c). Both pixel sizes are put on the same graph to compare them directly.

but in order to investigate thoroughly the evolution of the reconstruction error as a function of the readout noise, we repeated the simulations by varying noise from 0 to 12 electrons with steps of 0.5. Results are plotted in Fig.(3.22). Random and systematic error are shown separately for 13.5 μm in Panel (a) and 20 μm pixels in Panel (b), whereas Panel (c) outlines the total error for both pixel sizes. It is interesting to note that COM and η algorithm generate a systematic error which is around constant with the readout noise for both pixel sizes while the random dispersion of the values increases. η algorithm is able to cancel completely the systematic error, while, using β, it has a certain noise dependence, differently from the others. In general systematic shift is less pronounced with a bigger pixel that can collect almost completely the charge cloud. Random error, confirming its probabilistic origin, grows strongly with the readout noise. With a 13.5 μm pixel it has the same growing rate for all the three methods, but η algorithm introduce a degree of randomness that is twice the one of the others, probably due to the choice of the 2×2 cluster which is awkward with a small pixel. COM and β algorithm differ only by 0.25 μm, with the latter behaving worse because of the statistical correction with the distribution $dN/d\beta$. Different is the situation with the 20 μm pixel; at low noise COM and β act equally and η is still too much influenced by random contributions. On the other hand, at higher noise, η and β outdo COM and are more or less identical. As stated before, if we want to choose which algorithm to use, we should study the total error (Panel (c)) instead of considering the two components separately. It is clear that with a 13.5 μm pixel (solid lines), up to 12 electrons noise, β algorithm always performs better than the others and it has to be preferred to COM, that for large noise gives similar results, because it also solves the problem of oscillations. The η algorithm works improperly as it neglects too much signal, using 2×2 clusters. The situation is different with a 20 μm pixel, where, for large readout noise, η algorithm starts to be competitive. Indeed in this circumstance a 2×2 cluster is enough to store most of the charge cloud and η neglects 5 out of 9 pixels, keeping only the ones with highest SNR. As a conclusion, according to these preliminary ideal simulations, the best choice is to use β algorithm throughout the noise range with a 13.5 μm pixel. If using a 20 μm camera instead, we should prefer either β or η with low and high readout noise respectively.

3.7 η and β algorithm: simulated images

Although the total error is an effective index to quantify the quality of the reconstruction algorithms, we are ultimately interested in the assessment of the resolution achievable on the final spectrum. We evaluated it, as we did for SPC, by simulating a complete image with a blade stopping part of the photons. The resolution was again defined as the width of the transition between the dark and the illuminated region of the image. The simulations involved a spot search although photons were shot one by one thus preventing double events and fixing the total number of spots; furthermore only monochromatic light was taken into account. We considered a region of interest of (40×40) pixels which was partly covered by a blade starting at the 15th pixel row with a slope of 0.05. For each simulation we shot 1×10^6 photons with 930 eV energy. The distributions $dN/d\eta$ and $dN/d\beta$ were obtained by simulating a uniform illumination, considering 5×10^5 photons, under the same conditions used for generating the complete images. The results for the cases of main interest are summarized in Tab.(3.3) and visualized graphically by Fig.(3.23). For each simulation we reconstructed the photon positions with COM, η and β algorithm. The final spectrum was integrated using 21 channels per pixel. Resolution values follow broadly speaking the same trend of the total error given by the single spot simulations of the previous section. Considering a CCD with 13.5 μm pixel at zero noise, β algorithm works better by 1.5 μm with respect to the other techniques and guarantees a performance comparable to using a 20 μm pixel. The COM and η algorithm are

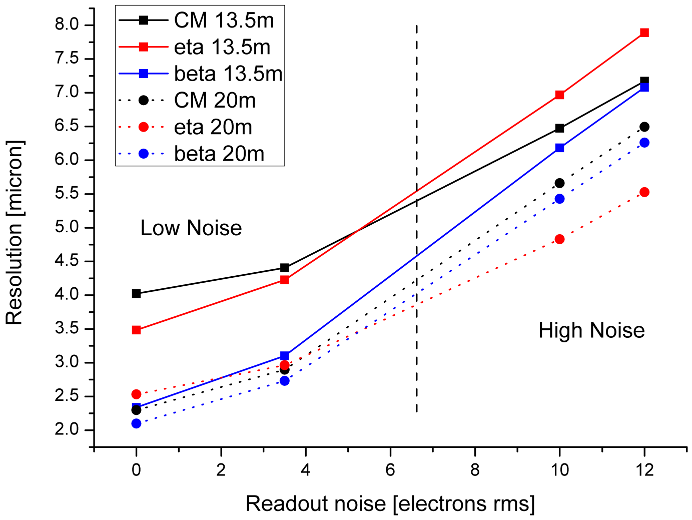

Figure 3.23: Resolution estimates as a function of readout noise. Values were calculated on simulated images.

Pixel	Noise	CM	η	β
13.5	0	4.0	3.5	2.3
	3.5	4.4	4.2	3.1
	10	6.5	7.0	6.2
	12	7.2	7.9	7.1
20	0	2.3	2.5	2.1
	3.5	2.9	3.0	2.7
	10	5.7	4.8	5.4
	12	6.5	5.5	6.3

Table 3.3: Resolution estimates from simulations of complete images, using COM (with 3×3 spots), η and β algorithms. Noise level is expressed in electrons *rms*, pixel lateral size and resolution values are in μm.

instead working similarly at low noise with the latter slightly better. With high readout noise COM and β reach 6.5-7 μm resolution, with β remaining below COM, while η is almost 1 μm worse than the other two, due to the big random noise. With a 20 μm pixel COM and β are very similar throughout the noise range considered. η has comparable performances at low noise but surpasses them by far with high noise, when the use of a 2×2 cluster keeps only the pixels with higher SNR. Yet η algorithm is not able to outdo the others with 13.5 μm pixels, because they are too small with respect to the spot lateral dimension.

The resolution estimates we found are on average twice the values of the total error. This could be compatible with the fact that we are integrating ideally along

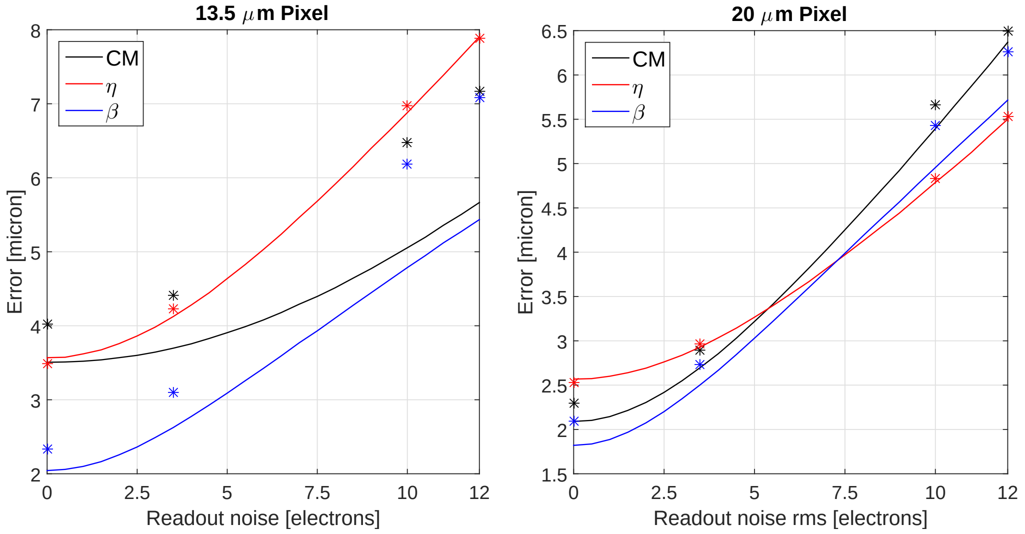

(a) (b)

Figure 3.24: Comparison between resolution estimates (star markers) and the corresponding total error profiles (solid lines) for a 13.5 μm (a) and 20 μm pixel (b). In order to compare the data, total error curves were enlarged by 1.9 times. Data from η algorithm agree very well, whereas COM and β would require a larger multiplicative constant. This points out a relative improvement of η algorithm with respect to what we expected from error simulations.

an inclined line, implying spot centre translation. Resolution and total error behave very similarly except for the η algorithm which gives better resolution results than expected if compared to the others. The relative improvement of η algorithm performance with respect to the other techniques is shown in Fig.(3.24) where we reproduced on the same plot the resolution datapoints and the total error profiles (multiplied times 1.9). We separated 13.5 μm (Panel (a)) and 20 μm (Panel (b)) data just for visualisation convenience. In both cases a scaling factor 1.9 is able to make the total error profile coinciding with the resolution data for the η algorithm (red line). On the contrary COM and β lines (black and blue respectively) stay below the resolution data, meaning that a higher scaling factor would be required. So we should look for a reason that is able to improve η algorithm performance with respect to the others.

We suppose that the disparity we have just highlighted between resolution estimates and total error could be due to the introduction, in later simulations, of the spot search as, apart from spectrum integration, which is though the same for all the algorithms, spot search represents the main difference between the two simulation frameworks we used. Indeed readout noise affects strongly the spot selection and altered spot recognition could deteriorate centroid determination,

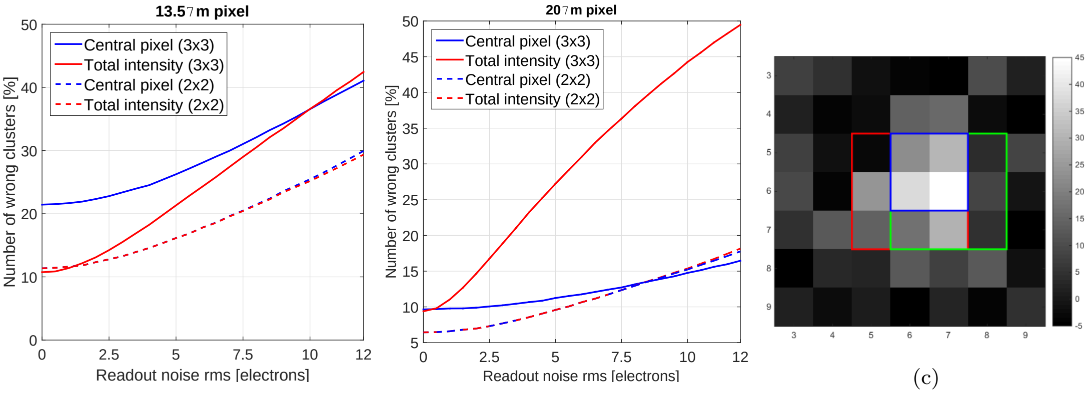

(a) (b) (c)

Figure 3.25: Simulation of the number of wrongly recognized spots as a function of readout noise for a 13.5 μm (a) and 20 μm (b) pixel detector. We considered the two spot search methods introduced in Section 2.2: central pixel and total intensity search. The dashed lines refer to the 2×2 cluster selection for the η algorithm, after the 3×3 spot has been looked for with the two mentioned methods. Panel (c) shows how a wrong spot recognition could bring to the right cluster selection. The correct spot is framed in red, the wrong one in green, but they both bring to the selection of the right 2×2 cluster (in blue). This can explain the generally better performance of cluster selection with respect to spot selection.

leading to a worsening of resolution. In order to test our hypothesis we simulated 1×10^6 photons and counted how many 3×3 spots and 2×2 clusters were recognized wrongly. Although in simulations done so far we were assigning the central pixel of the spot to the highest-intensity pixel, we also tested another method that makes use of the total intensity of the 3×3 spot matrix, which is described in Section 2.2. Results are shown in Panel(a) and (b) of Fig.(3.25) for pixels with 13.5 μm and 20 μm lateral size. The curves referring to 2×2 clusters represent the number of wrong clusters identified, after the 3×3 spots were searched using either the central pixel or the total intensity technique. With the smaller pixel, the total intensity technique is the one which gives the best results throughout the noise range. Central pixel method is not working properly at small noise level, with already 20% of wrong spots with zero noise, probably because of the pixel discretisation that is too fine. In any case the gap between the methods diminishes and at high noise they go through a comparable behaviour and with 12 electron noise the total number of wrong spots exceeds 40%. It is interesting the evolution of the number of wrong 2×2 clusters used by the η algorithm; The noise dependence is almost the same as the central pixel search, but improved by an offset of about 12% of the total number of spots. Moreover the two curves relative to the 2×2 clusters are alike. This can be understood by looking at Panel (c), which represents the intensity spot generated by a photon hitting in the central pixel of the image. The correct 3×3 matrix is the one in the red frame, giving the right 2×2 cluster in blue. If by chance we take the wrong spot (for example the green frame), nevertheless the selected 2×2 cluster is the same as before. Thus the choice of the 2×2 cluster is independent on the method used to select the original 3×3 spot, and η algorithm is often able to recognize the actual cluster even if it is starting from the wrong spot matrix. The uncertainty of the cluster choice with noise is mainly due to the fact that we are using a smaller matrix. Things change drastically with the 20 μm lateral pixel size; each pixel can collect more charge, so the central pixel method becomes very robust with respect to readout noise and even at 12 electrons, the number of wrong spots is a little more than 15%. On the contrary the total intensity search is strongly affected by noise and with 12 electrons it mistakes half of the spots. As before the curves referring to 2×2 clusters are identical, but in this case they do not exhibit the same dependence as the central pixel curve. Anyway they give good results, with only 6% of wrong spots at zero noise, and 17% at 12 electrons, a value comparable with the central pixel search for 3×3 spots. The peculiar behaviour of the 2×2 cluster search we described could partly explain the improvement of the η algorithm we noticed, although the real situation is probably more complex and the final spectral resolution depends on many variables.

The data simulated for the evaluation of resolution were also useful to inspect directly if the reconstruction of a uniformly illuminated area was working correctly. We had already checked this with the all-in-one plots of Fig.(3.21), but we were working with single pixel simulations, whereas afterwards we could use an entire image. Fig.(3.26) shows a 2D uniform intensity region of a simulated image reconstructed with COM, η and β algorithm, in case of a 13.5 μm pixel with 3.5 electrons readout noise. Once again the COM shows its typical depleted grid in correspondence with pixel edges. η and β algorithm are instead both able to reconstruct the flat illumination perfectly, as we have already verified from the folded all-in-one plots. However we should keep in mind that flat-field illumination is a rather unusual situation, because it requires each pixel to be surrounded by pixels with the same number of photons on average. This means that even if reconstruction within the single pixel were not correct, it could be compensated by the nearest neighbours. This is exactly the same process occurring when we fold the all-in-one plot. Although the single histogram may not represent ex-

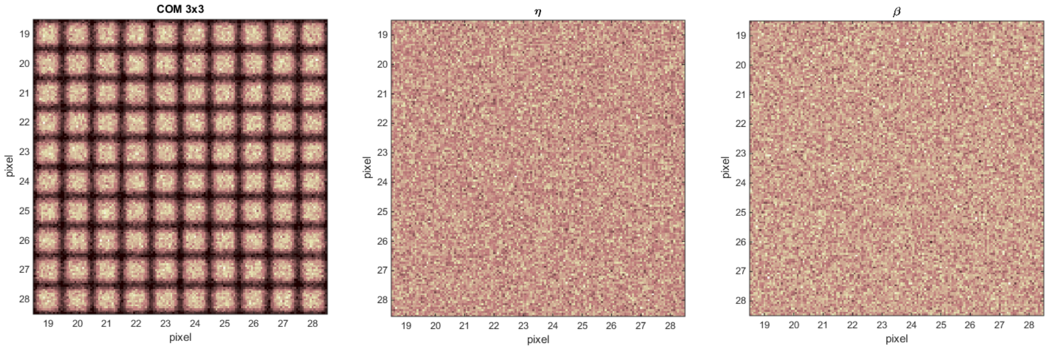

(a) (b) (c)

Figure 3.26: Simulation of flat-field illumination reconstructed by COM 3×3 (a), η (b) and β algorithm (c), using a 13.5 μm detector with 3.5 electrons readout noise.

actly the flat field, being depleted on the border, tails of events coming from histograms centred on the nearest neighbours sum up and flatten the intensity. As we are mainly interested in the narrow features of the spectrum and not on the flat regions we should have a look at what the intensity map looks like along the frame and the razor blade edge. A small region of 4×8 pixels, cut by the blade, is depicted in Fig.(3.27), where we used a simulated image with 13.5 μm pixels and 10 electrons *rms* noise. Panel (a) shows the actual simulated photons and the transition between light and dark is extremely sharp. Panel (b) is the same portion of the image reconstructed with the COM using a 3×3 spot matrix. The high level of noise is still not enough to fill up the depleted edges. The transition is broadened by noise and retains the oscillating pattern. The events deteriorating resolution, i.e. the ones relocated into the dark region, are either due to wrong COM calculation altered by noise, or to wrong spot recognition. The η algorithm (Panel (c)) broadens the cut isotropically with no evidence of artefacts. On the contrary β algorithm, although exhibiting a perfectly flat intensity in the central region, displays a depleted line when close to a light-dark transition, as it is visible along both the edge of the image and the razor blade. The depleted line runs along the pixel edge and is connected to the fact that once the spot has been selected, β algorithm produces a position correction inside the interval $[-0.5, 0.5]$. This means that once the spot has been chosen the photon is definitively assigned to a pixel. What happens in our example is that some events hitting near the pixel edge generates spots that are wrongly assigned to the adjacent pixel. So some photons are transferred to the other side of the pixel edge, leaving a typical depleted line. This deviation is instead compensated by

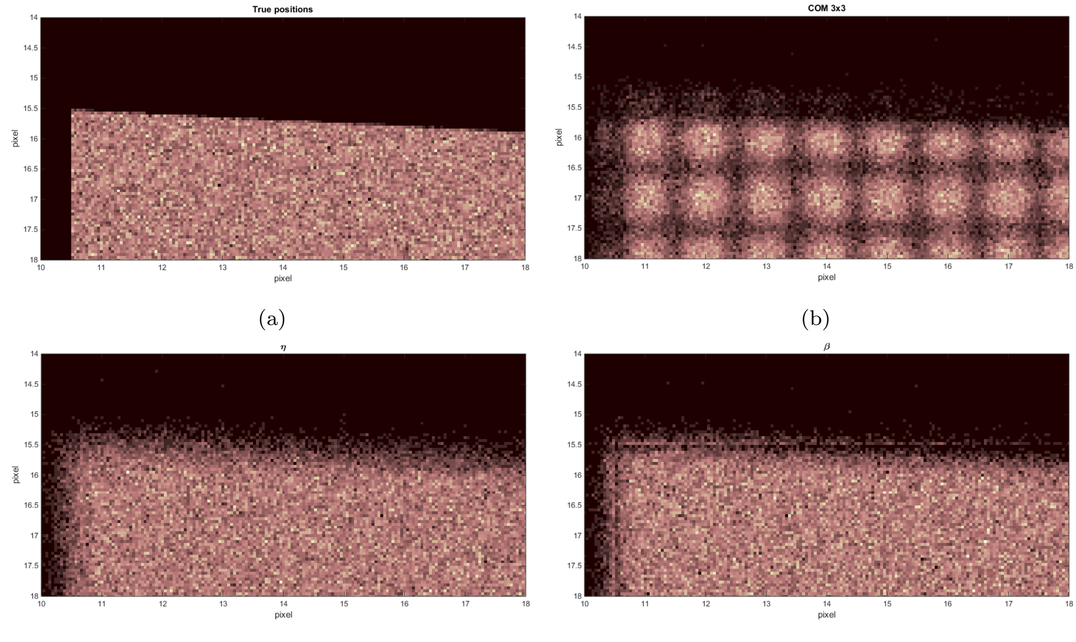

(a) (b)

(c) (d)

Figure 3.27: Detail of a region along the blade taken from a complete simulated image. The true image (a) was reconstructed by COM 3×3 (b), η (c) and β algorithm (d). It is possible to notice the artefacts introduced by the different techniques. Simulation were carried out using $13.5\,\mu$m pixels with 10 electrons readout noise.

nearest-neighbouring pixels in flat-field regions.

3.8 Conclusions and future perspectives

The simulations we carried out comparing the performances of COM, η and β algorithm clearly demonstrate that, according to the assumptions we made, η and β are able to reduce considerably the systematic error due to COM calculation, leading to two main advantages: on the one hand the intensity oscillations are completely removed and on the other hand the overall resolution is improved within the readout noise range we studied. These results encourage the possibility of successfully implementing η and β algorithms on the beamline. These, in combination with the already verified traditional algorithm, could provide a remarkable versatility to ERIXS and users could select the most suitable algorithm according to their needs: η or β if high resolution is required or the traditional one if faster measures at lower resolution are preferred. The assessment of the algorithms is not concluded yet, because we focused our investigations on photon energies of 930 eV. An important question is how η and β behave at lower energies, when the signal to noise ratio is reduced, and which their ultimate working limit is. Further improvements of the algorithms can be also imagined and we have in mind to test some of them in the future. A first idea is to consider a truly 2D η (and β) distribution, so that the x and y direction are not decoupled and it should be possible to define a 2D correction function $f(x, y)$. Another possible variation could be a compromise between η and β, using a 2×3 cluster. This method could be less sensitive to noise than β, leaving out three low signal pixels, and at the same time it could be less uncertain than η in the choice of the cluster.

Chapter 4

Magnetism in high-T_c superconducting cuprates

The present chapter consists in an introduction to the main phenomenology of high-T_c superconductivity in layered cuprates. Without the claim of being exhaustive in presenting the topic, which is very hot in current research, we will focus on the aspects that are most relevant for understanding the experimental results presented in next chapter. We will start by introducing the general structure of the cuprate families we inspected, stressing the common features among them, and continue by giving a hint at their character of strongly correlated electron systems. The last section is directly connected with the experiment we carried out and is a general introduction to the magnetic phases that develop inside cuprates.

4.1 High-T_c superconductivity in cuprates

Since its discovery in 1986 by Bednorz and Müller [5], high-T_c superconductivity has been representing one of the most long-lasting mysteries of recent condensed matter physics. A lot of effort has been put in its study by both experimental and theoretical scientists because on the one hand it made possible to envisage revolutionary technological applications and on the other hand high-T_c materials truly represent a “zoo” of complex and unconventional physical phenomena. As it became clear since the beginning, high-T_c superconductivity was not explained in terms of the BCS theory and a complete microscopic model is still lacking.

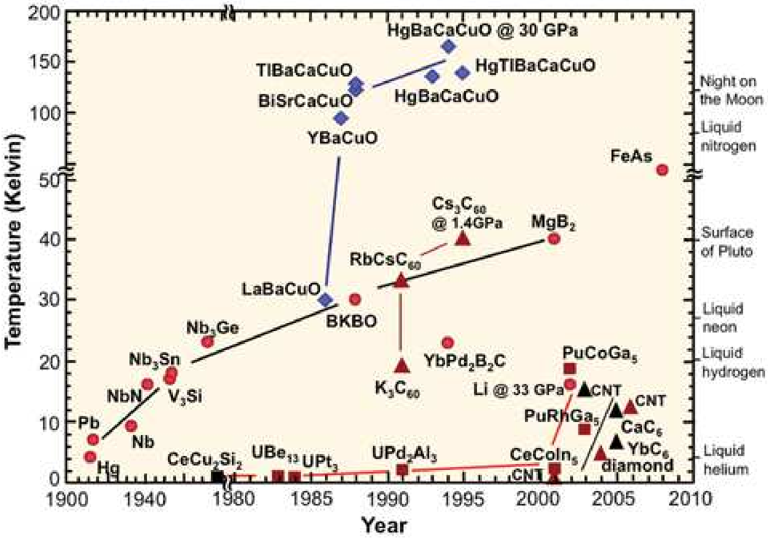

Figure 4.1: Timeline of the discovery of superconducting materials. Blue diamonds mark the high-T_c cuprates in which superconductivity was first observed in 1986 by Bednorz and Müller [5].

However thousands of experimental observations have been accumulated and, with our experiment, we also tried to add a tiny piece to this fascinating puzzle. If we look at the timeline of superconductor discovery in Fig.(4.1) the importance of layered cuprates (blue diamonds) is immediately evident, not only from an historical point of view, because they were the first systems in which the new phenomenon of high-T_c superconductivity was observed, but also because they are the ones reaching the highest T_c, even above the boiling temperature of liquid nitrogen, thus facilitating their experimental inspection.

Most of the high-T_c superconductors, or at least the ones we are interested in, share some structural features and form similar crystals. The basic building block they adopt is the perovskite structure ABO_3 of Fig.(4.2a) where A and B are metallic cations and O is oxygen. The larger cation (A) occupies the corners of a cubic structure, whereas B is in the centre. Oxygen atoms surround B forming an octahedron. This basic structure, depending on the relative volume of the ions can be distorted often adopting an orthorhombic cell [43]. The word *cuprate* indicates systems which contain copper anions in the positions B of the perovskite structure and these can be distinguished into many families. We start our introduction from the so-called “214” cuprate family which includes $La_{2-x}Sr_xCuO_4$ (LSCO). Fig.(4.2b) shows the unit cell of the antiferromagnetic parent compound La_2CuO_4 (LCO, in which $x = 0$), in which the octahedra of the perovskite structure are evidenced. However rather than thinking of it in terms of a cubic sub-lattice, it can be seen as a layered structure alternating a CuO_2 and two LaO planes. By varying temperature and the relative La-Sr concentration x a structural transition occurs, passing from an orthorhombic to a tetragonal crystal [28]. CuO_2 planes exhibit a square lattice in which each Cu^{2+} ion forms a squared plaquette with its four nearest-neighbouring O^{2-} in the corners (compare with Fig.(4.7)). The presence of these planes is a common feature of almost all cuprates and it is believed to play an important role in high-T_c superconductivity. The other most widely studied cuprates are the ones belonging to the so-called "123" family with formula $RBa_2Cu_3O_{6+x}$ with $R = Y, Nd$ (YBCO and NBCO) or another rare earth element. In particular YBCO was the first system found with T_c higher than the boiling point of liquid nitrogen (77 K). The unit cell of $YBa_2Cu_3O_7$ is depicted in Fig.(4.2c). As in the previous case we can think of the crystal as a stacking of different layers along the crystallographic c axis (perpendicular to the CuO_2 planes), from bottom to top: CuO-BaO-CuO_2-Y-CuO_2-BaO-CuO. In the arrangement of atoms it is still possible to see elements of the perovskite structure (light blue shaded regions). Copper atoms are distinguished according to their position in the crystal structure: Cu2 atoms form the usual CuO_2 planes with tetragonal coordination whereas Cu1 atoms arrange in CuO chains with linear coordination. As already mentioned, the most important feature of the cuprate structure introduced so far is the presence of CuO_2 planes, where the electronic configuration of Cu^{2+} atoms is $3d^9$ meaning that only one out of ten d orbitals is not filled. The degeneracy of these levels is removed by the *crystal field* generated by the oxygen ligands and according to the geometrical environment the highest energy orbital is $d_{x^2-y^2}$ whose lobes point towards the four in-plane oxygen ions. For the sake of simplicity it is common to describe the electronic state of cuprates in terms of the single $3d$ hole, which mainly have $d_{x^2-y^2}$ character [11]. CuO_2 planes are retained so important in determining the properties of cuprates that these materials are often described in terms of quasi-2D systems. Having an external shell not completely filled cuprates would be expected to have metallic behaviour, according to a single electron picture. Nevertheless they are insulators because adding an electron to the outer shell requires to overcome a large Coulomb repulsion. Therefore a mean-field theory cannot describe their electronic properties and this justify the name of *strongly correlated electron systems* which is often given to these materials.

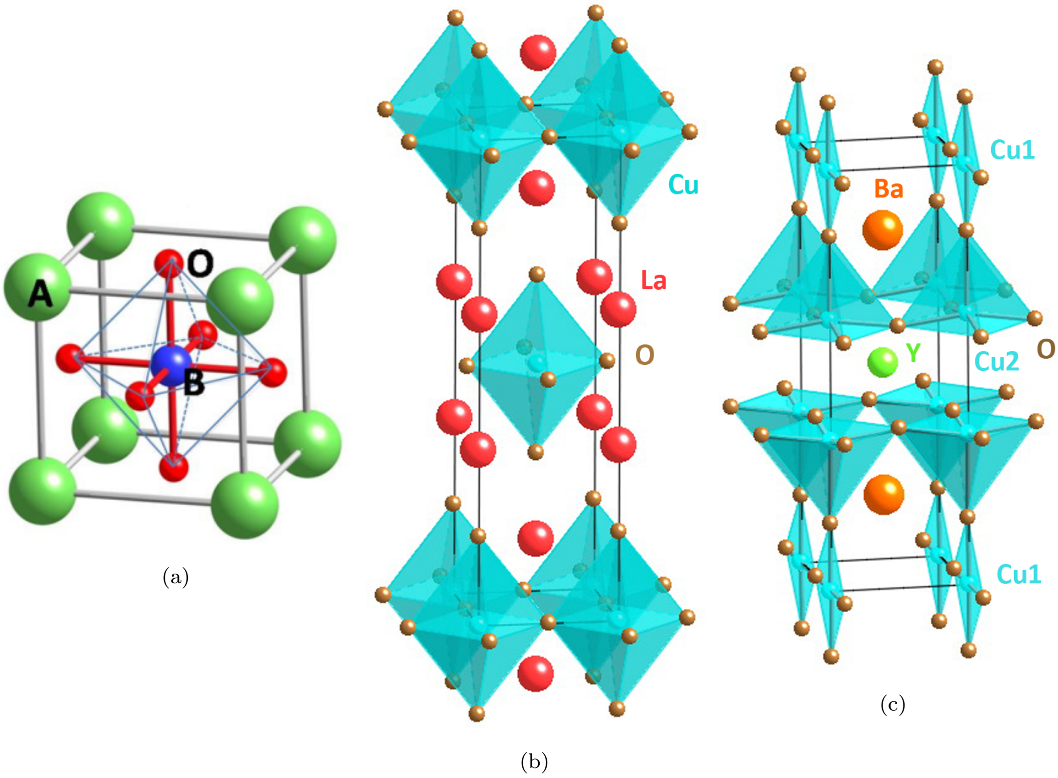

(a) (b) (c)

Figure 4.2: (a) Perovskite structure, which can be considered the basic building block of cuprate systems. (b) Unit cell of La_2CuO_4. (c) Unit cell of $YBa_2Cu_3O_7$.

The parent compounds of cuprate superconductors are called undoped meaning that they do not carry extra charge in the CuO_2 planes. Due to the unpaired electron Cu^{2+} ions have spin $S = 1/2$ and develop a long-range antiferromagnetic order thanks to super-exchange interaction. This order extends three-dimensionally, although in many cases CuO_2 planes can be considered independent because the in-plane coupling constant is stonger than the inter-plane one by many orders of magnitude [28]. The parent compound can be doped by changing its chemical composition according to the stoichiometric formula, which is usually done by adding oxygens or substituting ions with a different valence. Doping modifies the layers lying between CuO_2 planes which are actually named *charge reservoirs* or *blocking* layers as they regulate the number of electrons in CuO_2 planes. For example, in $YBa_2Cu_3O_{6+x}$ the hole concentration per planar Cu ion p is adjusted by changing the number of oxygens in the Cu1 chains. By varying x it is then possible to explore all the doping levels from $x = 0$ ($YBa_2Cu_3O_6$, undoped) where no oxygen is present in the chains to $x = 1$ ($YBa_2Cu_3O_7$, overdoped) where all the chains are completely saturated [40] (The

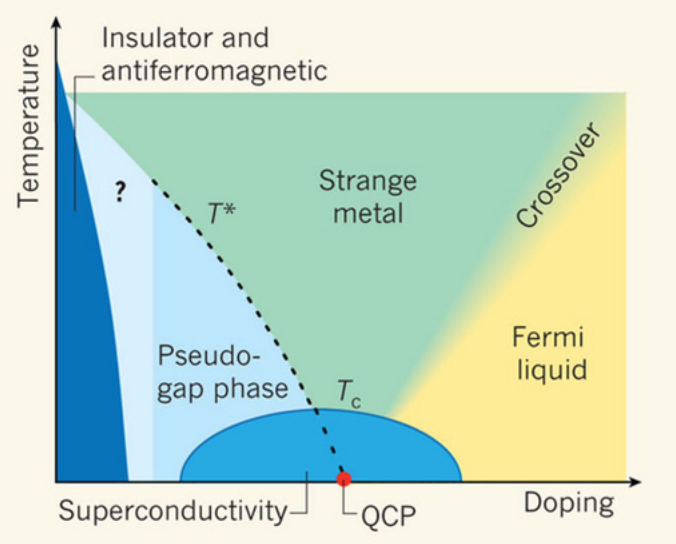

Figure 4.3: Typical phase diagram for a hole-doped high-T_c cuprate superconductor.

procedure to evaluate the doping $p$in the CuO$_2$ planes from the oxygen content x is described in [36]). For intermediate levels of x it is possible to recognize different arrangements of the oxygen donors in the chains and pass through several structural phases as the doping is increased [28, 6]. In LSCO instead the doping is controlled by changing the La/Sr ratio. The superconducting phase doesn't occur in the insulating parent compound, but appears with doping. The introduction of charges in the CuO$_2$ planes destroys the long-range antiferromagnetic order leaving only short-range correlations that are anyway able to keep the in-plane antiferromagnetic alignment. Upon doping the material passes through many different transitions showing a rich quantity of behaviours and for this reason the phase diagram of high-T_c cuprates is represented as a function of doping and temperature as depicted in Fig.(4.3) for a typical hole-doped superconductor. By increasing the doping the initially insulating system enters the superconducting phase, which is often referred to as the *dome*, due to its particular shape. The critical temperature T_c increases in the so-called *underdoped* region until reaching a maximum, when the material is defined *optimally doped*. If we add more holes T_c drops in the *overdoped* region, until the system becomes a low conductivity Fermi metal. Above the superconducting dome, the *pseudo-gap* region extends, whose name points out the presence of a partial energy gap characterized by a minimum in the density of states near the Fermi energy, that seems to be a precursor of the real gap opening in the superconducting phase.

The onset of the pseudogap region was evidenced by many different measuring techniques that highlighted anomalous evolution of transport, magnetic, optical and thermodynamic properties [42]. The interesting thing is that the starting point of these observations occurs at a temperature T^* larger than T_c. After the first experimental measurements drew attention to this phenomenon, several repetitions were carried out in order to investigate the doping dependence of T^* and it was found that it drops with increasing doping, finishing somewhere inside the superconducting dome where, due to the onset of superconductivity, it becomes more challenging to investigate the pseudogap properties. Actually the main difficulties in explaining the pseudogap are already connected with its definition. Most of the phenomena found in this region of the phase diagram, although having a similar decreasing doping dependence, shows onset temperatures slightly different among each other, so that even the definition of T^* is not unambiguous. Actually there has been no evidence yet that the pseudogap is a true thermodynamic transition with a fixed temperature, and this opened the way to two different interpretations [32]. For some theorists T^* represents a symmetry breaking phase that goes towards a quantum critical point (QCP) inside the superconducting region. The other picture is that T^* marks a crossover to superconductivity characterized by the creation of pre-formed pairs that completely condense only at T_c, in analogy with a magnetic transition.

It is common belief that in order to understand the rise of high-T_c superconductivity we should be able to understand the normal phase from which it originates and a definitive microscopic mechanism for superconductivity indeed has to be capable of explaining all the wealth of physical phenomena characterizing the whole phase diagram of cuprates. Much effort has been reserved to the study of the pseudogap phase where particular charge and spin orders have been found out. Apart from the already mentioned long-range antiferromagnetism characterizing the undoped parent compound, cuprates of the "214" family showed, developing in the pseudogap phase, a uniaxial modulation of spin and charge that was named *stripe order* [59]. To comprehend how stripes form it is necessary to understand what happens to doping charges when they are added to CuO_2 planes. Many scientists believe that every hole added to the system is delocalized over the four oxygen atoms surrounding the central copper of a plaquette. As the hole carries a spin as well, which is in the opposite direction with

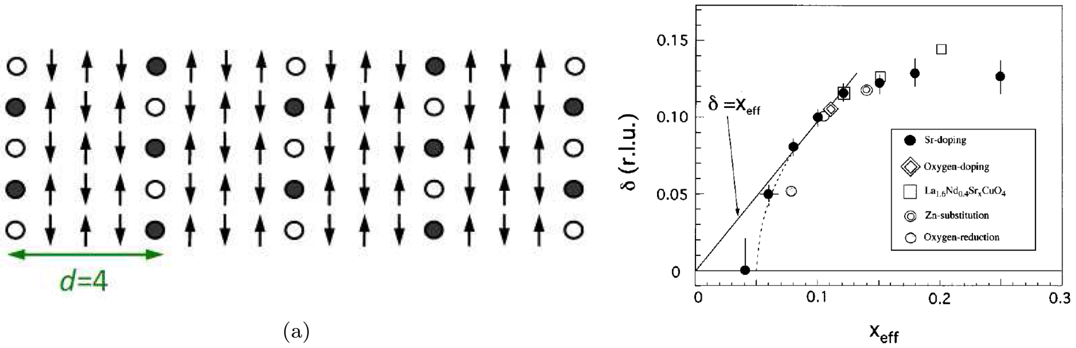

(a)

(b)

Figure 4.4: (a) Pictorial scheme of the arrangement of stripe order in the CuO_2 planes of LSCO. The circles represent the doping holes that constitute impurities of the 2D antiferromagnetic lattice. The uniaxial spin periodicity is twice the charge one. (b) So-called “Yamada plot”, showing the evolution of the incommensurability parameter δ with doping. After a linear increase δ flattens out at $x \simeq 1/8$. Taken from [63].

respect to the unpaired hole on the copper, it locally destroys the long-range antiferromagnetic order by quenching the superexchange interaction, diluting the 2D Heisenberg lattice. However a theoretical model [37, 49] describing the energetic balance between superexchange and Coulomb repulsion demonstrated that it is convenient for the added holes to form separate regions arranging in long stripes. Upon doping the periodicity d of charge stripes shortens until reaching the value of $d = 4a$, where $a \approx 3.8$Å is the lattice unit of the CuO_2 plane (distance between two equivalent Cu2 atoms). Once this critical density of stripes has been reached it is more convenient to increase the filling factor of each stripe (how much charge is contained within the stripe) than to further reduce the period d. This final situation is depicted in Fig.(4.4a) where the circles represent impurities in the 2D antiferromagnetic lattice (symbolized by the black arrows). As evidenced by this simple sketch, the onset of the charge periodicity, give rise to an equivalent uniaxial spin modulation with twice the period of the stripe order. A trace of this was observed with inelastic neutron scattering experiments which are sensitive to spin ordering [14, 63]. As the presence of stripes creates a superlattice on top of the antiferromagnetic order, instead of finding the diffraction peak at $\mathbf{q}_{AF} = (1/2, 1/2)$ in the reciprocal lattice (values of the momentum $\mathbf{q}$ are expressed in rlu *i.e.* reciprocal lattice units), as exhibited by the undoped parent compound, peaks were found at an incommensurate distance δ from this point. Yamada *et al.* [63] studied the dependence of the incommensurability δ as a function of doping level x and discovered that after a slightly linear behaviour

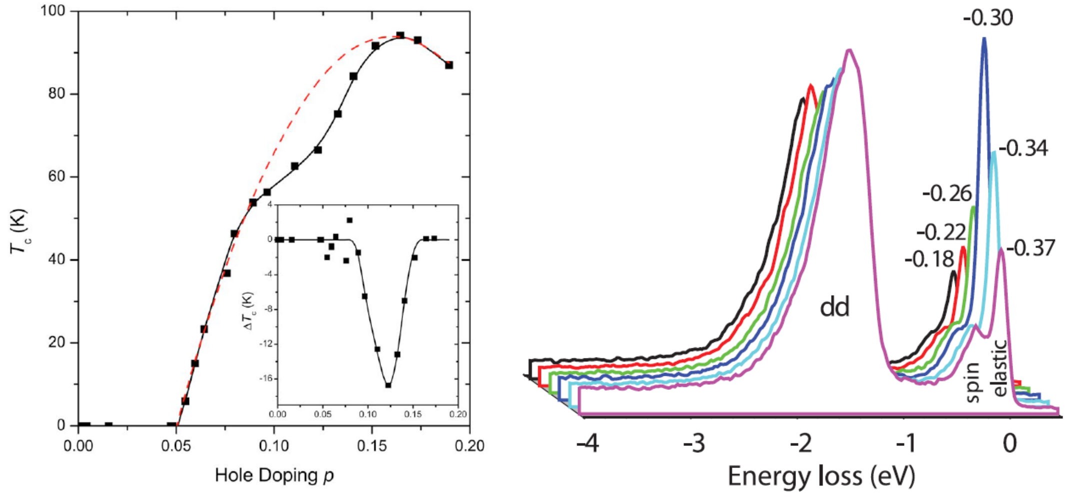

(a) (b)

Figure 4.5: (a) Doping dependence of the critical temperature T_c of YBCO, which shows the so-called *plateau* moving away from the dashed parabolic line, whit a maximum suppression at $p \simeq 1/8$. Image taken from [36]. (b) RIXS spectra showing a maximum of the quasi-elastic peak at transferred momentum $\mathbf{q}_{\|} \simeq 0.31$ rlu, which is evidence of the onset of incommensurate charge density order. Image taken from [22].

it tended to saturate to $\delta \simeq 1/8$, which relates to the commensurate periodicity $d = 4a$. The doping dependence was summarized in the so-called "Yamada plot" that is reproduced in Fig.(4.4b). This behaviour is in good agreement with the proposed theories and also shed some light on the connection between stripes and superconductivity. Indeed the phase diagram displayed a suppression of the critical temperature T_c for doping close to $p = 1/8$ which is the same value at which stripes stabilize. Furthermore neutron scattering experiments also showed an anomalous reduction of the incommensurate peak width at this level of doping, which is related to the inverse coherence length of the spin fluctuations [63]. All these observations suggest that stripes, pseudogap phase and superconductivity are strongly linked to each other, but the bigger picture is still missing and it should still be understood in which way stripes are hastening or preempting superconductivity.

After the discovery of stripes physicists wanted to understand if they were a peculiar phenomenon of LSCO family or a general feature of all the cuprates; so they started to look for other examples especially in the "123" family. However INS experiments on these materials revealed the presence of an energy gap in the dispersion of spin excitations [51] and the absence of Bragg elastic peaks compatibles with a static spin order [29], but anyway this was not ruling out the

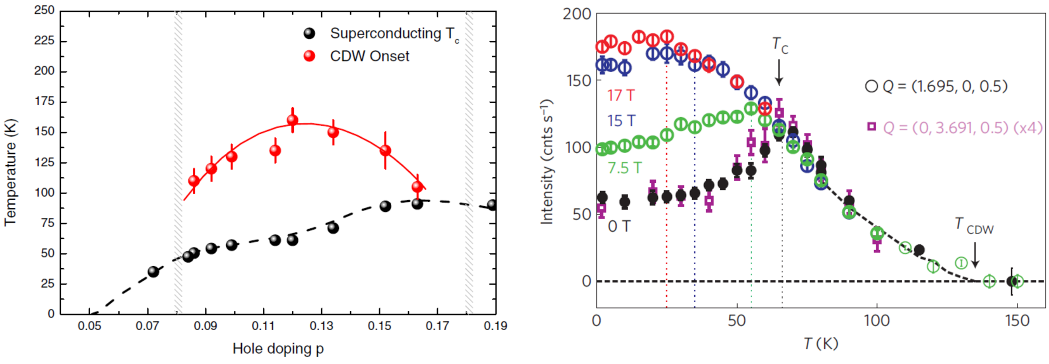

(a) (b)

Figure 4.6: (a) Doping dependence of the onset temperature of CDWs in YBCO. T_{CDW} exhibits a maximum approximately in correspondence with the maximum suppression of T_c. Taken from [6]. (b) Temperature dependence of the CDW peak intensity for increasing applied magnetic field. The charge order seems to be suppressed by the onset of superconductivity and stabilized by the magnetic field. Taken from [10].

presence of fluctuating stripes or a charge order. The interesting region to investigate was again the pseudogap phase where also $YBa_2Cu_3O_{6+x}$ systems exhibit an anomalous suppression of the critical temperature T_c that forms the so-called *plateau* shown in Fig.(4.5a) in proximity to doping $p \simeq 1/8$ [36]. X-ray scattering revealed the presence of 2D modulations of the charge density in CuO_2 planes [22, 10], which were identified as *Charge density waves* (CDW). In particular RIXS spectra, reproduced in Fig.(4.5b), showed an anomalous enhancement of the quasi-elastic peak at transferred momentum $\mathbf{q}_{||} \simeq 0.31\,\mathrm{rlu}$ (reciprocal lattice units). The periodicity is incommensurate and different from the one found for stripes in LSCO ($\mathbf{q}_{||} \simeq 0.25\,\mathrm{rlu}$). Furthermore as RIXS is a resonant process the excitation could be unambiguously assigned to Cu2 atoms, meaning that charge modulation occurred in CuO_2 planes and additional tests confirmed that the peak was due to charge modulation rather than spin [22]. Since the first observations in 2012, more systematic experiments have been carried out in order to study the doping dependence of CDWs and try to understand their relationship with superconductivity. The presence of CDWs was observed in the pseudogap phase for doping levels in the interval $0.09 \leq p \leq 0.16$ [6], that means in underdoped to optimally doped cuprates and since their discovery it was supposed that CDWs and superconductivity were two orders in competition among each other. The doping interval in which CDWs arise corresponds exactly to the plateau in the superconductivity dome an their onset temperature T_{CDW} reaches its maximum in the centre of this region, as shown in Fig.(4.6a). This is approximately the same doping level at which the quasi-elastic peak in RIXS spectra is most intense. On the other hand if we follows what happens to the peak intensity as a function of temperature, we would find the evolution of Fig.(4.6b) (black datapoints) [10]. The intensity increases smoothly as the temperature drops until reaching a maximum at $T = T_c$; here the CDW signals is quenched as if superconductivity destroyed the long-range charge order. However if a magnetic field is applied to the material (green, blue and red datapoints show increasing levels of the field), the curves continue raising below T_c and then flatten. The presence of a magnetic field seems to stabilize the CDW order while other experiments also reported a quenching of superconductivity and reduction of T_c upon application of magnetic fields. All of these behaviours suggest a competition between the two ordering phenomena, that should be investigated further. In particular stripes in the 214 family and CDWs in the 123 family were observed in the underdoped region within the pseudogap phase and they may be intimately related to it. However, although the definition of T^* is not shared by all the community, it is relevant to notice that $T_{CDW} < T^*$ everywhere thus suggesting that CDWs are an instability inside the pseudogap [6]. Another important question is related to what happens to charge order and the pseudogap within the superconducting dome and going to $T = 0\,\mathrm{K}$. One hypothesis is the presence of a quantum critical point, but this is still much debated and this region of the phase diagram, near optimal doping, should be investigated further.

4.2 Magnetism in cuprates

As already outlined in the previous section magnetism is one of the widest and most inspected theme in cuprate literature, because of the several unusual phenomena that have been observed in these kind of systems. First of all parent compounds of cuprate families possess a strict antiferromagnetic order that involves the CuO_2 planes. The long-range spin correlations are progressively weakened by hole doping determining the onset of unusual arrangements of the spins that have been interpreted in many ways according to their properties. The big effort in studying these magnetic phenomena arises from the fact that many scientists believe that they are intimately connected with the pairing mechanism originating high-T_c superconductivity. The most widespread experimental techniques for studying magnetism in cuprates are elastic and inelastic neutron scattering, which have been used to study thoroughly antiferromagnetic correlations in many regions of the phase diagram [28, 60]. However also other techniques as RIXS have been applied and demonstrated to be really useful in the study of magnetic excitations in cuprates [54]. Most of the experimental measurements have concentrated on the inspection of magnetic correlations in the undoped to optimally doped region as here spin fluctuations were observed and many phenomena, as the formation of stripe order, occur that are believed of fundamental importance for the understanding of high-T_c superconductivity mechanisms. All of these phenomena mainly involve the CuO_2 planes and the materials are often described in terms of 2D systems. However we should not forget that cuprates are 3D systems and an inter-plane coupling is also present. Along the c-axis (perpendicular to the CuO_2 planes) a weak ferromagnetism develops due to Dzyaloshinsky-Moriya interaction which is relevant in cuprate/ferromagnet heterostructures [18, 9] as long as in bulk cuprates [17]. This ferromagnetic order can be effectively studied with X-ray magnetic circular dichroism which is the technique we employed in the experiment described in next chapter.

3D Antiferromagnetic order

Before extending the discussion to the truly 3D layer structure of cuprates we start considering how antiferromagnetic order develops within CuO_2 planes. Fig(4.7a) is a pictorial representation highlighting the different lattice subunits that can be identified in a single plane. The solid red line specifies the CuO plaquette we have already described in the previous section, which calls to mind the perovskite structure where each Cu ion is bonded to four oxygen atoms. The addition of two apical oxygens determines the creation of the typical octahedra visible in the 3D structure of $La_{2-x}Sr_xCuO_4$ (see Fig.(4.2b)). The chemical unit cell of the 2D lattice is the one highlighted in green and clearly shows that the basic building block of the structure contains one copper and two oxygen atoms. However if we consider the spin arrangement, which exhibits a strong antiferromagnetic order, the unit cell has to be doubled and becomes the grey one. When working with diffraction it is more convenient to think in terms of the reciprocal lattice, which is drawn in Panel (b). The circles locate the positions of Bragg peaks corresponding to the chemical structure. The dashed line encloses

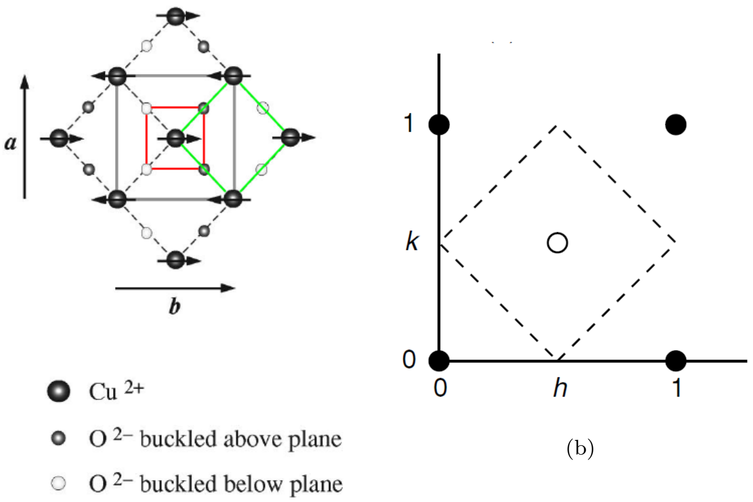

(a)

(b)

Figure 4.7: (a) Schematic representation of a CuO_2 plane, comprising the unpaired electron spins on the Cu atoms. The red line highlights the squared plaquette which is part of an octahedron. The green line specifies the chemical unit cell and the grey solid line the magnetic unit cell, which is twice the chemical one. Re-elaborated version of figure taken from [35]. (b) Reciprocal lattice of a CuO_2 plane. The dashed line shows the magnetic fist Brillouin zone. Taken from [60].

the antiferromagnetic first Brillouin zone and the central open circle identifies the magnetic Bragg peak $\mathbf{q}_{AF} = (1/2, 1/2)$. This point is one of the most important for the study of magnetism with neutron diffraction as the destruction of long-range spin correlations was identified by observing an intensity suppression of this peak.

2D antiferromagnetic order is determined by superexchange interaction mediated by the oxygens surrounding the Cu ions. The exchange interaction originates directly from the antisymmetric nature of the electronic wave function and can be espressed as an effective Hamiltonian involving two spins [7]:

$$\hat{H}^{spin} = -2J\mathbf{S_1} \cdot \mathbf{S_2} \tag{4.1}$$

where the *exchange constant* J represents the energy necessary for reversing a single spin. The sign of J determines if either ferromagnetic or antiferromagnetic order is favoured. Direct exchange is usually effective when there is large overlap among the neighbouring magnetic orbitals, which is not the case for oxides of $3d$ metals as copper. In these materials the exchange interaction is mediated by the non magnetic oxygen ions and takes the name of *superexchange*. Antiferromagnetic coupling is favoured because it determines a kinetic energy gain by delocalizing the magnetic electrons. Describing the system with a single band Hubbard model the exchange coupling is given by $J = 4t/U$ where t is the hopping matrix element and U is the Coulomb repulsion of two electrons on the same site [7, 60]. In parent compounds high values of J were founds; as an example it was determined $J = 146\,\mathrm{meV}$ for La_2CuO_4 and $J = 106\,\mathrm{meV}$ for $YBa_2Cu_3O_{6.1}$ meaning that the AF order is strong [60]. The Néel temperature T_N of the most common compounds varies between 250 K and 540 K, but it is also affected by impurities that reduce it. The same holds true for the value of the ordered magnetic moment m_{Cu} that differs from the ideal Heisenberg ferromagnet with $m_S = 1\mu_B$, given that $S = 1/2$. The value found is smaller, included in the range $0.3 - 0.6\mu_B$. Some reasons for this reduction are the presence of impurities and covalency effects generated by the hybridized orbitals between copper and oxygen in the CuO_2 planes [28].

We are now ready to extend the discussion of antiferromagnetic order to the real 3D structure. As an example Fig.(4.8a) shows the chemical unit cell of La_2CuO_4 in which some important elements have been highlighted: the central octahedron, the spin antiferromagnetic orientation in CuO_2 planes and the three main crystallographic directions. The one shown is the unit cell of the tetragonal phase of La_2CuO_4 which however upon cooling undergoes a transition to an orthorhombic structure. This is characterized by an alternate tilting of around 4° of the CuO_6 octahedra, about the diagonal axis of the tetragonal cell. A picture of how the new structure looks like is displayed by Fig.(4.8b). The orthorhombic unit cell is doubled with respect to the tetragonal one and, considering the 2D cell within the CuO_2 planes, coincides with the magnetic unit cell. The structural transition occurs at 530 K and represents a problem from the point of view of sample growth because, as there are two equivalent tilting directions (the two diagonals of the tetragonal cell), the crystal is usually twinned. A possible solution is to apply a directional stress while cooling, determining the formation of a single domain [33]. It is important and useful to point out that in La_2CuO_4 consecutive CuO_2 planes are staggered so that if we consider a magnetic ion, we do not find other spins directly on its vertical in the two neighbouring planes. In $YBa_2Cu_3O_{6+x}$ the situation is slightly different as each unit cell contains a bilayer of CuO_2 planes antiferromagnetically coupled and they stack one upon the other

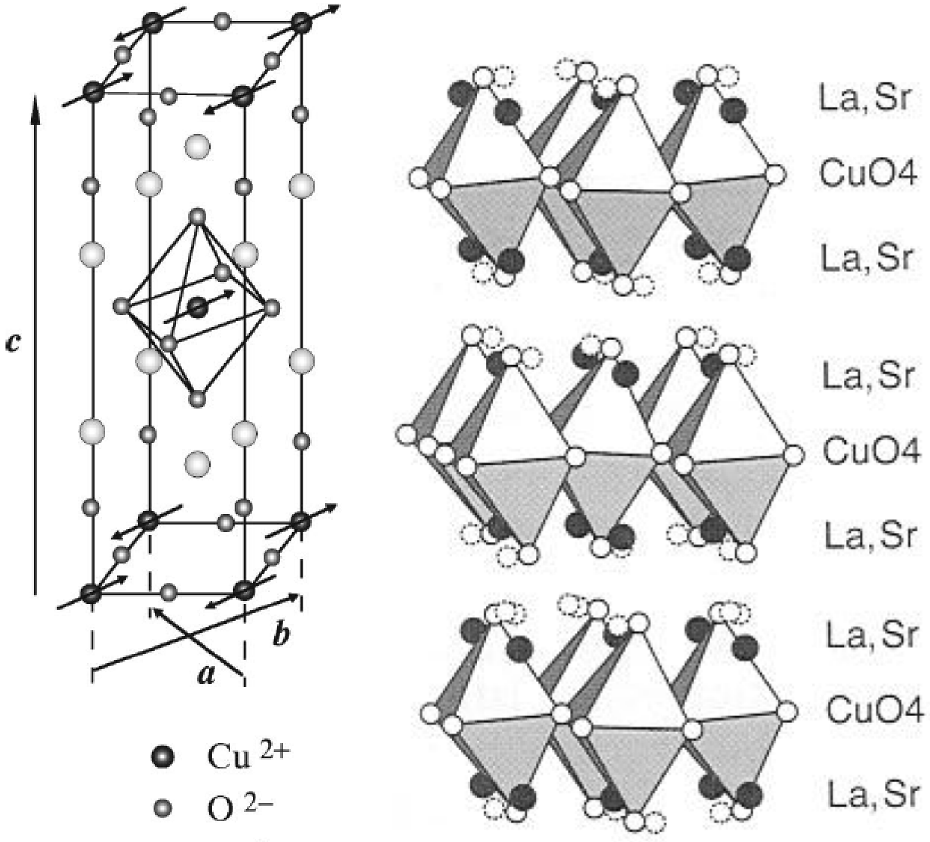

(b)

(a)

Figure 4.8: (a) Unit cell of La_2CuO_4 evidencing the 3D antiferromagnetic order of the parent compound. Taken from [35]. (b) Pictorial representation of the orthorhombic structure of La_2CuO_4, characterised by the tilting of the CuO_6 octahedra. Taken from [43].

separated by one layer of CuO chains. So Cu1 and Cu2 atoms are all vertically aligned along the *c*-axis (refer to Fig.(4.2c)). The antiferromagnetic coupling between consecutive CuO_2 layers is in general weaker than in the plane; indeed in La_2CuO_4 no direct exchange interaction is present due to the small overlap of the magnetic orbitals and there is no oxygen bonding to mediate superexchange. Moreover, because of the staggered structure of the atoms, each spin sees as its nearest neighbours in the consecutive plane two couples of moments with opposite direction; hence the magnetic coupling should cancel out exactly if not for the buckling due to the tilting of octahedra that slightly modifies the local inter-plane distance. This results in a weak correlation of the magnetic moments on a distance only up to two or three CuO_2 layers. The situation notably differs for $YBa_2Cu_3O_6$ [58] where the two CuO_2 planes in a bilayer are distant only 3.3 Å

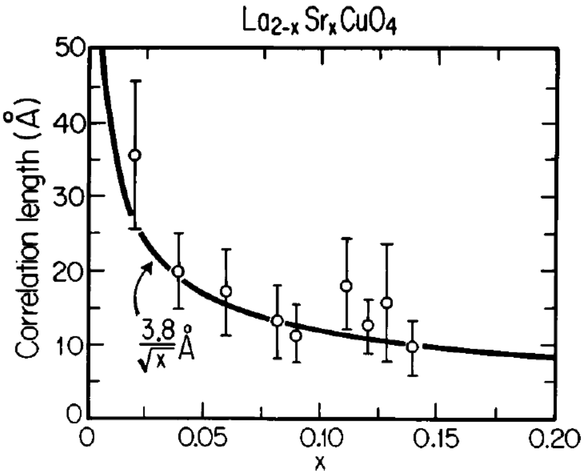

Figure 4.9: Doping dependence of the spin correlation length ξ in LSCO. Taken from [57].

accounting for direct dipolar interaction. Between non neighbouring layers coupling is instead determined by superexchange mediated by the non magnetic Cu1 atoms. The inter-plane coupling constant in this material is about one hundred times larger than for LSCO but it is still weaker than in-plane correlations.

As briefly mentioned above, the long-range antiferromagnetic phase is rapidly destroyed upon doping leaving short-range correlations that can further develop in different sorts of static arrangements as for example stripes. In LSCO this phenomenon evolves very quickly with doping and the Néel antiferromagnetic state shows a fast decreasing T_N [34] and already disappears with $x \simeq 0.02$. Adding holes, that compensate the unpaired spins in Cu2 outer shell, means diluting the magnetic long-range order, but the decrease is too effective to be explained by dilution only, as in similar systems it takes one order of magnitude more doping to destroy the Néel phase. Some have suggested that adding a hole determines the onset of a frustrated state [33] because the new spin, lying on an oxygen atom has the same magnetic coupling to its two nearest-neighbouring coppers which however have opposite directions. Neutron scattering studies of very lightly doped cuprates ($x \leq 0.02$) have revealed the onset of an incommensurate order for $T < 30\,\mathrm{K}$ [39] and anomalous reduction of the magnetic Bragg peak, meaning a sudden deterioration of antiferromagnetism. This observation seems in continuity with the observed *spin glass* phase in the doping range $0.02 \leq x \leq 0.055$ where a diagonal stripe pattern was observed. In particular in the region $x \leq 0.02$ the onset temperature is about constant and the estimated volume fraction of the stripe order is linear in the doping x. Thus Matsuda and coworkers have interpreted their observations [39] as the evidence of an electronic phase separation. As holes are added through doping, they tend to separate into finite regions with either stripe order and local doping $x = 0.02$ or keeping antiferromagnetic order and $x = 0$. The degeneration of long-range antiferromagnetic order is also reflected by the doping dependence of the spin correlation length ξ, which is depicted in Fig.(4.9) [57]. This represents how ξ evolves with doping of $La_{2-x}Sr_xCuO_4$ at low temperature. Of course, by increasing temperature, ξ tends to go to zero because of thermal agitation, but in the limit of low temperature it reaches a finite value which gets higher as doping decreases. The solid line represents the average separation between the holes and well fits the datapoints except for $x \lesssim 0.02$ where ξ diverges as the 3D AF order is established. A similar picture is also valid for $YBa_2Cu_3O_{6+x}$ where however things are complicated by a structural transition. As already explained YBCO has one tetragonal and many orthorhombic phases according to temperature and doping. The tetragonal to orthorhombic-II transition occurs at $x \simeq$0.3-0.4 that is the same level at which AF order is suppressed. Furthermore the structural rearrangement determines a jump in the hole density in the CuO_2 planes. By increasing the doping further the material becomes superconducting and spin correlations remain short-range involving only a few cells [60].

Weak Ferromagnetism

As CuO_2 planes inside cuprates can be considered almost ideal Heisenberg antiferromagnets the total spin Hamiltonian describing their magnetic properties can be written by summing contributions of the form (4.1) for all the couples of nearest-neighbouring spins, which yields the so-called Heisenberg model [7]. However if we are interested in studying the real system other contributions have to be taken into account; in particular the sum should extend also to the nearest-neighbours between consecutive CuO_2 layers. Furthermore the structural tilting of the octahedra introduces an additional antisymmetric exchange term called Dzyaloshinsky-Moriya (DM) interaction. In a similar way as oxygen acts in superexchange, spin-orbit coupling mediates an interaction between the ground and the excited states of two neighbouring magnetic ions. Taking the anisotropic terms into account the exchange constant becomes a second rank tensor **J** rather than a scalar and the spin Hamiltonian can be expressed as [55]:

$$H = \sum_{\langle i,j \rangle} \mathbf{S}_i \cdot \bar{\bar{\mathbf{J}}} \cdot \mathbf{S}_j \tag{4.2}$$

The off-diagonal components account for the Dzyaloshinsky-Moriya anisotropy term that, in its basic form is written as [25]:

$$H_{DM} = \sum_{\langle i,j \rangle} \mathbf{d} \cdot (\mathbf{S}_i \times \mathbf{S}_j) \tag{4.3}$$

where **d** is the DM vector, whose direction depends on the crystal field and on the symmetry of the structure. In the case of La_2CuO_4 the presence of this term is brought about by the buckling of CuO_2 planes, which breaks the inversion symmetry of the system so that oxygen atoms are no longer aligned with the copper atoms they connect. Referring to Fig.(4.8) we can imagine **d** as parallel to the *a*-axis of the crystal structure. In order to lower the magnetic energy the couple of spin considered tends to adjust in the plane perpendicular to **d** in a way that their vector product gives a negative energetic contribution when projected along **d**. As a result spins cant slightly out of the CuO_2 plane by 0.17° and therefore each layer possesses a weak ferromagnetic character perpendicularly to the planes, with a net moment of $2 \times 10^{-3} \mu_B$ per Cu2 atom [33]. Without applying an external field ferromagnetism is "hidden" because spins in consecutive layers cant in the opposite direction, due to the small interlayer coupling. However if we apply a field which is strong enough perpendicularly to the planes (along the *c*-axis) we are able to determine the transition to weak ferromagnetism, overcoming the interlayer coupling. An important question which is still open is how the observed weak ferromagnetism behaves with doping and whether this has any relations with the onset of superconductivity. As we already explained for antiferromagnetism in CuO_2 planes, the introduction of additional holes in the material effectively destroys the long-range spin correlation. However short-ranged fluctuations are believed to be still very important in determining the outstanding physical phenomena that appears in cuprates. A very valuable technique to investigate the evolution of weak ferromagnetism as a function of the most relevant parameters (doping, temperature and applied field) is X-ray Magnetic Circular Dichroism which yielded interesting results both on ferromagnet/superconductor junctions [9, 18] and pure cuprates [17]. We considered useful to move the brief review of this topic in the next chapter because it is directly connected with the experiment we carried out and we thought that it could be better understood after a general introduction to the experimental technique.

Chapter 5

XMCD for probing magnetic properties of cuprates

After a general review of the most important properties of cuprates, focusing on the magnetic ones, in this chapter we introduce the experimental technique of X-ray Magnetic Circular Dichroism. The dichroic signal consists in the differential absorption of right and left circularly polarized light by the material subject to an external field and can give some useful information on the magnetic properties of the valence states. Moreover a set of sum rules allows to determine quantitatively with a good accuracy the spin and orbital moments from the XMCD signal. XMCD has been used effectively to study the hidden ferromagnetism in pure cuprate structures and ferromagnet/cuprate interfaces for which we present a brief summary. Following these works we also carried out an XMCD experiment to study the evolution of magnetism in samples of $La_{2-x}Sr_xCuO_4$ and $NdBa_2Cu_3O_{6+x}$ with different dopings. The interest in these measurements was not only justified by the topic but also by the fact that it was the very first experiment on the new ID32 beamline at ESRF and so it was a strict test of all the equipment. The last section of this chapter illustrates the main results we were able to produce.

5.1 XAS and XMCD techniques

An XMCD spectrum is a dichroic signal which is obtained by the difference of the absorption spectra of a magnetized sample measured with left and right circularly polarized light. In this sense XMCD is simply a variation of the general experimental technique of X-ray Absorption Spectroscopy (XAS) [16]. When X-ray photons hit a solid sample they can be scattered inside the material or absorbed for example by exciting a core electron to an empty valence level. By comparing the incident photon intensity with some signals related to the excitation processes inside the material it is possible to generate the absorption spectrum, which gives interesting information on the density of states.

As XAS involves the interaction between radiation and matter its theoretical description starts from the general framework of time-dependent perturbation theory, which can be found in any general text of quantum mechanics, for example [27, 44]. The Hamiltonian describing a set of particles in an electromagnetic field can be written in the following way:

$$H = H_0 + H_{int} \tag{5.1}$$

where H_0 represents the unperturbed system and H_{int} is the perturbation given by the interaction with the electromagnetic field. Considering only the perturbative terms that are first order in the vector potential $\mathbf{A}$ describing the field and neglectic the interaction of the spin with the magnetic component, the perturbation Hamiltonian takes the following form:

$$H_{int} = \frac{e}{mc} \sum_i \mathbf{p}_i \cdot \mathbf{A} \tag{5.2}$$

where i runs over all the electrons. If we suppose that an absorbed photon excites the system from the initial state $|\Psi_i\rangle$ to the final state $|\Psi_f\rangle$ the transition probability per unit time is given by Fermi's Golden Rule:

$$W_{fi} = \frac{2\pi}{\hbar} \left|\langle\Psi_f \left|H_{int}\right| \Psi_i\rangle\right|^2 \delta\left(E_f - E_i - \hbar\omega\right) \tag{5.3}$$

in which the delta function ensure the conservation of energy in the process. If we evaluate W_{fi} by substituting (5.2) into (5.3) and write $\mathbf{A}$ as a plane wave, we obtain an expression of the form

$$W_{fi} \propto \left|\left\langle \Psi_f \left| \sum_j (\mathbf{p}_j \cdot \mathbf{e}) e^{i\mathbf{k}\mathbf{r}_j} \right| \Psi_i \right\rangle\right|^2 \tag{5.4}$$

where $\mathbf{k}$ and $\mathbf{e}$ are the wave vector and polarization of the radiation. In X-ray energy range, $\mathbf{kr}$ is smaller than 10^{-2} and the term $e^{i\mathbf{kr}}$ can be expanded into its Taylor series. It is often sufficient to truncate it to the first term $e^{i\mathbf{kr}} = 1$, which is called the electric dipole approximation. This derives by the fact that with some calculations the transition matrix element can be rearranged into $\langle \Psi_f \left| \mathbf{D} \cdot \mathbf{e} \right| \Psi_i \rangle$ where $\mathbf{D}$ is the magnetic dipole operator. If we keep the next term in the expansion of $e^{i\mathbf{kr}}$ we find the electric quadrupole and magnetic dipole terms and so forth. It is common to use the following notation for the transition operators in the multipolar expansion: E1 for the electric dipole, E2 for the electric quadrupole and M1 for the magnetic dipole and so on. As the relevant experimental parameter is the absorption cross-section, which is given by the transition probability divided by the photon flux and is then proportional to the squared value of the transition matrix element, we find in its final expression both pure (E1E1, E2E2, M1M1) and mixed contributions (E1E2, E1M1, M1M2) [50]. Nevertheless within X-ray energies the most relevant term is the electric dipole because the electric quadrupole and magnetic dipole transitions give a probability which is smaller by 10^{-4}. Not all the possible transitions from an initial $|\Psi_i\rangle$ to a final $|\Psi_f\rangle$ state are permitted because some combinations may cancel the transition element. The allowed transitions are set by the so-called selection rules and for the absorption processes we consider in XAS and XMCD, in dipolar approximation, the only possible transitions are the ones with $\Delta l = \pm 1$, $\Delta s = 0$ and $\Delta m_l = 0, \pm 1$.

XAS measures the entity of the absorption as a function of the incident energy, which is governed by Fermi's Golden Rule; indeed when radiation has the right photon energy, it can be absorbed by the material through a transition. Once the incident radiation energy is equal to the binding energy of a core electron we observe a sharp increase in the absorption which is known as the *absorption edge*. XAS energy scans are performed in proximity of the different edges which take their name according to the core levels that are excited; specifically if we excite electrons with quantum number $n = 1, 2, 3$ we are working at the K, L and M edge respectively. In the systems we are studying, which are $3d$ transition metal oxydes, the most relevant excitations are at the $\mathrm{L}_{2,3}$ edge of copper and at the K edge of oxygen. The main features of these edges respectively identify the transitions $2p \rightarrow 3d$ and $1s \rightarrow 2p$ which are allowed by electric dipole and are hence the most intense. The fact that XAS spectroscopy works on electronic states with a precise binding energy makes it a very powerful technique because

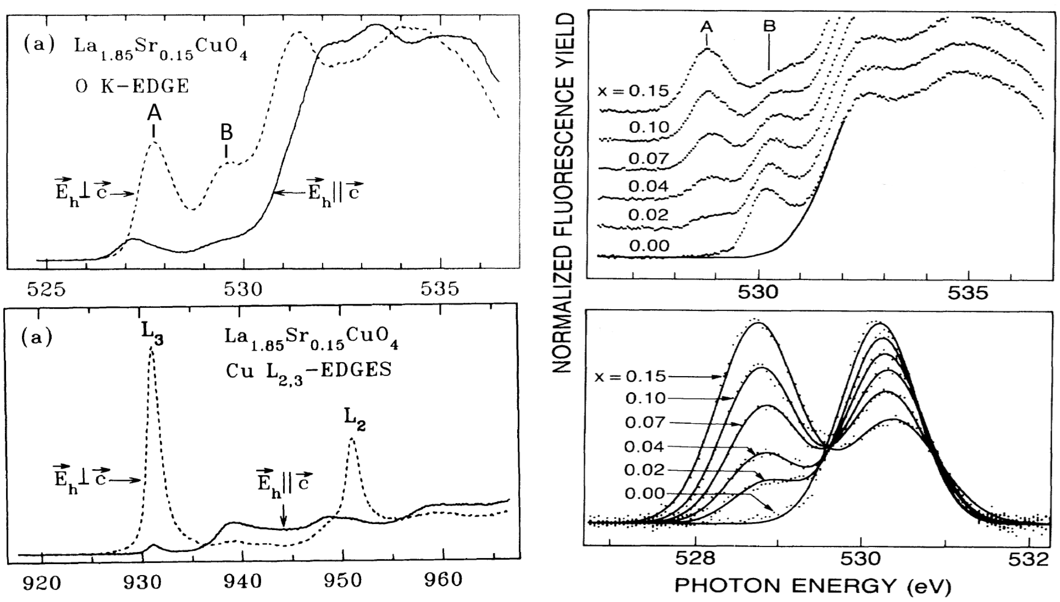

(a) (b)

Figure 5.1: (a) XAS spectra at the O K edge (top) and Cu $L_{2,3}$ edge of optimally doped LSCO (x = 0.15) measured with majority light polarization parallel (solid line) and perpendicular (dashed line) to the c-axis, pointing out the almost totally in-plane $d_{x^2-y^2}$ character of both intrinsinc and doping-induced holes. Taken from [13]. (b) Doping dependence of the O K pre-edge peaks of LSCO: XAS spectra (top) and peaks fitted with two gaussians after the subtraction of the common background (bottom). Re-elaborated image taken from [12].

it allows a certain chemical selectivity. Although being a naïve picture, we can think of radiation absorption as a one-electron process in which a core electron is excited to an empty valence state and the other electrons do not take part in the process. If we suppose that the squared matrix element is almost constant with the energy, XAS is effectively inspecting the density of empty states ρ [16]. This picture well describes the K-edge of oxygen where the XAS is well approximated by the oxygen p-projected density of states whereas poor agreement is found when dealing with $3d$ states of transition metals or $4f$ states of rare earths in case of partly filled final states. In these cases a more sophisticated approach called *Charge Transfer Multiplet* theory [15] can be used.

Absorption spectroscopy has proved to be very useful for the study of high-T_c copper oxide superconductors. In particular it was really important for the determination of the orbital nature of the holes in undoped and doped cuprates. Fig.(5.1a) shows the XAS spectra at the O K edge (top) and Cu L edge (bottom) of a sample of optimally doped LSCO (x = 0.15) [13]. The same measures have been repeated with majority light polarization $\mathbf{E}_h$ parallel (solid line) and perpendicular to the c-axis of the sample. The two peaks (A and B) in the pre-edge of the oxygen and the $L_{2,3}$ peaks of copper are associated with the excitation of $3d$ holes and demonstrate that they have almost pure in-plane $x^2 - y^2$ nature. However the small residual peaks with out-of-plane polarization allowed to quantify about 15% of oxygen $2p_z$ character [13]. The A and B peaks at the oxygen pre-edge are related to doping-induced holes and $3d^9$ holes of the undoped material respectively. The first peak, located at 528.8 eV mainly results from transitions of the type $3d^9\underline{L} \rightarrow \underline{1s}3d^9$ and the second, at 530.3 eV is due to $3d^9 \rightarrow \underline{1s}3d^{10}$ transitions [13]. This is confirmed by the doping dependence of the relative intensity of the two peaks shown in Fig.(5.1b). In the top panel the different XAS of $La_{2-x}Sr_xCuO_4$ samples are plot for increasing doping level x from bottom to top. The pre-edge region is zoomed in the bottom panel, where the common background has been subtracted and the peaks have been fitted with two gaussian lineshapes. It is clear that raising the doping level brings about a suppression of the B peak and an enhancement of the A peak which is already higher than B at $x = 0.10$.

Basics of XMCD

In order to introduce the XMCD method we would like to start by giving a brief explanation of its name. Circular dichroism refers to the property of some materials of absorbing differently right and left circularly polarized radiation. This effect could be due to intrinsic properties of the system connected with the relative orientation of the light helicity and symmetry or chiral axes, or it can be brought about by the application of a strong magnetic field parallel to the direction of light propagation, which orients the magnetic moments inside the sample. This phenomenon is quantified by the XMCD spectrum $\Delta\mu$ which is defined as the difference of the XAS spectra measured with right (μ_R) and left circularly polarized light (μ_L):

$$\Delta\mu = \mu_R(\mathbf{B}) - \mu_L(\mathbf{B}) \tag{5.5}$$

The magnetic field $\mathbf{B}$ is oriented parallel and opposite to the direction of propagation of the light, as this is the arrangement that provides the maximum signal. Fig.(5.2) sketches out the essential geometry of an XMCD experiment highlighting the relative directions of magnetic field, light wave vector, magnetization and

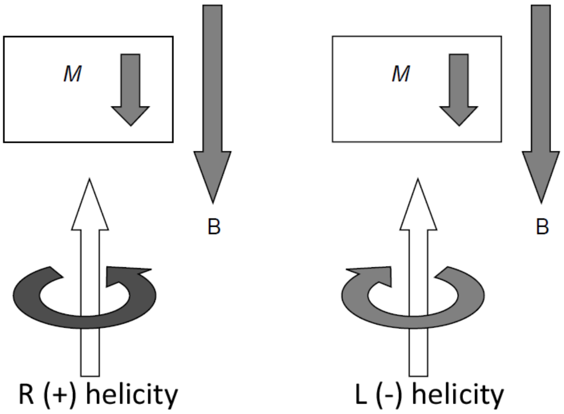

Figure 5.2: Geometry used in an XMCD experiment. The magnetic field is parallel to the direction of light propagation in order to maximize the dichroic effect. Image re-elaborated from [16].

helicity. Sometimes the helicity is labelled with “+” and “-” instead of “R” and “L” and every author uses his own sign convention. If the magnetic field is reversed the sign of the dichroism is inverted as well because what is important in order to generate the dichroic effect is the relative orientation of the helicity and the magnetic field, hence the XMCD spectrum can be also measured by keeping the same helicity but inverting the magnetic field as follows:

$$\Delta\mu = \mu_R(\mathbf{B}) - \mu_R(-\mathbf{B}) \tag{5.6}$$

The origin of the XMCD effect has to be looked for in the different selection rules connected with the polarization of light. Actually the absorbed photon transfers its angular momentum to the excited photoelectron and the dipole selection rule states that $\Delta m_l = 0, \pm 1$ where $+1$ is valid for left circularly polarized light, -1 for right circular polarization and 0 for linear polarization. The presence of the magnetic field splits the electronic levels by Zeeman effect [27] and if we evaluate the relative weights of the allowed transitions by means of Fermi’s golden rule, it is possible to find a helicity dependence of the XAS which gives a non-zero XMCD signal. Wu and Stöhr proposed a simple two-step model to explain the birth of a dichroic signal especially in $3d$ transition metals [52], which is depicted in Fig.(5.3a). We consider the L_3 and L_2 edges of a $3d$ transition metal which results from the $2p_{3/2} \rightarrow 3d$ and $2p_{1/2} \rightarrow 3d$ transitions respectively where the starting core level is split by spin-orbit coupling. The incoming photons carries an angular momentum related to the helicity, that can be partly transferred to the spin of the excited photoelectrons. Right and left circularly polarized radiation photons

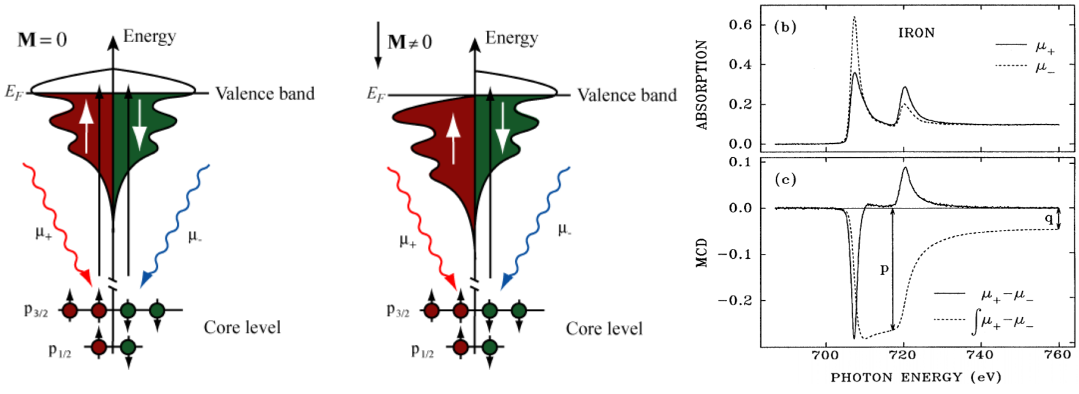

(a)

(b)

Figure 5.3: (a) Two-step model proposed in [52] to explain the onset of the XMCD effect. The presence of a magnetization (right panel) splits the valence band changing the relative number of spin-polarized empty states. This, combined with the matrix elements, determines different transition rates for the two opposite light polarizations. (b) XAS (top) and XMCD (bottom) at the L edge of Fe. In strong ferromagnetic metals the XMCD signal can be around 30% of the XAS. Taken from [11].

transfer the opposite momentum and generate photoelectron populations with opposite spins. This represents the first step of the model, in which the core level can be considered as an atom-specific source of spin-polarized electrons. By evaluating the transition matrix elements it can be formally demonstrated that right circularly polarized light excites 62.5% spin-up and 37.5% spin-down electrons at the L_3 edge whereas at L_2 edge it excites 25% spin-up and 75% spin-down. For left circularly polarized light the above percentage values are inverted. It is interesting to note that with equal light polarization, the two edges have opposite spin polarization, because of the opposite spin-orbit coupling. The second step of the model is the absorption of the photoelectrons by the $3d$ valence band which acts as a spin-resolved detector. If the valence band is not spin-split, meaning that there is no magnetization (diagram on the left in figure), the sum of the transition intensities of spin-up and spin-down electrons is the same for the two light polarizations and no XMCD signal is evidenced. On the contrary if we apply a magnetic field for example to a ferromagnetic sample, the valence band is spin-split (diagram on the right in figure), according to the Stoner model [7]. As a consequence of this, there is a majority and a minority spin orientation with a relative imbalance in the density of empty states that favours the absorption of electrons with a certain spin polarization. As the two helicities excite a different number of spin-up and spin-down electrons the absorbed intensities are different giving rise to an XMCD signal as the one shown in the bottom panel of Fig.(5.3b). The described picture, based on Stoner model, is valid for $3d$ metals, whereas for their ions and coordinated systems an atomic picture is more appropriate, in which all the single transitions are considered. However the results are analogous to the ones explained and an example of the XMCD evaluation based on the transition probabilities for Cu^{2+} ions can be found in [16]. Anyway the XMCD signal is the result of the combination of two factors which are the transition matrix elements and the number of empty states, which together give the transition rate. When there is an imbalance in the transition rates for left and right circularly polarized light the XMCD effect occurs. Fig.(5.3b) shows as an example the XMCD signal of the $L_{2,3}$ edge of Fe [11]. The top panel displays the XAS spectra with the two opposite polarizations and the presence of a strong dichroism is visible naked-eye. The dichroic signal is plotted in the bottom panel and we can notice the opposite sign of the two edges. Fe, as well as other strong ferromagnets, gives a huge XMCD signal, which is around 30% of the XAS. In the systems we are interested in for studying weak ferromagnetism, we have instead to deal with signals that are less than 1% of the XAS. One of the main strong points of XMCD is its chemical and orbital selectivity, that allows to study the magnetic properties of the sample from the point of view of a specific element. However XMCD is even more powerful because it can give also quantitative information on the atomic spin and orbital moments of the ground state through the use of *sum rules* [56, 8]. These apply to the $L_2, 3$ edges of $3d$ transition metals and allow to estimate the expectation values of the orbital moment $\langle L_z \rangle$ and spin moment $\langle S_z \rangle$, where the axis of quantization z is parallel to the wave-vector of incident photons and to the direction of magnetization in our simple geometry.

Regarding the experimental detection of XAS and XMCD signals, three main methods are used: transmission detection, total electron yield and fluorescence yield. *Transmission detection* is capable of measuring directly the absorption coefficient of the material as it probes the radiation intensity before and after having passed through the sample. The main disadvantage of this technique is that it requires very thin samples (with thickness of the order of some microns) with a high degree of homogeneity, otherwise non-linear thickness effects can occur modifying the spectral shape. *Total Electron Yield* (TEY) does not measure absorption directly, but rather all the electrons that are emitted by the material in consequence of it. These can be roughly divided into photoelectrons and Auger electrons, which themselves generate a cascade of secondary electrons. As electrons interact with matter much more than X-rays their escape depth is of the order of a few nanometres, thus TEY is sensitive to the surface of the sample. The measure can be done for example by connecting the sample to ground and measuring the emitted current with a picoammeter. This method could give problems with insulating samples as the emitted electrons cannot be replaced and they are getting more and more charged. The last detection method is *Fluorescence Yield* (FY) which measures the photons emitted by the fluorescent decay of the core holes. Differently from TEY, fluorescence yield is bulk-sensitive, but works well only for diluted samples. Too dense samples indeed undergo the process of self-absorption that lowers the apparent absorption coefficient. Moreover the FY signal is usually smaller than the TEY, also because it is often acquired through a photodiode that sees only a small part of the solid angle of emission, and hence it is more sensitive to noise.

Weak ferromagnetism studied by XMCD

As explained in depth in the previous chapter, Dzyaloshinsky-Moriya interaction is responsible for the “hidden” weak ferromagnetism in cuprates, which can be successfully inspected with XMCD. Anisotropic exchange interaction determines a small canting ($\simeq 0.17^\circ$) of the spin moments towards the *c*-axis giving a small ferromagnetic component in this direction. The ferromagnetic order is however “hidden” by the AF coupling of consecutive CuO_2 planes, but, if we apply a magnetic field sufficiently strong to overcome the inter-layer exchange, we can induce a spin-flop transition that orientates the small spin components and gives rise to the phenomenon of weak ferromagnetism [47]. It is important to notice that the magnetic canting of the spins cannot be explained in terms of a paramagnetic effect as it would require a much higher magnetic field in these materials. An interesting question is how the weak ferromagnetic order evolves with doping in $La_{2-x}Sr_xCuO_4$ and if it can be also found in other families of cuprates. Recently De Luca *et al.* [17] carried out an extensive XMCD study of weak ferromagnetism in undoped La_2CuO_4 and underdoped to optimally doped LSCO and YBCO and interestingly found out that weak ferromagnetism persists even up to optimal doping. In particular, by the application of the sum rules, it was

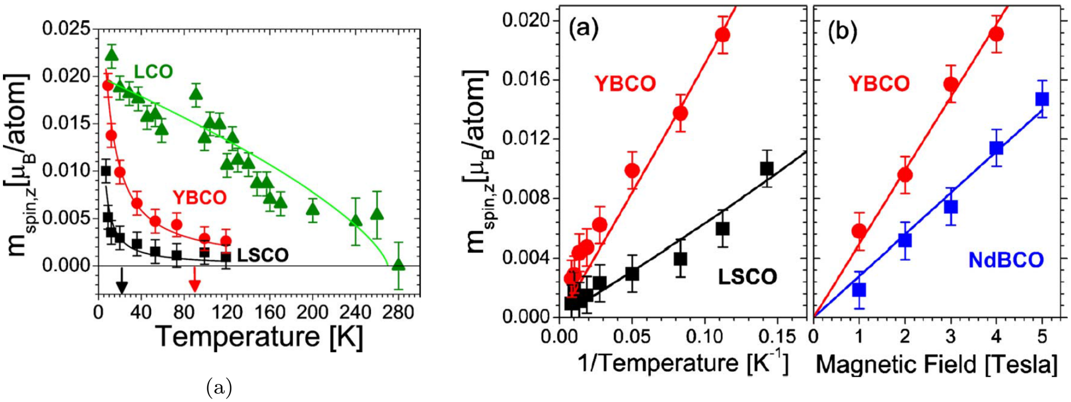

(a)

(b)

Figure 5.4: (a) Temperature dependence of the spin magnetic moment $m_{spin,z}$ of LCO, optimally doped YBCO and underdoped LSCO, evaluated from XMCD at 4 T. The arrows indicate the critical temperatures of the superconducting samples. (b) Evidence of paramagnetic behaviour of the weak magnetism due to the Dzyaloshinsky-Moriya interaction in doped samples. Both images are taken from [17].

possible to evaluate the spin magnetic moment $m_{spin,z}$ and follow its evolution as a function of applied field and temperature. Fig(5.4a) shows the temperature dependence of $m_{spin,z}$ for the undoped parent compound LCO, for underdoped LSCO and for optimally doped YBCO, with an applied magnetic field of 4 T. The different behaviour of the undoped sample is evident. LCO shows the typical trend of weak ferromagnetism in antiferromagnetic systems. Indeed LCO possesses an overall 3D antiferromagnetic order and the strong magnetic field overcome the interlayer coupling generating a weak ferromagnetic order along the *c*-axis. As temperature increases the magnetic moment reduces and goes to zero near the Néel temperature of the antiferromagnet ($\simeq 250$ K). The doped systems instead show an iperbolic behaviour and the magnetic moment goes below the sensitivity limit around 130 K for both samples. Interestingly there is no change in behaviour at the critical temperature T_c, signalled by the arrows in the graph. The left plot in Fig.(5.4b) shows that in the superconducting samples the magnetic moment grows linearly with the inverse of the temperature as in a paramagnet. This suggests that doping destroys the inter-layer antiferromagnetic coupling of the CuO_2 planes and the direction of the magnetic moments is decided by the competition between the thermal fluctuations and the external field as in a paramagnet. At low temperatures the magnetic moments are aligned by the field but the order is progressively destroyed by thermal agitation. A further confirmation of this view emerges from the right panel of the same figure,

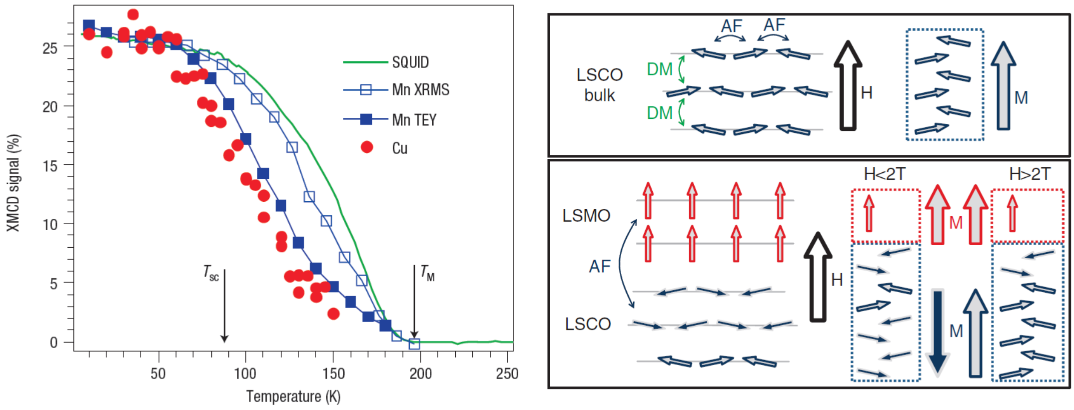

(a) (b)

Figure 5.5: (a) Temperature dependence of the XMCD signal of Cu and Mn in a YBCO/LCMO heterostructure. For comparison the green line is the bulk magnetization measured by a SQUID. Taken from [9].(b) Schematic representation of the spin orientation in bulk LSCO (top) and at a LSMO/LSCO interface (bottom) in the absence (left) and presence (right) of an applied external field. Taken from [17].

which shows the net magnetic moment as a function of the applied field at low temperature (9 K). The trend is linear with no remanent magnetization at zero field. It is important to highlight the fact that the magnetic moments, which were evaluated with the sum rules, are ten times bigger than the reference value for LCO given in [33], but the difference can be due to covalency effects in the Cu-O bond which were not taken into account in the calculations. As a consequence the estimated canting angle is 1.2-1.7° instead than the literature value, which is $\simeq 0.17°$.

Besides bulk cuprates, XMCD has been also employed to study the magnetization profile at the interface between a ferromagnet and a superconductor. The typical systems are cuprate/manganite heterostructures in which the ferromagnet layer is usually constituted by $La_{1/3}Ca_{2/3}MnO_3$ (LCMO) or $La_{1/3}Sr_{2/3}MnO_3$ (LSMO). An $YBa_2Cu_3O_7$/LCMO multilayer was the first system in which an XMCD signal was found also at optimal doping [9]. The magnitude of the signal and evaluated spin moment at low temperature is close to the one calculated in [17], suggesting the same physical origin, but the temperature behaviour, shown in Fig.(5.5a), is totally different. The XMCD signal at the $L_{2,3}$ edge of Mn in the manganite (solid blue squares) exhibits the typical ferromagnetic behaviour going to zero at T_M which is the temperature of the ferromagnetic-paramagnetic transition. Moreover the XMCD signal of Cu (red circles) closely follows the same behaviour. The XMCD of Cu has been rescaled to the Mn dichroism in order to plot them on the same figure; actually the Mn signal is of the order of 27% of the XAS peak, which is a high value typical of ferromagnets, whereas the Cu signal is around 1.4%. The XMCD L_3 peaks of Mn and Cu are also opposite in sign, indicating an antiparallel orientation of the magnetic moments. The XMCD signals, acquired with TEY detection, are slightly quenched with respect to the total bulk magnetization of the sample measured with a SQUID (green line). The temperature dependence of the multilayer is very different from the bulk cuprate of Fig.(5.4). In this case there is no strong external field and the spin orientation is given by the interaction of the canted spins of Cu with the ferromagnetic manganite. It seems that the ferromagnet works as an exchange bias pinning the magnetization inside the cuprate. The strong antiferromagnetic coupling at the interface was believed to be due to the linear Mn-O-Cu bond connecting the two layers, although a recent study demonstrated that cuprate/manganite heterostructures develop weak ferromagnetism even in the absence of this direct link [18]. The previous observations on YBCO/LCMO were extended to an LSMO/LSCO structure where also the field dependence of the magnetization profile perpendicularly to the CuO_2 planes was studied. The two different behaviours evidenced for bulk LSCO and for LSMO/LSCO are depicted in Fig.(5.5b). As already explained, in bulk LSCO magnetization has zero mean value because spins in consecutive CuO_2 planes have opposite canting. However if a magnetic field is applied, they align ferromagnetically. On the other hand at cuprate/manganite interfaces the ferromagnetic layer acts as an exchange bias on the first two CuO_2 planes which align antiparallel to it. The overall sign of the weak ferromagentism is determined by the relative strength of the antiparallel coupling of the first layers and the applied external field. If the latter is less than 2 T the overall magnetization is opposite with respect to the manganite and to the field; if it is greater than 2 T moments orient parallel to it except the two layers closer to the interface, which remain antiferromagnetically pinned. This perturbation of the magnetization profile involves around 10-15 stacked CuO_2 planes and is thought to be due to the transfer of spin-polarised electrons from the manganite to the cuprate at the interface. This process is also considered responsible of the so-called proximity effect, which determines the suppression of the critical temperature of materials in a strong magnetic field.

5.2 First XMCD experiment at ID32

We present in this section the results of an XMCD experiment we carried out in November 2014 at the ID32 beamline of the ESRF. ID32 is the new soft X-rays beamline of the facility and our experiment was the very first one, thus it was also the first test of all the equipment in a real experimental situation. We measured the XMCD spectra of several samples of $La_{2-x}Sr_xCuO_4$ and $NdBa_2Cu_3O_{6+x}$ with different doping levels. We carried out a field dependence of the signal for LSCO and explored some temperature behaviour in NBCO both in high (8 T) and zero field (0.03 T). All the XMCD spectra of NBCO were measured both at the Cu L_3 edge and at the O K edge, which is to our knowledge the first time it was measured on high-T_c cuprates. As a first experiment it was a very strict test for the beamline, as the XMCD signals were very small with respect to the XAS spectrum and this allowed us to point out some energy jitters and non-linearities of the instrumentation that could be of valuable importance for a further improvement of the beamline. In the next we give a brief description of the equipment, materials and methods we used and finally summarize the most relevant results we obtained.

The XMCD branch at ID32

A general description of the ID32 beamline was presented in Chapter 1 when introducing the RIXS instrumentation. Here we give some additional information specific of the XMCD branch. The three APPLE II undulators can provide 100% left and right circularly polarized light which is necessary for XMCD measurements. The monochromator, placed inside the optic hutch, is constituted by a VLS grating with a sagittally refocusing mirror and the spot size on the sample can be adjusted from a FWHM of $1 \times 1\,\mathrm{mm}^2$ to $10 \times 100\,\mu\mathrm{m}^2$ (the first dimension is the vertical and the second the horizontal one). The XMCD experimental chamber is represented by a huge cylinder containing the superconducting magnet sketched in Fig.(5.6). It can supply a magnetic field of up to 9 T along the beam and 4 T perpendicularly to the beam and the field can be ramped relatively fast (less than 2 minutes). The samples are mounted on a manipulator that can rotate by 360° and the sample temperature can be tuned between 6 K and 400 K. Cooling is obtained through an external liquid nitrogen can and an inner liquid

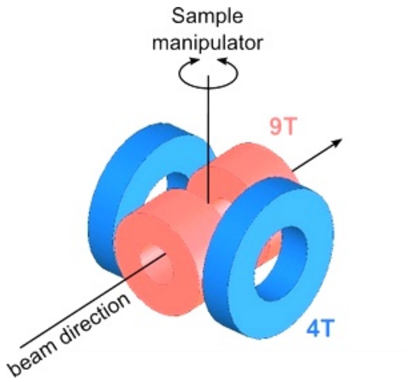

Figure 5.6: Superconducting magnet of the XMCD beamline ID32 at the ESRF. Taken from [3].

helium one. Everything is kept in UHV at around 10^{-10} mbar. Moreover up to three sample holders can be stored in vacuum ready to be swapped. The magnet chamber is integrated with an all-in-vacuum facility for sample preparation and characterization that is equipped with STM, LEED, e-beam and molecular evaporators.

Materials and methods

During the experiment we carried out XMCD measurements of cuprate films with different doping levels. We considered three $NdBa_2Cu_3O_{6+x}$ films grown on a strontium titanate ($SrTiO_3$) substrate: the first one was the antiferromagnetic undoped parent compound, the second was an underdoped sample with $T_c = 50\,K$ and the third was an optimally doped sample with $T_c = 90\,K$. The two doped samples had already exhibited in previous experiments the presence of charge density waves although more stable and stronger in the underdoped. On the contrary the undoped had not shown any evidence of charge ordering. The three samples were studied at $T = 10\,K, 50\,K, 90\,K$ and $300\,K$, and with high ($\pm 8\,T$) and very low ($\pm 0.03\,T$) magnetic field along the beam direction. The low field measures were done to check for a possible remanent magnetization. At 10 K we also measured two films of $La_{2-x}Sr_xCuO_4$: an optimally doped sample ($x = 0.15$ and $T_c = 30\,K$) and an underdoped one ($x = 0.05$), which was insulating; for the LSCO samples we also carried out a magnetic field dependence. All the samples were mounted on the holder which was rotated in order to bring the c-axis almost parallel to the beam direction. For the samples we measured both the copper L_3-edge and the oxygen K-edge, which are dominated by the dipole-allowed transitions $2p \rightarrow 3d$ and $1s \rightarrow 2p$ respectively. These are the most relevant in the XMCD spectrum which is determined by the E1E1 and E2E2 terms of the transition probability [50, 16]. In ideal conditions only two XAS measures are necessary to get an XMCD spectrum: one with right and the other with left circularly polarized light (or one with positive and the other with negative field, using the same polarization). However in real conditions there could be some temporal drifts among the measures or some dependence on field direction and polarization. In order to compensate for linear drifts each XMCD spectrum was acquired following the protocol of Tab.(5.1). For each XMCD spectrum a sequence of 32 XAS was acquired, 16 with positive field and 16 with negative field, switching the polarization according to the sign sequence in table. This was designed in order to compensate for temporal drifts and field dependence but a higher number of acquisitions was also useful to reduce statistical noise in the signal. The XAS have to be combined as follows to generate the XMCD signal:

Field	**Light polarization**															
+	+	+	+	+	-	-	-	-	-	-	-	-	+	+	+	+
-	+	+	+	+	-	-	-	-	-	-	-	-	+	+	+	+

Table 5.1: Experimental protocol used during the measurements. For each XMCD spectrum we measured 32 XAS.

$$\Delta\mu = \frac{\sum \mu_+(+\mathbf{B}) - \sum \mu_-(+\mathbf{B}) - \sum \mu_+(-\mathbf{B}) + \sum \mu_-(-\mathbf{B})}{32} = \frac{\sum f \cdot p \cdot \mu_p(f \cdot \mathbf{B})}{32} \tag{5.7}$$

where $f, p = \pm 1$ are the signs of magnetic field and polarization. For all the measures TEY and FY signals were acquired simultaneously, but only TEY was capable of giving good results, because the fluorescence signal, although qualitatively resembling the TEY, was too small and noisy to be useful in the data analysis. This however prevented us to get reliable results in some spectra of the undoped NBCO sample as, being insulating, gave some charging problems with TEY. Although it was the first experiment on the beamline and commissioning was not complete, the quality of the data was excellent, with negligible electronic noise. The main issues we ran into were instead some energy jitter and drifts and a residual non linearity in the measurement of the incoming beam intensity I_0. The energy drifts affected both the energy scale and the intensity scale of the spectrum but it was possible to correct them almost perfectly with the data processing. First the XAS spectra were aligned horizontally applying a shift that was calculated by maximizing the cross-correlation of the derivative with a reference spectrum. Then the intensities also had to be rescaled in the following way: at first the pre-edge was set equal applying a gain and then a linear offset was subtracted in order to level the opposite side of the spectrum. The values of the gain and of the offset slope were not evaluated by matching single datapoints but optimizing it with linear least squares method over a broad region of the spectrum. On the contrary we were not able to solve the problem of the residual non-linearity of the I_0, that was sensitive to both the photon polarization and the sign of the magnetic field. The non-linearity introduced some artificial residual signals we were not able to get rid of. In XMCD measurements at the copper edge this was smaller than the true signal but set the sensitivity threshold of the system.

Experimental results

We summarize here the main results we obtained from the experiment. On the basis of the literature we were expecting the doped samples to show an XMCD signal at the Cu L_3 edge and this signal to be stronger at low temperature and higher field. Fig.(5.7a) shows the L_3 XAS peaks and relative XMCD signals for the four doped samples (underdoped and optimally doped LSCO and NBCO) measured at 10 K in an 8 T field. Intensities have been rescaled to the XAS peak, and the relative XMCD signals have been zoomed in by 100 times to put them on the same plot (The XMCD scale is the one on the right side). The small horizontal shift of the peaks is due to a drift of the beamline monochromator on a timescale of several hours, which was not a limitation for the data analysis. It is important to note that the highest XMCD peak is smaller than 1% of the XAS and the others are less than 0.5%, meaning that we are working on very tiny effects if compared with XMCD spectra of ferromagnetic metals as Fe and Ni (compare with Fig.(5.3)) and our experiment was very demanding for being the very first test of the beamline. Anyhow the values we measured are of the same order of magnitude of what is found in literature [9]. The biggest XMCD is given by underdoped NBCO (red line), which is twice as big as the others, whereas the optimally doped one gives the smallest signal. In LSCO the two

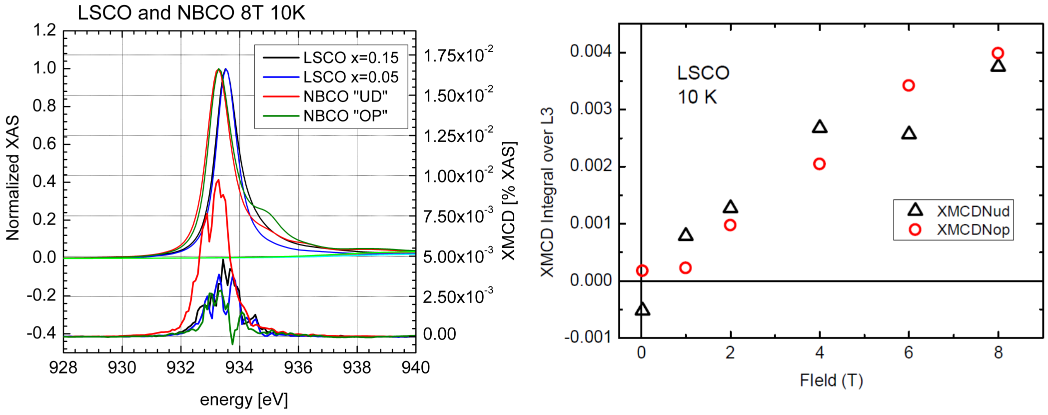

(a)

(b)

Figure 5.7: (a) Cu L_3 edge XAS and XMCD comparison for LSCO and NBCO. (b) Field dependence of LSCO Cu L_3 XMCD at 10 K.

samples give a comparable signal, with the optimally doped slightly higher at this field. For LSCO we carried out a complete field dependence of the signal at 10 K with steps of 1 T or 2 T between each experimental point and the data are plotted in Fig.(5.7b). As the XMCD signal is noisy (refer to Panel (a)) we considered more explicative to plot its integral over the L_3 edge, which is also a value used in the calculation of sum rules. The values for the optimally doped and underdoped samples are comparable all over the considered magnetic field range and both have an approximately linear evolution which is in agreement with the paramagnetic behaviour found in [17] (see Fig.(5.4b)) for other cuprates.

For the NBCO samples we inspected the temperature dependence of the XMCD signal with 8 T applied field. We measured values at the following temperatures: $T = 10\,\mathrm{K}, 50\,\mathrm{K}, 90\,\mathrm{K}$ and 300 K. In Fig.(5.8a) the thick lines represent the XMCD peaks of the NBCO samples (curves have been shifted for visualization convenience). For each curve we also reported as a thin line the measurements at 0.03 T field, where we did not expect any true signal and they thus provide the errorbar of the experiment. The XMCD integrated over the L_3 edge are plotted in Panel (b) as a function of temperature. Both the optimally doped and underdoped samples exhibit a paramagnetic behaviour at low temperature, although the absolute effect is stronger for the latter. With respect to [17] (see Fig.(5.4a)), thanks to the improved experimental conditions, we were able to observe that a non-zero XMCD signal persists even at room temperature (300 K). This signal is reliable and clearly connected to magnetism as it is well detached

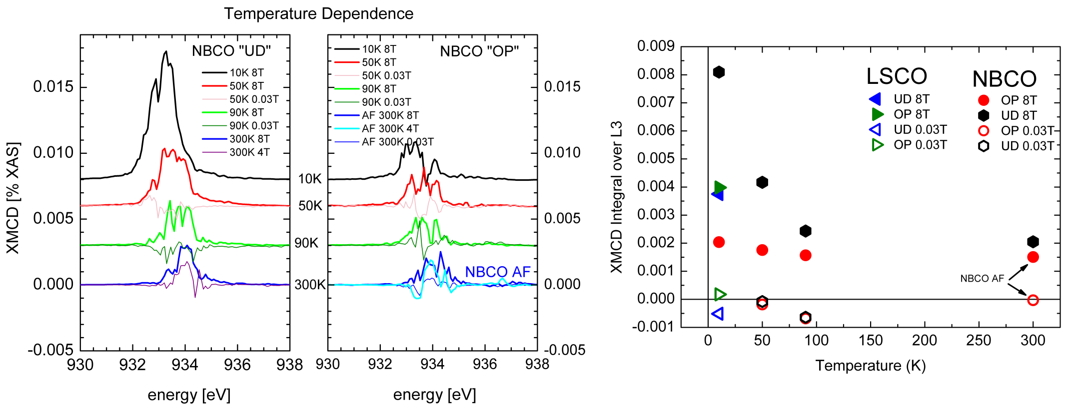

(a)

(b)

Figure 5.8: (a) Temperature dependence of Cu L_3 XMCD in NBCO measured at 8 T (thick lines). The thin lines are measurements at 0.03 T and provide the errorbar of the experiment. (b) Summary of the temperature dependence of Cu L_3 XMCD in NBCO and LSCO. The values plotted are the XMCD integrals on the Cu L_3 edge. LSCO has been measured only at low temperature (10 T).

from the zero line given by the measures at 0.03 T. At room temperature we do not have the data for the optimally doped sample but we interestingly observed an analogous dichroism in the undoped antiferromagnetic sample. Moreover the signals at 300 K and 90 K are similar for all the measured samples, although underdoped and optimally doped behave differently at lower temperatures.

After studying the Cu L_3 edge we moved on to investigate the O K edge, which is, to our knowledge, the first time it has been measured on high-T_c cuprates using XMCD. The quality of the oxygen spectra was better than the copper ones as they were showing an almost negligible energy drift that we did not have to correct. This fact allowed us to observe smaller effects than at the copper edge. We were able to see a reliable signal in the optimally doped LSCO and in the underdoped and optimally doped NBCO, but we did not measure underdoped LSCO. Fig.(5.9a) shows the XMCD (thick lines) together with the relative XAS spectra (thin lines) for the three samples we measured, in the same working conditions that gave the biggest signal on copper, *i.e.* 10 K and 8 T. The XAS of NBCO show the evolution of the pre-edge peaks with doping, which we discussed above; the first peak on the left (related to doping induced holes) is raised in the optimally doped sample, whereas the second (connected with the Cu^{2+} holes) is more evident in the underdoped. The XMCD plots are once again normalized to the XAS maximum and the figure evidences that the entity of the signal is smaller than in copper. The two NBCO samples give a comparable XMCD, whereas the

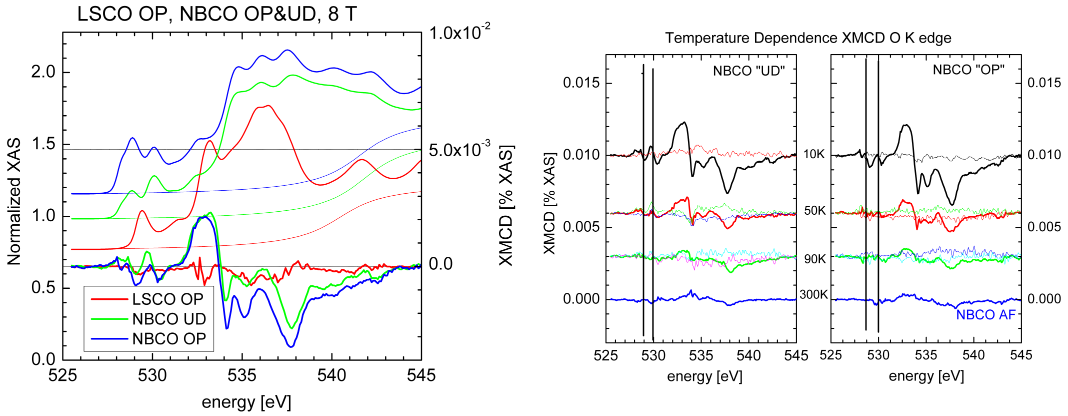

(a)

(b)

Figure 5.9: O K edge XAS and XMCD of LSCO and NBCO at 10 K. (b) Temperature dependence of the O K edge XMCD of NBCO. The vertical black lines indicate the pre-edge peaks related to holes in the CuO_2 planes.

effect in LSCO, although still visible, is around ten times smaller ($< 5 \times 10^{-4}$). The presence of the Nd magnetic ion is probably enhancing the effect in NBCO with respect to LSCO. The most relevant peaks in the XMCD are at 533 eV and 538 eV that can be associated with transitions to hybrid final states mixing O $2p$ and Nd $4p$ valence orbitals. In Panel (b) we show the temperature dependence of the XMCD spectra for underdoped and optimally doped NBCO. From top to bottom we can see how the XMCD evolves increasing the temperature. The thick lines are measured with 8 T applied field and we reported for comparison the same measures at 0.03 T (thin lines). Note that, as for the copper edge, we did not measure the optimally doped sample at room temperature, so we put in the plot the signal of the undoped one, just for comparison. The XMCD we found at O K edge is smaller and more noisy with respect to Cu L_3 edge. Moreover it shows a very complicated pattern of peaks and valleys making it difficult to quantify the signal with an integral as we did for copper. However we can establish from the plots a similar trend as the one we observed in copper. The XMCD drop as temperature increases and there seems to be a remanent signal even at room temperature that would need further inspection. The XMCD peak we are most interested in is the one corresponding to the pre-edge XAS peaks, clearly visible in graph (a). However we cannot reliably judge its evolution as its height becomes comparable to noise as the temperature is increased. Nevertheless, the dominant peaks seems to survive up to room temperature.

Conclusions

With this experiment we demonstrated that the weak magnetism driven by Dzyaloshinsky-Moriya interaction is present up to room temperature in NCBO and we suppose that it is connected to the presence of a magnetic Nd atom in the charge reservoirs layer. The phenomenon is clearly visible from the XMCD of copper, but it is not clear yet if this high temperature magnetism is partly or completely localized on the Cu1 atoms building the chains in the charge reservoir, and hence not directly involving the CuO_2 planes. The experiment was also really valuable to shed light on some non-linearities of the beamline that are important to fix in order to improve the quality of the spectra. This would be necessary if we wanted to see some effects smaller than the XMCD signal. Actually, apart from XMCD, XAS spectra acquired with opposite circular polarization and magnetic field can be combined to generate other two dichroich signals, that are X-ray Natural Circular Dichroism (XNCD) and X-ray Magneto-Chiral Dichroism (XMχD) [4, 24]. The observation of these effects could indicate the presence of a chiral order inside the material. The use of this techniques may be of utmost importance in investigating a possible chiral stacking of the charge order in underdoped cuprates, which is one of the possible hypothesis explaining the anomalous Kerr effect in YBCO recently measured by Xia *et al.* [62]. These effects however are proportional to the E1M1 and E1E2 mixed terms of the transition probability which are extremely small if compared with the dominant dipolar transitions. Due to instrumental asymmetries we were not able to observe a reliable signal, not affected by artefacts, with these techniques, hence a significant improvement would be required in order to obtain any result on this aspect. However we just remind that these effects are really small if compared with XMCD signals of magnetic material and for more ordinary experiments the spectral quality of the beamline has demonstrated to be excellent.

Bibliography

[1] Andrea Amorese. Single photon acquisition in CCD detectors for high resolution resonant inelastic soft x-ray scattering. Master's thesis, Politecnico di Milano, 2013.

[2] Andrea Amorese, Greta Dellea, Lucio Braicovich, and Giacomo Ghiringhelli. Enhancing spatial resolution of soft x-ray CCD detectors by single-photon centroid determination. arXiv:1410.1587, 2014.

[3] ID32 at the European Synchrotron Radiation Facility (ESRF). http://www.esrf.eu/usersandscience/experiments/electstructmagn/id32.

[4] Laurence D. Barron. *Molecular Light Scattering and Optical Activity.* Cambridge University Press, 2 edition, 2009.

[5] J.G. Bednorz and K.A. Müller. Possible high–T_c superconductivity in the Ba–La–Cu–O system. *Z. Phys. B: Condens. Matter*, 64(2):189–193, 1986.

[6] S. Blanco-Canosa, A. Frano, E. Schierle, J. Porras, T. Loew, M. Minola, M. Bluschke, E. Weschke, B. Keimer, and M. Le Tacon. Resonant x-ray scattering study of charge-density wave correlations in $YBa_2Cu_3O_{6+x}$. *Physical Review B*, 90:054513, 2014.

[7] Stephen Blundell. *Magnetism in Condensed Matter.* Oxford University Press, 2001.

[8] Paolo Carra, B. T. Thole, Massimo Altarelli, and Xindong Wang. X-ray circular dichroism and local magnetic fields. *Phys. Rev. Lett.*, 70:694–697, Feb 1993.

[9] J. Chakhalian, J.W. Freeland, G. Srajer, J. Strempfer, G. Khaliullin, J.C. Cezar, T. Charlton, R. Dalgliesh, C. Bernhard, G. Cristiani, H.-U. Haber-

meier, and B. Keimer. Magnetism at the interface between ferromagnetic and superconducting oxides. *Nature Physics*, 2:244–248, 2006.

[10] J. Chang, E. Blackburn, a. T. Holmes, N. B. Christensen, J. Larsen, J. Mesot, Ruixing Liang, D. a. Bonn, W. N. Hardy, A. Watenphul, M. V. Zimmermann, E. M. Forgan, and S. M. Hayden. Direct observation of competition between superconductivity and charge density wave order in $YBa_2Cu_3O_{6.67}$. *Nature Physics*, 8(12):871–876, 2012.

[11] C. T. Chen, Y. U. Idzerda, H.-J. Lin, N. V. Smith, G. Meigs, E. Chaban, G. H. Ho, E. Pellegrin, and F. Sette. Experimental confirmation of the x-ray magnetic circular dichroism sum rules for iron and cobalt. *Phys. Rev. Lett.*, 75:152–155, Jul 1995.

[12] C. T. Chen, F. Sette, Y. Ma, M. S. Hybertsen, E. B. Stechel, W. M. C. Foulkes, M. Schulter, S-W. Cheong, A. S. Cooper, L. W. Rupp, B. Batlogg, Y. L. Soo, Z. H. Ming, A. Krol, and Y. H. Kao. Electronic states in $La_{2-x}Sr_xCuO_{4+\delta}$ probed by soft-x-ray absorption. *Phys. Rev. Lett.*, 66:104–107, Jan 1991.

[13] C. T. Chen, L. H. Tjeng, J. Kwo, H. L. Kao, P. Rudolf, F. Sette, and R. M. Fleming. Out-of-plane orbital characters of intrinsic and doped holes in $La_{2-x}Sr_xCuO_4$. *Phys. Rev. Lett.*, 68:2543–2546, Apr 1992.

[14] S-W. Cheong, G. Aeppli, T. E. Mason, H. Mook, S. M. Hayden, P. C. Canfield, Z. Fisk, K. N. Clausen, and J. L. Martinez. Incommensurate magnetic fluctuations in $La_{2-x}Sr_xCuO_4$. *Phys. Rev. Lett.*, 67:1791–1794, Sep 1991.

[15] Frank de Groot. Multiplet effects in x-ray spectroscopy. *Coordination Chemistry Reviews*, 249(1):31–63, 2005.

[16] Frank de Groot and Akio Kotani. *Core Level Spectroscopy of Solids*. CRC Press, 2008.

[17] G. M. De Luca, G. Ghiringhelli, M. Moretti Sala, S. Di Matteo, M. W. Haverkort, H. Berger, V. Bisogni, J. C. Cezar, N. B. Brookes, and M. Salluzzo. Weak magnetism in insulating and superconducting cuprates. *Physical Review B - Condensed Matter and Materials Physics*, 82:2–7, 2010.

[18] G. M. De Luca, G. Ghiringhelli, C. A. Perroni, V. Cataudella, F. Chiarella, C. Cantoni, A. R. Lupini, N. B. Brookes, M. Huijben, G. Koster, G. Rijnders, and M. Salluzzo. Ubiquitous long-range antiferromagnetic coupling across the interface between superconducting and ferromagnetic oxides. *Nature Communications*, 5(5626), 2014.

[19] M. E. Dinardo, A. Piazzalunga, L. Braicovich, V. Bisogni, C. Dallera, K. Giarda, M. Marcon, A. Tagliaferri, and G. Ghiringhelli. Gaining efficiency and resolution in soft X-ray emission spectrometers thanks to directly illuminated CCD detectors. *Nuclear Instruments and Methods in Physics Research, Section A: Accelerators, Spectrometers, Detectors and Associated Equipment*, 570:176–181, 2007.

[20] A. Wylie E. Belau, R. Klanner, G. Lutz, E.neugebauer, H. J. Seerbrunner. Charge collection in silicon strip detectors. *Nuclear Instruments and Methods*, 214:253–260, 1983.

[21] G. Ghiringhelli, A. Piazzalunga, C. Dallera, G. Trezzi, L. Braicovich, T. Schmitt, V. N. Strocov, R. Betemps, L. Patthey, X. Wang, and M. Grioni. SAXES, a high resolution spectrometer for resonant x-ray emission in the 400-1600 eV energy range. *Review of Scientific Instruments*, 77:1–9, 2006.

[22] G Ghiringhelli, M Le Tacon, M Minola, C Mazzoli, N B Brookes, G M De Luca, A Frano, D G Hawthorn, F He, T Loew, M Moretti Sala, D C Peets, M Salluzzo, E Schierle, R Sutarto, G a Sawatzky, E Weschke, B Keimer, and L Braicovich. Long-Range Incommensurate Charge Fluctuations in (Y,Nd)$Ba_2Cu_3O_{6+x}$. *Science*, 337(August):821–825, 2012.

[23] R.C. Gonzalez and R.E. Woods. *Digital Image Processing, 3rd edition.* Prentice Hall, 2008.

[24] José Goulon, Andrei Rogalev, Fabrice Wilhelm, Nicolas Jaouen, Chantal Goulon-Ginet, and Christian Brouder. Optical activity probed with x-rays. *Journal of Physics: Condensed Matter*, 15(5):S633, 2003.

[25] A. Gozar, B. S. Dennis, G. Blumberg, Seiki Komiya, and Yoichi Ando. Magnetic order in lightly doped $La_{2-x}Sr_xCuO_4$. *Phys. Rev. Lett.*, 93:027001, Jul 2004.

[26] David W. Greve. *Field effect devices and applications: Devices for portable low power, and imaging systems.* Prentice Hall, 1998.

[27] David J. Griffiths. *Introduction to Quantum Mechanics.* Pearson Prentice Hall, 2nd edition, 2004.

[28] Stephen M. Hayden. Neutron scattering and the magnetic response of superconductors and related compounds. In K.H. Bennemann and J.B. Ketterson, editors, *Superconductivity*, volume 2. Springer, 2008.

[29] V. Hinkov, P. Bourges, S. Pailhes, Y. Sidis, A. Ivanov, C. D. Frost, T. G. Perring, C. T. Lin, D. P. Chen, and B. Keimer. Spin dynamics in the pseudogap state of a high-temperature superconductor. *Nature Physics*, 3:780–785, 2007.

[30] Princeton Instruments. http://www.princetoninstruments.com/.

[31] James R. Janesick. *Scientific Charge-Coupled Devices.* SPIE Press, 2001.

[32] Aharon Kapitulnik, Jing Xia, Elizabeth Schemm, and Alexander Palevski. Polar kerr effect as probe for time-reversal symmetry breaking in unconventional superconductors. *New Journal of Physics*, 11(5):055060, 2009.

[33] M. A. Kastner, R. J. Birgeneau, G. Shirane, and Y. Endoh. Magnetic, transport, and optical properties of monolayer copper oxides. *Rev. Mod. Phys.*, 70:897–928, Jul 1998.

[34] B. Keimer, N. Belk, R. J. Birgeneau, A. Cassanho, C. Y. Chen, M. Greven, M. A. Kastner, A. Aharony, Y. Endoh, R. W. Erwin, and G. Shirane. Magnetic excitations in pure, lightly doped, and weakly metallic La_2CuO_4. *Phys. Rev. B*, 46:14034–14053, Dec 1992.

[35] Y. S. Lee, R. J. Birgeneau, M. A. Kastner, Y. Endoh, S. Wakimoto, K. Yamada, R. W. Erwin, S.-H. Lee, and G. Shirane. Neutron-scattering study of spin-density wave order in the superconducting state of excess-oxygen-doped La_2CuO_{4+y}. *Phys. Rev. B*, 60:3643–3654, Aug 1999.

[36] Ruixing Liang, D. A. Bonn, and W. N. Hardy. Evaluation of CuO_2 plane hole doping in $YBa_2Cu_3O_{6+x}$ single crystals. *Phys. Rev. B*, 73:180505, May 2006.

[37] J. Lorenzana and G. Seibold. Metallic mean-field stripes, incommensurability, and chemicalpotential in cuprates. *Phys. Rev. Lett.*, 89:136401, Sep 2002.

[38] David H. Lumb and John a. Nousek. Energy and time response of CCD X-ray detectors. *IEEE Transactions on Nuclear Science*, 39(5):1379–1383, 1992.

[39] M. Matsuda, M. Fujita, K. Yamada, R. J. Birgeneau, Y. Endoh, and G. Shirane. Electronic phase separation in lightly doped $La_{2-x}Sr_xCuO_4$. *Phys. Rev. B*, 65:134515, Mar 2002.

[40] Minola Matteo. *Magnetic, Orbital and Charge Fluctuations in Layered Cuprates Studied by Resonant Soft X-Ray Scattering.* PhD thesis, Politecnico di Milano, 2013.

[41] M. Moretti Sala, V. Bisogni, C. Aruta, G. Balestrino, H. Berger, N.B. Brookes, G.M. De Luca, D. Di Castro, M. Grioni, M. Guarise, P.G. Medaglia, F. Miletto Granozio, M. Minola, P. Perna, M. Radovic, M. Salluzzo, T. Schmitt, K.J. Zhou, L. Braicovich, and G. Ghiringhelli. Energy and symmetry of *dd* excitations in undoped layered cuprates measured by Cu L_3 resonant inelastic x-ray scattering. *New Journal of Physics*, 13(4):043026, 2011.

[42] M.R. Norman, D. Pines, and C. Kallin. The pseudogap: friend or foe of high T_c? *Advances in Physics*, 54(8), 2005.

[43] H.R. Ott. High–T_c superconductivity. In K.H. Bennemann and J.B. Ketterson, editors, *Superconductivity*, volume 2. Springer, 2008.

[44] Hans P. Paar. *An Introduction to Advanced Quantum Physics.* Wiley, 2010.

[45] George G. Pavlov and John a. Nousek. Charge diffusion in CCD X-ray detectors. *Nuclear Instruments and Methods in Physics Research, Section A:*

Accelerators, Spectrometers, Detectors and Associated Equipment, 428(June 1998):348–366, 1999.

[46] Nicola Pezzotta. Algoritmi avanzati per il trattamento dei dati grezzi di uno spettrometro per scattering anelastico di raggi X. Master's thesis, Politecnico di Milano, 2008.

[47] M. Reehuis, C. Ulrich, K. Prokeš, A. Gozar, G. Blumberg, Seiki Komiya, Yoichi Ando, P. Pattison, and B. Keimer. Crystal structure and high-field magnetism of La_2CuO_4. *Phys. Rev. B*, 73:144513, Apr 2006.

[48] A. Schubert, A. Bergamaschi, C. David, R. Dinapoli, S. Elbracht-Leong, S. Gorelick, H. Graafsma, B. Henrich, I. Johnson, M. Lohmann, a. Mozzanica, V. Radicci, R. Rassool, L. Schädler, B. Schmitt, X. Shi, and B. Sobott. Micrometre resolution of a charge integrating microstrip detector with single photon sensitivity. *Journal of Synchrotron Radiation*, 19:359–365, 2012.

[49] G. Seibold and J. Lorenzana. Doping dependence of spin excitations in the stripe phase of high-T_c superconductors. *Phys. Rev. B*, 73:144515, Apr 2006.

[50] Roberta Sessoli, Marie-emmanuelle Boulon, Andrea Caneschi, Matteo Mannini, Lorenzo Poggini, Fabrice Wilhelm, and Andrei Rogalev. Strong magneto-chiral dichroism in a paramagnetic molecular helix observed by hard X-rays. *Nature Physics*, 11(January):69–74, 2015.

[51] C. Stock, W. J. L. Buyers, R. A. Cowley, P. S. Clegg, R. Coldea, C. D. Frost, R. Liang, D. Peets, D. Bonn, W. N. Hardy, and R. J. Birgeneau. From incommensurate to dispersive spin-fluctuations: The high-energy inelastic spectrum in superconducting $YBa_2Cu_3O_{6.5}$. *Phys. Rev. B*, 71:024522, Jan 2005.

[52] J. Stöhr and Y. Wu. X-ray magnetic circular dichroism: Basic concepts and theory for $3d$ transition metal atoms. In A.S. Schlachter and F.J. Wuilleumier, editors, *New Directions in Research with Third-Generation Soft X-Ray Synchrotron Radiation Sources*. Kluwer Academic Publishers, 1994.

[53] S. Straulino, O. Adriani, L. Bonechi, M. Bongi, S. Bottai, G. Castellini, D. Fedele, M. Grandi, P. Papini, S. B. Ricciarini, P. Spillantini, F. Taccetti,

E. Taddei, and E. Vannuccini. Spatial resolution of double-sided silicon microstrip detectors for the PAMELA apparatus. *Nuclear Instruments and Methods in Physics Research, Section A: Accelerators, Spectrometers, Detectors and Associated Equipment*, 556:100–114, 2006.

[54] M. Le Tacon, G. Ghiringhelli, J. Chaloupka, M. Moretti Sala, V. Hinkov, M. W. Haverkort, M. Minola, M. Bakr, K. J. Zhou, S. Blanco-Canosa, C. Monney, Y. T. Song, G. L. Sun, C. T. Lin, G. M. De Luca, M. Salluzzo, G. Khaliullin, T. Schmitt, L. Braicovich, and B. Keimer. Intense paramagnon excitations in a large family of high-temperature superconductors. *Nature Physics*, 7(9):11, 2011.

[55] Tineke Thio, T. R. Thurston, N. W. Preyer, P. J. Picone, M. A. Kastner, H. P. Jenssen, D. R. Gabbe, C. Y. Chen, R. J. Birgeneau, and Amnon Aharony. Antisymmetric exchange and its influence on the magnetic structure and conductivity of La_2CuO_4. *Phys. Rev. B*, 38:905–908, Jul 1988.

[56] B. T. Thole, P. Carra, F. Sette, and G. van der Laan. X-ray circular dichroism as a probe of orbital magnetization. *Phys. Rev. Lett.*, 68:1943–1946, Mar 1992.

[57] T. R. Thurston, R. J. Birgeneau, M. A. Kastner, N. W. Preyer, G. Shirane, Y. Fujii, K. Yamada, Y. Endoh, K. Kakurai, M. Matsuda, Y. Hidaka, and T. Murakami. Neutron scattering study of the magnetic excitations in metallic and superconducting $La_{2-x}Sr_xCuO_{4-y}$. *Phys. Rev. B*, 40:4585–4595, Sep 1989.

[58] J. M. Tranquada, A. H. Moudden, A. I. Goldman, P. Zolliker, D. E. Cox, G. Shirane, S. K. Sinha, D. Vaknin, D. C. Johnston, M. S. Alvarez, A. J. Jacobson, J. T. Lewandowski, and J. M. Newsam. Antiferromagnetism in $YBa_2Cu_3O_{6+x}$. *Phys. Rev. B*, 38:2477–2485, Aug 1988.

[59] J. M. Tranquada, B. J. Sternlieb, J. D. Axe, Y. Nakamura, and S. Uchida. Evidence for stripe correlations of spins and holes in copper oxide superconductors. *Nature*, 375:561–563, 1995.

[60] John M. Tranquada. Neutron scattering studies of antiferromagnetic correlations in cuprates. In J. Robert Schrieffer and James S. Brooks, editors, *Handbook of High-Temperature Superconductivity*. Springer, 2007.

[61] R. Turchetta. Spatial resolution of silicon microstrip detectors. *Nuclear Instruments and Methods in Physics Research Section A: Accelerators, Spectrometers, Detectors and Associated Equipment*, 335:44–58, 1993.

[62] Jing Xia, Elizabeth Schemm, G. Deutscher, S. A. Kivelson, D. A. Bonn, W. N. Hardy, R. Liang, W. Siemons, G. Koster, M. M. Fejer, and A. Kapitulnik. Polar kerr-effect measurements of the high-temperature $\mathrm{YBa_2Cu_3O_{6+x}}$ superconductor: Evidence for broken symmetry near the pseudogap temperature. *Phys. Rev. Lett.*, 100:127002, Mar 2008.

[63] K. Yamada, C. H. Lee, K. Kurahashi, J. Wada, S. Wakimoto, S. Ueki, H. Kimura, Y. Endoh, S. Hosoya, G. Shirane, R. J. Birgeneau, M. Greven, M. A. Kastner, and Y. J. Kim. Doping dependence of the spatially modulated dynamical spin correlations and the superconducting-transition temperature in $\mathrm{La_{2-x}Sr_xCuO_4}$. *Phys. Rev. B*, 57:6165–6172, Mar 1998.

[64] Shaodi Zhang, Honghai Sun, Yanjie Wang, Xiaomeng Jia, and Hao Chen. Design of high precision star image locating method used in star sensor technology. In *2010 International Conference on Computer, Mechatronics, Control and Electronic Engineering, CMCE 2010*, volume 5, 2010.

[65] J.F. Ziegler. Terrestrial cosmic rays. *IBM Journal of Research and Development*, 40(1):19–39, 1996.